An Observation of Low Energy Cosmic Antiprotons

（低エネルギー宇宙線反陽子の観測）

上田 郁夫

An Observation of Low Energy Cosmic Antiprotons

By
Ikuo Ueda

Department of Physics,
School of Science,
University of Tokyo

1995

Abstract

A search for antiprotons ($\bar{p}$'s) in the cosmic radiation was performed using the BESS balloon-borne magnetic spectrometer, resulting in the first definitive detection of cosmic antiprotons, as well as the first measurement of its flux at the low energies. The flights were made in 1993 and 1994 at a residual atmosphere below $5 g/cm^2$ and the geomagnetic cut-off rigidity below 0.5 GV. The particles were identified by the mass measurement based on the precise measurements of rigidity, time of flight and energy loss. Eight clearly identified antiprotons were detected, two in the kinetic energy range 175–350MeV, four in 350–500MeV, and two in 500–600MeV, giving the antiproton fluxes of $(5.1\,^{+8.9\,+2.9}_{-3.7\,-2.4}) \times 10^{-3}$, $(9.2\,^{+9.7\,+4.8}_{-5.6\,-3.6}) \times 10^{-3}$, and $(1.0\,^{+2.0\,+0.5}_{-0.8\,-0.4}) \times 10^{-2}$ $m^{-2}sr^{-1}sec^{-1}GeV^{-1}$ in the respective energy ranges after correcting for the instrumental and selectional efficiencies. The $\bar{p}/p$ ratio was measured to be $(3.6\,^{+6.1\,+2.0}_{-2.6\,-1.7}) \times 10^{-6}$, $(7.0\,^{+7.3\,+3.6}_{-4.3\,-2.7}) \times 10^{-6}$, and $(1.0\,^{+1.9\,+0.5}_{-0.7\,-0.4}) \times 10^{-5}$. The observed flux and the $\bar{p}/p$ ratio are consistent with the predictions on the secondary antiprotons of the leaky box model as well as of the diffusive reacceleration model, and place a new unique constraint on the explosion rate of evaporating primordial black holes of $R < 1.3 \times 10^{-2} pc^{-3} yr^{-1}$(90% C.L.).

Contents

List of Tables

List of Figures

Chapter 1

Introduction

The energy spectrum of cosmic antiprotons provides important and interesting information on the cosmic ray propagation models, as well as on the hypothetical novel processes such as the evaporation of primordial black holes or the annihilation of supersymmetric dark matters (neutralinos).

Cosmic antiprotons are expected to be produced secondarily by the collisions of cosmic rays with the interstellar medium. Since protons dominate in the cosmic rays, and the interstellar medium consists mainly of hydrogen gas, one can expect a flux of cosmic antiprotons through the reactions

$$
\begin{aligned}
& p_{cr} + p_{gas} \longrightarrow \bar{p} + x \\
& \text{or} \\
& p_{cr} + p_{gas} \longrightarrow \bar{n} + x \\
& \qquad\qquad\quad \searrow \bar{p} + e^{+} + \nu_{e} \ ,
\end{aligned}
$$

where x stands for other particles which emerge with the antiproton from the interaction.

The energy spectrum of the antiprotons to be observed depends on that of protons, on the characteristics of the interactions in pp-collisions, and on the subsequent energy changing processes in propagation. The kinematic conditions on the interactions require the lowest threshold energy on the cosmic ray protons of $E^{th}_{p_{cr}}$~6GeV. The particles produced at this threshold are $pppp\bar{p}$ at rest in the center of mass (CM) system, having a kinetic energy of about 1GeV in the laboratory system. The energy of the antiproton could be lower than 1GeV when the cosmic ray proton has a higher energy and the antiproton is produced in the backward direction in CM system to the incoming cosmic ray proton. However this probability is reduced by the small phase space factor. Hence the spectrum of the antiprotons will decline steeply at energies below 1GeV. On the contrary, no such the suppression of low energy antiprotons is expected for primary sources such as the evaporation of the primordial black holes, or the annihilation of the supersymmetric (neutralino) dark matters.The low energy antiprotons could thus be a potent probe for the novel pri-

mary processes. Figure 1.1 shows the predicted antiproton fluxes for the cosmic ray secondaries, for the evaporation of primordial black holes and for the annihilation of neutralino dark matters.

The "standard leaky box (SLB) model" is the most popular model of the cosmic ray propagation, in which the cosmic rays escape from the galactic disk after having traversed about 10 g/cm^2 of interstellar medium. Antiprotons will be produced in the collisions of the cosmic ray protons and heliums with the interstellar medium, and will propagate in the Galaxy. The flux of this secondary antiprotons can be calculated using the escape length determined by fitting the observed ratios of secondary to primary nuclei, such as B/C [1, 2, 3, 4].

The "diffusive reacceleration (DR) model" [5] proposed recently, takes into account a link between diffusion and reacceleration. It interprets the propagation of cosmic rays as a diffusive process, and requires no further effective mechanisms for the escape of particles below ~1GeV/nucleon from the Galaxy which is needed in the standard leaky box model in order to explain the observations on cosmic ray nuclei.

The spectra of the antiprotons predicted by these two models have their peaks around 2GeV of kinetic energy, showing a steep decline at lower energies due to the kinematical suppression, as well as at higher energies due to the decline of the cosmic ray fluxes.

In a recent systematic study [6], the absolute energy spectra of the secondary antiprotons has been calculated for these models with a reasonably small uncertainty. It is also realized that these energy spectra of the antiprotons will not be affected by the solar modulations because of its specific spectral shape. Hence the measurement of the antiproton flux at the top of the atmosphere will provide informations to examine the model.

A possible novel source of primary antiprotons is the evaporation of mini black holes. The "primordial black holes" (PBHs), which might have formed in the early universe [7, 8, 9], are the only black holes small enough for the quantum emissions to be significant. The rate of the quantum emission from a black hole with a mass of M is just the same as the rate of a thermal radiation from a body with temperature of $T \propto M^{-1}$ [10, 11]. PBHs would thus radiate rapidly, loose their mass, and will reach higher and higher temperatures. Finally the temperature would get extremely high and PBHs would explodingly radiate various particles, including antiprotons [12, 13, 14]. The flux of these antiprotons would rise toward the lower energy, and could clearly be distinguished from the secondary antiproton flux. In a recent detailed study [15], the energy spectrum of these antiprotons is calculated with a reasonably small uncertainty, and it has become possible to discuss the abundance of PBHs using the experimental data.

The annihilation of the supersymmetric (neutralino) dark matters could also be a source of the primary antiprotons. Neutralino is supposed to be the lightest supersymmetric particle, and therefore to be stable. Such a weakly interacting massive

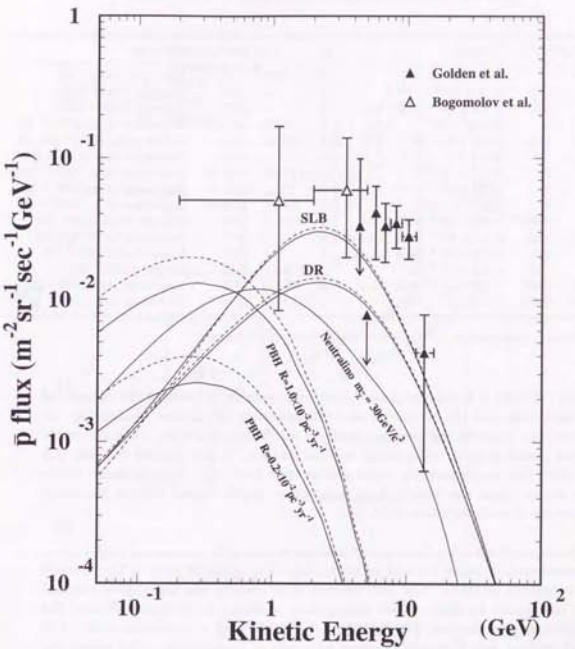

Figure 1.1: Predicted antiproton fluxes and experimental data. The solid and dashed curves labeled "SLB" and "DR" are the calculations by Mitsui [6] based on standard leaky box model [4] and on diffusive reacceleration model [5], respectively. The spectrum for neutralino annihilation (the curve labeled "Neutralino") are from Jungman and Kamionkowski [17], being converted into a flux by multiplying the proton flux. The spectra for primordial black holes (the curves labeled "PBH") are the calculations by Maki *et al.*[15]. All the curves are corrected for solar modulations (dashed curves for ϕ=500MV, i.e. minimum modulation, and solid curves for ϕ=600MV). The experimental data points are from Golden *et al.*[23, 24] (filled triangles) and Bogolomov *et al.*[26, 27, 24] (open triangles).

Table 1.1: Summary of experimental results on $\bar{p}/p$ ratio .

Energy (GeV)	$\bar{p}/p$ ratio	$N_{\bar{p}}$	N_p	Year	Reference
———	$\lesssim 1 \times 10^{-3}$	0	1000	1957	Aizu *et al.*(1961)† [18]
0.10 – 0.15	$\lesssim 3 \times 10^{-4}$	0	—	1962	Apparao (1967)† [19]
0.05 – 0.15	$< 4.3 \times 10^{-4}$ (1σ)	0	—	1972	Apparao (1985)† [20]
2 – 5	$(6 \pm 4) \times 10^{-4}$	2	3400	1972–77	Bogomolov *et al.*(1979)†† [21]
4.7 – 11.6	$(5.2 \pm 1.5) \times 10^{-4}$	34.9	54600	1979	Golden *et al.*(1979)†† [22, 23]
0.13 – 0.37	$(2.2 \pm 0.6) \times 10^{-4}$	14	—	1980	Buffington *et al.*(1981)† [25]
0.2 – 2	$(6^{+14}_{-5}) \times 10^{-5}$	1	17800	1984–85	Bogomolov *et al.*(1987)†† [26]
2 – 5	$(3^{+4}_{-2}) \times 10^{-4}$	2+0	$\frac{3400}{+2200}$	1972–86	Bogomolov *et al.*(1987)†† [26]
2 – 5	$(2.4^{+2.8}_{-1.3}) \times 10^{-4}$	3	12400	1986–88	Bogomolov *et al.*(1090)†† [27]
0.1 – 0.64	$< 2.8 \times 10^{-5}$ (85% C.L.)	0	87213	1987	Salamon *et al.*(1990)‡ [28]
0.64 – 1.58	$< 6.1 \times 10^{-5}$ (85% C.L.)	0	38590	1987	Salamon *et al.*(1990)‡ [28]
0.6 – 0.8	$< 2.3 \times 10^{-4}$ (90% C.L.)	3	41514	1987	Moats *et al.*(1990)†† [29]
0.12 – 0.60	$< 4.2 \times 10^{-6}$ (2σ)	1	322281	1987	Stochaj (1990)‡ [30]
0.175 – 0.300	$< 2.9 \times 10^{-5}$ (90% C.L.)	0	405860	1993	Yoshimura *et al.*(1995)‡ [31]
0.300 – 0.500	$(1.2^{+1.9}_{-0.65}) \times 10^{-5}$	4	772940	1993	Yoshimura *et al.*(1995)‡ [31]

†annihilation identification ††Čerenkov veto ‡mass measurement

particle (WIMP) is a popular dark matter candidate in the view of the primordial nucleosynthesis and the formation and the clustering of galaxies. Supposing the galactic halo contains the neutralinos, their annihilation in their collisions would produce cosmic primary antiprotons in some fraction. It was pointed out that this antiproton flux might possibly reach a detectable level [16]. A more recent calculation showed that the flux of these antiprotons might exceed that of secondary antiprotons at energies below 1GeV [17].

There have been many balloon experiments searching for cosmic ray antiprotons, as summarized in Table 1.1 and in Figure 1.2. The methods used in the searches are categorized in three. The first method is to identify the antiprotons stopped in the instrument by their specific annihilation radiation in the materials. For this annihilation identification, the backgrounds could reach a significant level. The second method uses Čerenkov counters as a veto of backgrounds, after separating negative particles from positive ones by measuring their deflection in the magnetic field. This way of identification is vulnerable to various backgrounds as well as to the errors in determining the efficiencies of the Čerenkov counters. The most positive identification can be made by determining the mass of the particles, based on the measurement of their magnetic rigidity, velocity, and $\mathrm{d}E/\mathrm{d}x$.

The earliest experiments was performed based on the annihilation identification using emulsion stacks [18, 19, 20], however, the solid angle of the stacks were small and failed to observe a signal. The first reports of the observations of cosmic ray antiprotons [21, 22] and the succeedings [26, 27, 29] were based on the searches at higher energies, where higher antiproton fluxes are expected. These experiments,

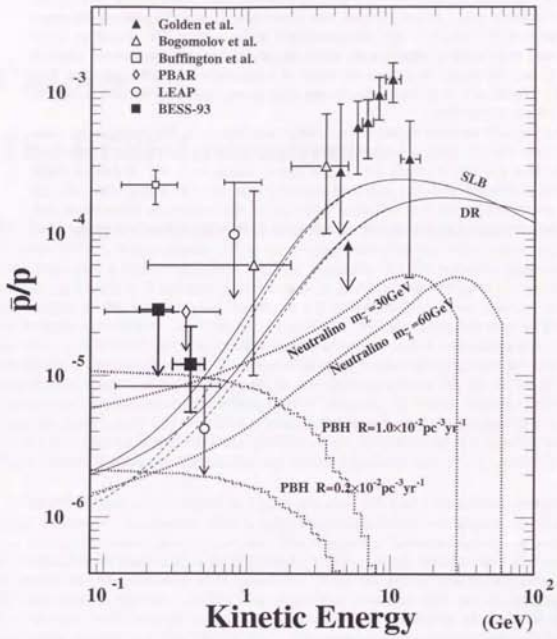

Figure 1.2: Current summary of $\bar{p}/p$ ratio from experiments and calculations. The data points are Bogolomov *et al.*[26, 27] (open triangles), Golden *et al.*[23] (filled triangles), Buffington *et al.*[25] (open squeare), PBAR experiment [28] (open diamonds), LEAP experiment [29, 30] (open circles), and BESS-93 [31] (filled squares). The solid and dashed curves are the calculations by Mitsui [6] based on the standard leaky box model (SLB) [4] and on the diffusive reacceleration model (DR) [5]. The dashed curves are for minimum solar modulation (the mean energy loss ΔE =500MeV) and the solid are for ΔE =600MeV. The spectra from neutralino annihilation are from fig.1 in Reference [17]. The spectra from the evaporation of primordial black holes ("PBH") are the calculations by Maki *et al.*[15] for ΔE =500MeV. The spectra for ΔE =600MeV is almost the same.

however, lacked the very definitive identification since the mass of the particles cannot be determined in those energy region. Therefore these observations had to rely on the Čerenkov veto. At low energies, one experiment reported a positive detection of antiprotons utilizing the annihilation-identification method [25]. However, more recent and more reliable experiments which employ the mass-measurement method failed to see the signal at a level an order of magnitude below the reported flux [28, 30]. Therefore it is probably fair to say that there existed no definite detection of the cosmic antiprotons.

Very recently we have detected four antiproton events at low energies by measuring their masses, using a magnetic spectrometer with a much larger acceptance, and provided the first evidence for the low energy antiprotons [31]. A further flight has been performed with the improved instrument in the succeeding year. In this thesis, we report on the first definitive detection of the cosmic ray antiprotons and the mearsurement of its flux at low energies, based on eight antiproton events.

Chapter 2

The BESS Instrument

The Balloon-borne Experiment with a Superconducting solenoidal magnet Spectrometer (BESS) was proposed [32] as an omnipurpose detector, with a very large solid angle and a highly redundant tracking capability, for the scientific purposes such as the detection of low energy antiprotons in search of novel primary processes, and a highly sensitive search of antinuclei, as well as the precise determination of absolute cosmic ray fluxes. The detector is constructed by embodying the state of the art technology from the modern collider experiments such as the thin superconducting solenoid, the precision drift chambers with multi-track capability, the precision time of flight system, and the high speed data acquisition system [33, 34, 35, 36, 37]. The present BESS collaboration is composed of University of Tokyo, National Laboratory for High Energy Physics (KEK), Institute for Space and Astronautical Science (ISAS), New Mexico State University (NMSU), Kobe University and Goddard Space Flight Center of National Aeronautics and Space Administration (NASA/GSFC).

The BESS instrument, shown in Figure 2.1 and 2.2, has a cylindrical configuration of detector components with a superconducting solenoidal magnet which is thin enough for cosmic rays to traverse. This unique configuration provides a large geometrical acceptance with a large tracking volume, which enables carefull measurements and searches with high sensitivity. Since the geometrical acceptance of the instrument is abount $0.5 m^2 sr.$, tens of millions of cosmic rays can be detected in a one-day flight, corresponding, for instance, to the sensitivity of the ratio of antiproton to proton at the level of 10^{-6}. The large tracking volume occupied by the detectors with high position-resolution provides a precise momentum measurement. Furthermore, it is possible, by the deteailed tracking, to recognize the tracks which interact or scatter in the midst of the instrument. This is crucial in searching for very rare antiprotons or antinuclei among millions of proton- and helium-cosmic rays, since such the interactions or the scatters might result in a wrong rigidity measurement or even a mis-identification of positively charged particles as negative ones.

It was essential to design a high-speed data acquisition system which can handle the high trigger rate due to the large geometrical acceptance as well as large data size produced by the large-volume tracking detectors. In addition, it was crucial for

Table 2.1: Main specifications of the BESS instrument.

Geometrical acceptance	0.4 m^2 sr
Maximum detectable rigidity	200 GV
Time of Flight resolution	300 ps
First level trigger rate	2 kHz
Second level trigger rate	100 – 200 Hz
Event recording rate capacity	400 Hz
Event storage capacity	10 Gbytes ($\simeq 8 \times 10^6$events)
Material in the instrument	14 g/cm^2
Material of the gondola shell	0.54 g/cm^2
Gondola shell dimension	1.5 m$\phi \times$ 3.2m
Total weight	2,060 kg
Power consumption	1.2 kW

the balloon-borne detector to restrain the total weight as well as the total power consumption to a low level. Table 2.1 summarizes the main specifications of the BESS instrument.

In order to identify a particle, the mass and the charge of the particle are determined by measuring its magnetic rigidity (momentum per charge), velocity and ionization energy losses. The rigidity of incident particles are determined by the magnetic rigidity spectrometer composed of the superconducting solenoidal magnet and three drift chambers of two types (JET and IDCs) which reside in the bore of the solenoid . Using the drift chambers the curvature of the track of an incident charged particle, which is deflected in the strong and uniform magnetic field produced by the solenoidal magnet, is measured and the rigidity and the sign of its charge are obtained. A time-of-flight (TOF) system is used to determine the velocity of the particle. Two sets of scintillation counters placed at the top and the bottom of the instrument are used to measure the time of flight of the particle. Then the velocity of the particle is obtained, combining the time with the path length determined by the track information. The scintillation counters are also used to measure the energy the incident particle loses in a scintillator, by which the magnitude of the charge is determined and an auxiliary means of particle identification is provided using the velocity dependence of the energy loss. Čerenkov counters are installed in the flight of 1994 to make the instrument more capable of particle identification.

All detector components were arranged concentrically, and were contained in the aluminum pressure vessel of 3.2m long, 1.5m across, and 2mm thick, which kept the internal conditions, such as the pressure and the temperature, at a desired level during the flight in the rarefied and cold atmosphere at the high altitude. The data acquisition system including the front-end read-out electronics and microcomputers was also contained in the vessel except for the magnetic tape data recorders which do not work in the strong magnetic field produced by the superconducting magnet. The data recorders were contained in the pressure vessels made of iron being shielded

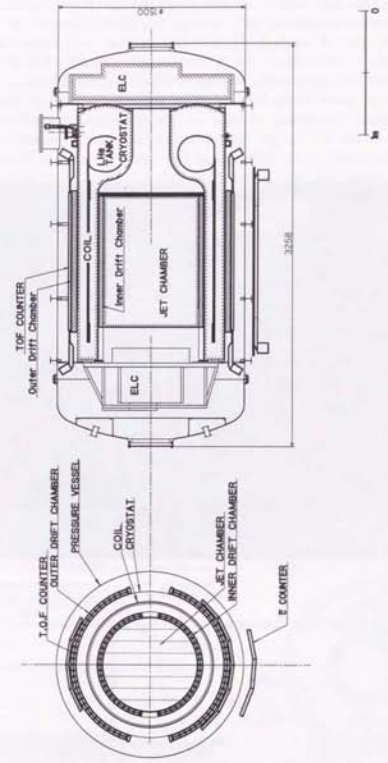

Figure 2.1: Cross-sectional view of the BESS instrument

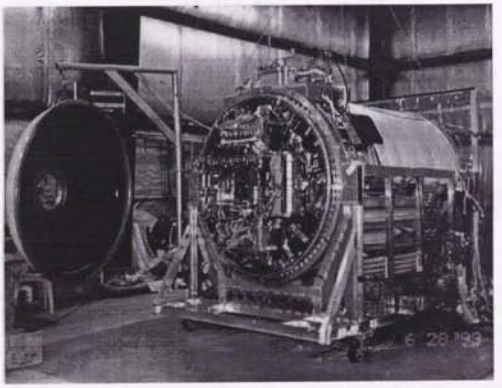

Figure 2.2: Photograph of the BESS instrument

from the magnetic field. The power supply system for the instrument which consists of batteries, electric relays and remote control system of them was installed on the exterior so as to be accessible until the launch. The package of communication devices which was supplied by the National Scientific Balloon Facility (NSBF) for remote commanding and telemetry, was situated in an iron box outside the pressure vessel. The entire apparatus weighed 2,060 kilograms. Lifted by a 29.47-Mft^3 ($8.34 \times 10^5 m^3$) helium-filled balloon, it ascended up to an altitude of about 35 km where the atmospheric pressure is about 5g/cm^2. In order for cosmic ray particles to be detected by the instrument, they had to go through 5g/cm^2 of the air and 14.5 g/cm^2 of the material in the instrument and the gondola shell. The total material was thin enough for particles below 1GeV to pass through and the lowest energy of the protons detected by the instrument was to be 175MeV. The individual detector components and data acquisition system will be discussed in detail in the following sections.

2.1 Thin Superconducting Solenoidal Magnet

Figure 2.3 shows cross-sectional views of the thin superconducting solenoidal magnet. The advantages of this magnet are (i) uniform magnetic field and (ii) large acceptance and tracking volume in it, while the materials surrounding the tracking volume are thin enough for cosmic ray particles to pass through. The conceptual design will be found in Yamamoto *et al.*[38].

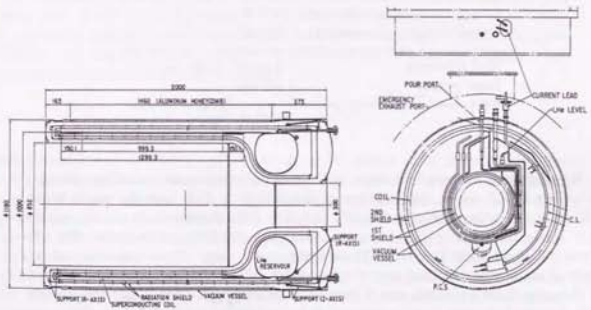

Figure 2.3: Cross-sectional view of the superconducting solenoidal magnet.

Table 2.2: Main specifications of the superconducting solenoidal magnet.

Coil		
material	conductor	NbTi/Cu
	stabilizer	Pure Al (99.999%)
diameter		1.0 m
length		1.3 m
thickness	(center)	5.2 mm
	(end)	10.4 mm
Support cylinder		
material		A2219
thickness	(center)	2 mm
	(end)	4 mm
Cryostat		
diameter		1.18 m
length		2.0 m
LHe capacity		150 ℓ
		(6 days in excitation)
Warm bore		
caliber		0.85 m
length		1.0 m
Central field	(maximum)	1.2 T
	(operational)	1.0 T
Current	(maximum)	520 A
	(operational)	430 A
Stored energy	(maximum)	815 kJ
Wall thickness		4 g/cm^2 (0.21 X_0)
Total weight		430 kg

It generates a uniform field about 1.2T with a nominal current at 520A, storing an energy 815kJ, while the variation of the field is $\pm$ 15% over the warm bore 0.85mϕ $\times$ 1.0m that contains the JET and IDC drift chambers. It was operated at a nominal current of 430 A during the flights, producing a magnetic field of about 1T (from 0.865T to 1.139T) over the warm bore. The solenoidal coil is made of aluminum-stabilized superconductor NbTi(Cu) and has dimensions of 1m in diameter, 1.3m in length and 5.2mm in thickness, with 15cm long extra turns with 5.2mm thickness (10.4mm in total) at both ends for a better field uniformity. The support cylinder which surrounds the coil and withstand the hoop force is made of high strength aluminum alloy (2219-t851) and liquid helium reservoir tank with a toroidal shape is welded to its end. The coil, the support cylinder and the reservoir

tank are enclosed with two layers of thermal radiation shields and contained in a vacuum vessel. The reservoir tank has a capacity of 150ℓ and is to keep cooling the coil via the support cylinder for 6 days, This static indirect cooling method using only thermal conduction is adopted because of no need for active elements during balloon flights, and of the thinness of the wall of the cryostat surrounding the tracking volume compared to the bath cooling method. The thickness of the solenoidal magnet including the cryostat is 0.21 radiation length and its total weight is 430kg including liquid helium. The magnet is excited in persistent current mode during experiments, where the magnetic field decays with a time constant of 900 years, and in order to charge or discharge the magnet, the persistent current switch (PCS) is to be turned off by heating a part of the loop of the superconductor. To extract the energy stored in the magnet at the time of discharging, a resistor parallel with PCS is equipped at the exterior of the pressure vessel and the current which runs PCS is shunted to the resistor by turning PCS off. The ratio of the stored energy (E) to the effective coil mass (M) including the support cylinder is high enough for hot spots to break out easily resulting in quenches and damages in quenching. A new effective quench protection system is adopted using pure aluminum strips, which increase the net axial thermal conductivity and prevent quenches, while, in case of a quench, leading it into a homogenized energy dump in the entire coil. Further details of the performance of the magnet will be found in Makida *et al.*[39]. Table 2.2 summarizes the main specifications of the magnet.

2.2 JET chamber

JET chamber, shown in Figure 2.4, is a cylindrical drift chamber situated in the warm bore of the solenoidal magnet. It has a large tracking volume of 0.754mϕ $\times$ 1m, and a position resolution of 200μm in the drift direction. Combining these features, one can obtaine a resolution in measurement of transverse rigidity, the component perpendicular to the magnetic field:

$$\frac{\delta(R_t)}{R_t} \simeq 0.005 \cdot (R/GV),$$

and the maximum detectable rigidity (MDR) about 200GV. JET chamber also provides the z-coordinates, the position along the wire direction, of the track, which is derived by charge division method [40]. The charge induced on a sense wire will be divided into two fractions each of them being fed to the preamplifiers at the ends of the wire. The ratio of the charge fractions fed to two preamplifiers is z-dependent due to the resistance of the wire. Though the resolution is not good enough to achieve a desired rigidity resolution by itself alone, it is acculate enough to make use of z information of IDCs, and combined with them, a sufficient resolution are obtained. The actual performance will be shown in Chapter 4. Here is described the structure and the line of track measurment.

The cylindrical side wall of JET chamber is made of KAPTON sheets 125μm thick, stiffened by aramid honeycomb core glued in between two sheets, providing a

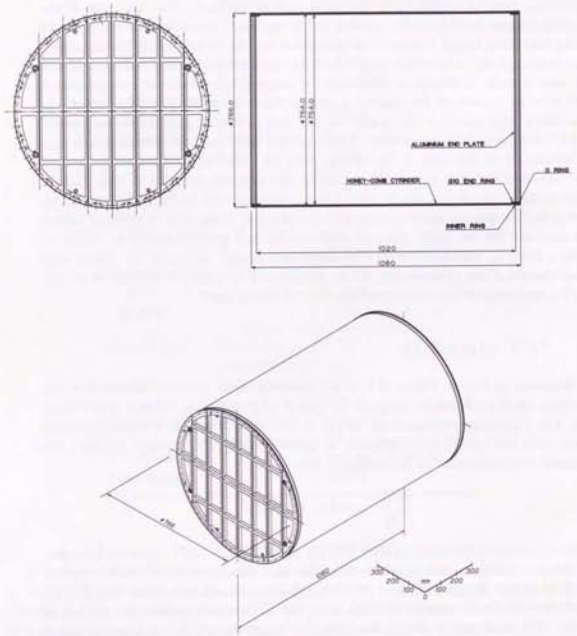

Figure 2.4: Schematic view of the JET chamber.

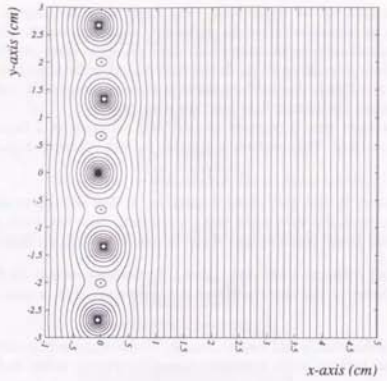

Figure 2.5: Equipotential contour map of the electric field of JET chamber.

required strength with a small amount of material. The surfaces of the both side of the wall are pasted with copper sheets 35μm thick, the outer of which plays a role as an electric shield and on the inner is etched a pattern to be used as cathodes. The end-plates are made of 20-mm-thick aluminum disks, with 15-mm-deep hollows on it, providing a one-body structure of a 20-mm-thick frame and a 5-mm-thick plate. The total weight of the chamber is 60kg.

The chamber is partitioned vertically into four sections of width 19 cm by three cathode planes each of which consists of about a hundred of aluminum wires, placed at intervals of 6.7mm. The inner surface of the cylinder wall also makes cathodes, with the field-shaping copper pattern etched on it. The central two sections contains 52 sense wires each, and the outer two sections 32 sense wires each. At the center of each section laid out are sense wires at intervals of 13.4mm, between which potential wires are placed in order to lead drift electrons smoothly to the sense wires. The sense wires are made of gold-plated tungsten-rhenium alloy, 20μm in diameter, and are strung with a tension of 40gw. The cathode and the potential wires are made of gold-plated aluminum, 200μm in diameter, and are strung with a tension of 300gw.

A flat electric field, 95mm long, is made by the cathode wires (or the cathode patterns on the cylinder wall) and the sense wires, -10.8kV of high voltage being applied to the cathode wires and 0V to the sense wires. The electrons produced in the ionization of the gas molecular by the incident cosmic ray particles drift along the field to the sense wires. Near the sense wires, the potential wires enhances

the focusing of the field to the sense wires. The sense wires are aligned with a small staggering so as to resolve 'left-right ambiguity' that from which side of the sense plane the ionization electrons came; i.e. alternate sense wires are displaced by ±0.5mm from their original positions in the field direction and thus only one of possible two space coordinates derived from the drift time can compose a continuous track. Figure 2.5 shows the electric field near the sense wires.

The chamber is filled with a mixture of CO_2 and Ar gases at a mixing rate 90% and 10%, respectively. This mixture is suitable for this experiment due to the following reasons:

1. The drift velocity in this gas, about 6.6mm/μs, is slow enough to achieve a good position resolution even while using a relatively slow electronic package designed for low power consumption, which is crucial for balloon experiments.

2. Due to a small diffusion coefficient, timing fluctuations caused by the longitudinal diffusion of the electron cloud are small even after a long drift of 95mm.

3. The gas is non-flammable and easy to handle. Unlike experiments carried-out in laboratories, balloon-borne experiments require extreme safety and convenience.

This mixture was used for the other drift chambers for the same reasons, and the entire vessel was filled with it so that any chamber suffering a small gas leak would remain operational during the flight.

The signals from the sense wires are picked up by preamplifiers mounted on the end-plates, in the hollow of it, then amplified and converted into voltage signals that are fed into 28.5-MHz flash-type analog-to-digital converter (FADC) modules [43]. The FADC modules further amplify the signals and digitize them into 8-bit digits every 35ns. Since the shape of each input pulse can be reconstructed using the output of the FADC module, the time-sliced pulse height, multiple hits on a single wire can be well separated and recognized. Since the total amount of FADC data is too large to record all the data during the flight, on-line zero-suppressing circuits were adopted to discard the data not containing signal pulse information, and a data compression circuit was employed to reduce the data amount by a factor of about 3 while retaining the principal information on the signal pulse. Briefly, in a zero-suppressing circuit included in every FADC module, digitized data are discriminated by a digital comparator and only data above thresholds are accumulated into a first-in-first-out (FIFO) memory. The data compressor read these data from the FIFOs of all FADC modules sequentially, and when it detects a pulse, a cluster of data with successive time indices, it compresses the data into 8-byte data consisting of the total charge (the integration of the pulse heights), the first time index, the first two pulse heights, and the pulse width. The entire process takes about 100–150μs, depending on the number of time-sliced pulse-height data stored in the FIFOs.

The position of the hits are three-dimensionally determined by the time index and the charge of signals. Taking the axis of the chamber, which is also the co-axis

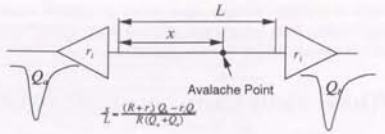

Figure 2.6: Circuit model of the charge division method used for determining the z-coordinate.

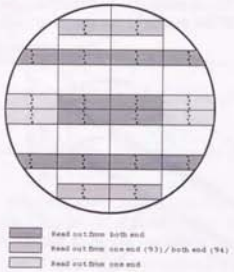

Figure 2.7: The wires of JET chamber which were read-out in the experiment.

of detectors, as z-axis and the vertical as y-axis, the magnetic field is parallel to z-axis and the electric field to x-axis. Since the deflection of incident particles is perpendicular to the magnetic field, it is convenient to describe the trajectories in x-y plane and z-s plane, where s-coordinate is taken along the x-y component of the trajectory. The position of the hits in x-y plane is determined by their time index. The z-coordinate of the hits are obtained from the ratio of the charges read out at the two ends of the hit wires as shown in Figure 2.6. The resistances and the gain of the preamplifiers are calibrated using the flight data.

The signals from 80 sense wires were read in the experiment, to reduce the number of the FADC modules and the power consumption, of which 48 wires in 1993 flight and 64 in 1994 flight were read from both ends to determine the z-coordinate (Figure 2.7). The central two sections of JET chamber contain 24 active (or read-out) sense wires each, of which 16 (24) wires were z-determining wires.

The external two sections contain 16 active sense wires, of which 8 wires were z-determining. The performance tests using accelerator beam and cosmic rays, carried out at KEK, showed resolutions 200μm in x and 1-2cm in z.

2.3 Inner/Outer Drift Chambers (IDC/ODC)

The inner drift chambers (IDCs) and the outer drift chambers (ODCs) are arc-shaped cell-type drift chambers (Figure 2.8), which were located at the inside and the outside of the magnet, respectively. They were used as trigger chambers, i.e. the number of hits in each chamber and the combination of their hit-wire indices were used for the second level trigger to select negative-charged single track events (see Section 2.6.2). They of course provided hit-point information. The hit-points in IDCs were combined with the hit-points in JET chamber and used in trajectory fitting. Let the coordinates of the hit points be described in a cylindrical coordinate system, where z-axis is taken to be co-axis of the detector configuration. The res-

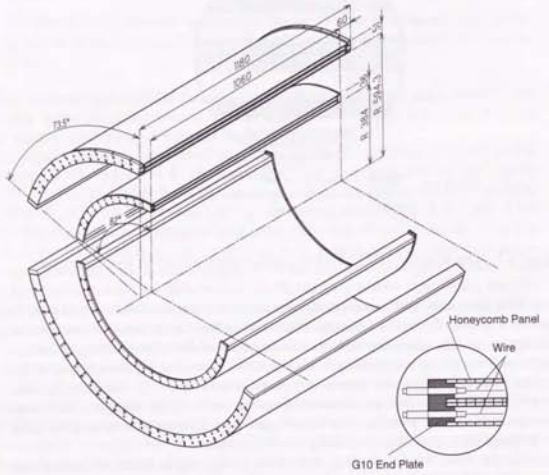

Figure 2.8: Schematic view of IDC and ODC, the upper set shows their cross sections.

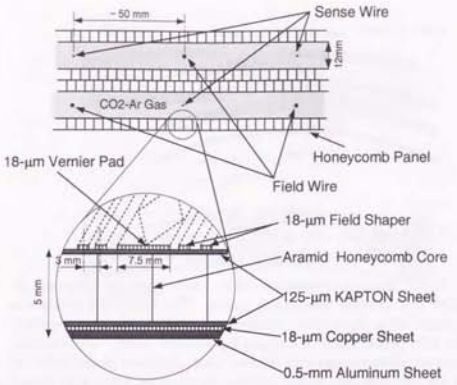

Figure 2.9: Schematic view of $r-\phi$ cross section of IDC and ODC.

olution in ϕ-direction of IDCs was about 200μm and that in z-direction was about 350μm. The z-coordinates are only determined within 10cm intervals and which interval to be taken is determined using the trajectory fitted to hit points in JET.

IDCs are 1.06-m-long and 36-mm-thick semi-cylinder type drift chambers located between JET chamber and the magnet. Surrounding JET chamber by two of them, a better resolutions in trajectory fitting is to be obtained. Each of them covers 164° in the ϕ-direction. ODCs are 1.18m-long and 44mm-thick semi-cylinder type drift chambers located outside the magnet. Each of them covers 144.57° in the ϕ-direction. Both type of chambers were designed in the same manner except for their dimensions and the measures against the magnetic field. Since the magnetic field was 1T where IDCs was situated and 0.1T where ODCs was, the Lorentz angle for drift electrons was significant only in IDCs.

Figure 2.9 shows a schematic view of the r-ϕ cross sections of IDC and ODC. Each of the chambers is composed of two layers of drift cells, which are bounded by the field and the sense wires stretched in the midst of each layer alternately at intervals of about 5cm. The arrangement of the wires were designed to be complementary between the layers, i.e. at the same ϕ-coordinate, a sense wire is to be placed in one layer and a field wire in the other. This configuration allows solving the left-right ambiguity and provides 5cm-wide hit cells which are used to produce the second level trigger(Figure 2.10). This is also used in calibrating the drift velocity, which is obtained by adjusting the sum of the drift length of both layers to the

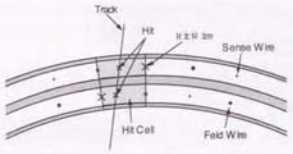

Figure 2.10: Schematic view of hits, hit wires and hit cell.

wire interval, i.e. , 5cm. The semi-cylindrical walls of each layer are composed of aramid-core and KAPTON-surface honeycomb panels. The KAPTON sheets are 125μm thick and pasted with 18μm-thick copper sheets. The walls are supported by the end and the side plates made of engineering plastics (G10). The exterior walls of the chambers are strengthened with 0.5mm-thick aluminum plates glued on them (0.3mm-thick for the outer side wall of ODCs). As the sense wires gold-plated tungsten-rhenium wires of diameter 25μm were used, and as field wires gold-plated aluminum wires of diameter 250μm. They were stretched with tensions of 55 gw and 400 gw, respectively, having been pre-stretched with tensions of 15 and 40 gw to reduce loosening due to creep. Both chambers were filled with the same gas mixture used in the JET chamber (CO_2:90%, Ar:10%).

High voltages of +2.7kV and −4.0kV was applied to the sense and the field wires of IDCs, and +2.6kV and −4.5kV to those of ODCs. Field shaping patterns (1.5mm-wide strip at intervals of 3mm) are etched on the interior surface of the walls to form flat electric fields. Figure 2.11 shows electric field in IDC. The field direction was inclined by 5.5° to the drift direction so as to compensate the Lorentz angle due to the magnetic field. The electric field in ODC was almost the same as that in IDC, with the exception that the Lorentz angle was negligibly small. The hit positions in IDCs and ODCs in the $r\phi$-plane were determined by measuring the drift time. In order to determine the z-coordinate of hits, diamond-shaped vernier pads [41] are etched on the both wall, facing to the sense wires (Figure 2.12). The pads were at a potential of 0V and mirror charges were induced on them corresponding to the charge placed on the sense wire. A vernier pad is formed on a copper strip of width 7.5mm, a pattern composed of a line of diamond shapes connected each other at their ends is etched on it. Together with the pattern composed of a line of the remaining half-diamonds outside the diamond-pattern, hit points are determined within the length of the diamonds (10cm in IDCs and 12cm in ODCs). The pattern on the inner pad (the pad on the wall of smaller raidus) and that on the outer pad are shifted by a quarter of the period of the diamond-pattern so as to be complementary to each other (Figure 2.13). When drift electrons make an avalanche near the sense wire and induce a signal on a sense wire, there also induced are the mirror charges on

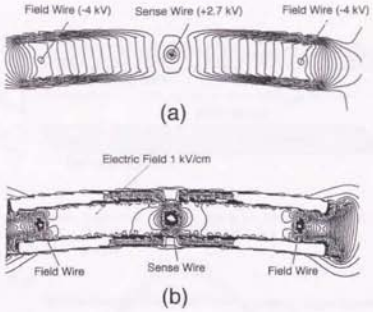

Figure 2.11: Electric field maps of IDC. (a) equipotential map. (b) field strength map.

the vernier pads facing to the wire. The charge induced on each pad is distributed on two sections of the pad; A — the central diamond pattern and B — the bounding half-diamond patterns. The normalized difference of the fractions of the charge Q_A and Q_B on the sections A and B, respectively, is a function of z:

$$\varepsilon \equiv \frac{Q_A - Q_B}{Q_A + Q_B} = 1 - \frac{|z - z_i|}{l/4}$$

where l is the length of the diamond shapes and z_i is the center of the single diamond which is the nearest to the avalanche point. The locus of the point $(\varepsilon_o, \varepsilon_i)$ is then a square with vertices $(0, \pm 1)$ and $(\pm 1, 0)$, where ε_i and ε_o are ε for the inner and the outer pad, respectively. Varying the z-coordinate from z to $z + l$, the point $(\varepsilon_o, \varepsilon_i)$ moves round the square. Figure 2.14 shows the scatter plot of the measured ε. The difference from the simple square described above is due to (i) the difference in solid angles of two sections in a pad and (ii) the non-zero width at the ends of the diamond patterns which is necessary to make connections of the patterns. The curve in the figure shows the result of the calculations taking the above effects into account. We can then derive the z-coordinate of the hit position by obtaining the closest point on the calculation curve from the measured $(\varepsilon_o, \varepsilon_i)$.

The signals from the sense wires and vernier pads are both amplified by preamplifiers mounted on the aluminum plates attached to the end-plates. The sense wires of IDCs are read out at one end, and those of ODCs are enabled at both end. Four readouts of vernier signals are equipped for one sense wire. Thus, a total of five/six

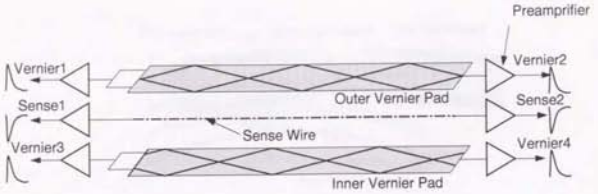

Figure 2.12: Schematic view of a set of sense wire and vernier pads.

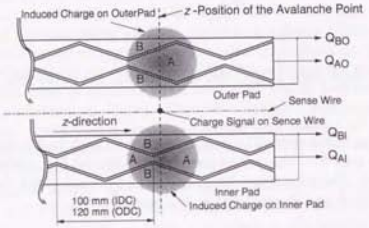

Figure 2.13: Charge induction on the diamond-shaped vernier pads.

readouts per sense wire are equipped on IDC/ODC. The signals were utilized as follows;

1. The sense wire signals were used for the second level trigger. They were fed to the modules consisting of amplifiers and discriminators and then the discriminated signals were fed to the coincidence modules. The coincidence modules output the logical products of the nearest combinations of sense wires between two layers. Thus, even if there is a signal on a sense wire, it will be discarded as a noise if there are no signals on either of two nearest sense wires in the other layer. The coincidence signals which provides a rough hit-point information with ambiguity of 5cm in width were fed to the track trigger module to produce the second level trigger (see Section 2.6.2).

2. The output of the discriminators from ODCs were also fed to the TDC modules

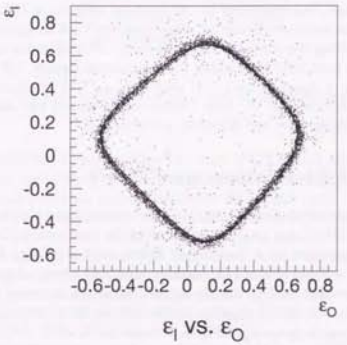

Figure 2.14: Scatter plot of the ε parameter of the inner and outer pad. The curve is the calculation for the simplified model of the charge induction on the vernier pads.

which digitized the timing of the hits with a resolution of 12 bits. The timing information was utilized for determining the hit position in the $r\phi$ plane.

3. The vernier signals of ODCs were fed to the ADC modules which integrated their charge during a gate time of 500ns and digitized them with 12-bit resolution. The charge information was used for determining the z-coordinate of the hit points.

4. The vernier signals of IDCs were fed into the FADC modules, which are the same modules as described in Section 2.2. The timing and charge informations derived from the modules are used for determining $r\phi-$ and $z-$coordinates of the hit points.

In the present experiment, the number of FADC modules assigned to IDC readout were 112, therefore the verniers of only 38 wires were read (16 in upper IDC and 22 in lower IDC), selecting the wires correspondig to the fiducial region of JET chamber, though all wires were used for making the coincidence signals. Of which 8 (10) wires in outer layer of upper (lower) IDC were assigned four channels each to determine $\phi-$ and z-coordinates of the hits. Others were assigned two channels each to determine ϕ-coordinates and less definitely z-coordinates.

2.4 Time of Flight Hodoscope (TOF)

The TOF hodoscope consists of ten plastic scintillation counters placed side by side, four of them at the top (TOFU) and six at the bottom of the instrument (TOFL). TOFU and TOFL were separated by a diameter of 130cm, and were used for the measurement of the time of flight of incident particles and their energy deposit in the scintillators. They were also used to specify the incoming and outgoing points of incident particles, which were used for the verification of the fitted trajectories.

Each scintillation counter, shown in Figure 2.15, is composed of a NE Technology NE102A scintillator with dimensions 110 cm × 20 cm × 2 cm and two Hamamatsu

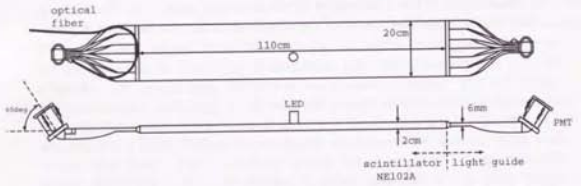

Figure 2.15: Time of flight counter.

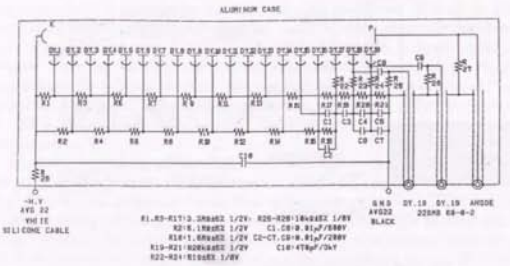

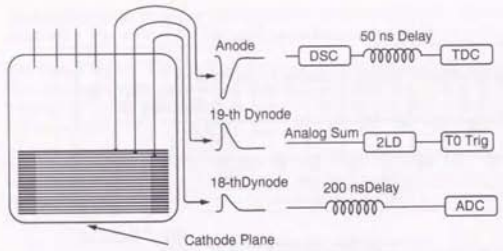

Figure 2.17: Read-out scheme PMT signals

vinyl sheet 0.1mm thick for light shielding.

The output signals of each counter were utilized in three ways; time-of-flight measurement, charge measurement and trigger. To make the time-of-flight measurement precise, three signals were extracted separately from a PMT, avoiding a possible deformation when one signal had been used for the three ways. The signals were obtained from the anodes, the 19th dynodes and the 18th dynodes of the PMTs (Figure 2.17). and used as follows:

- Time-of-flight measurement: To make it precise, the largest signal from the anodes were used for time-of-flight measurement.
- Charge measurement: The energy deposit of incident particles largely depends on their charge. To provide a wide range of charge measurement, the smallest signal from the 18th dynodes were used.
- Trigger: The 19th dynode signals were used for generating fast triggers to start digitization of read-out signals.

The signals from 19th dynodes of two PMTs of a counter are put into an analog summation circuit, and then a two-level discriminator module (2LD) which provides a source signal of the trigger module. See Section 2.6 for the details. The fast trigger signals are used for 'start' signals for TDC modules and Gate generators, the 'gate' outputs of which are used for ADC modules.

The anode signals are used to generate 'stop' signals for TDC modules. They were put into Discriminator modules and the ECL-level digital output signals of the modules were fed into the TDC modules through 50ns-delaying differential cables. The delay was necessary for the 'stop' signals to be well later than the 'start' signals which were usually produced from the same PMT signals. The threshold of the discriminators, which can be set by a CAMAC command by 0.23 mV step starting

at a minimum value of 5mV, was set to 10mV in the BESS-93 flight. Since there were some spurious hits due to electric noise, the thresholds were set to 15mV in BESS-94 flight, though the TOF resolution could be worse. The TDC modules were made by modifying Lecroy 2208 to receive ECL-level signals from the discriminator modules. They provide 11-bits of dynamic range and 50 ps/count of conversion gain. According to the calibrations done before the flight, a timing resolution of 70 ps and a linearity of 0.1% over a full scale were obtained. The time conversion gain shifted by 2.5% in the magnetic field, however, there was no effect on time resolution and linearity.

The 18th dynode signals were used for the charge measurement. They were fed into ADC modules, which were developed in KEK [42], through 200ns analog delay lines. The charges integrated during 50ns of the gate width were converted into 12-bit digital values with a conversion gain of 0.6 pC/count and a nonlinearity below 1 count over the full range. The charge produced by a minimum ionization signal of a TOF counter was about 30counts above the pedestal at about 200-250counts, thus the dynamic range of charge measurement extend from 1/20 to 120 in the units of minimum ionization signal, corresponding from $Z^2 = .2$ to 11. The intrinsic resolution of the charge measurement was 10% for minimum ionization signals, which was dominated by photo-electron statistics in the PMT.

The PMT gains and the time resolution of each counter were first calibrated before the installation into the BESS instrument, using proton and pion beams of 1GeV/c at the proton synchrotron in KEK, to determine the high-voltage to be applied to each PMT and to obtain parameters for the correction of time walk, which is dependent on the signal size. After the installation, the PMT gains, the converson gains and the ADC and TDC modules were monitored and calibrated both for the data collected on the ground and during the flight by the following three ways:

1. A laser light pulser (Hamamatsu PLP-02, wave length 410nm) was used for the precise measurement of the TDC conversion gain and timing offset for each counter in the actual operating condition. The output light was led into the light guide of a counter through a 1-mm-diameter quartz fiber. The excellent stability of the pulse height and the timing of laser pulse enabled to calibrate the timing and gain of each counter, though this calibration scheme was not available when the endcap of the pressure vessel was closed.

2. The blue light of the LED attached at the center of the counters were also used to monitor the gain and timing of the counters. Although LED signals were slower in rise-time and less stable than the laser signals, calibrations could be performed even after the pressure vessel was closed, driving the LEDs via hermetic connector terminals equipped on a side hatch of the vessel. The gain of the PMTs at both ends of a counter were calibrated simultaneously and their gain could be relatively adjusted.

3. For the data collected during the flight, cosmic-ray data themselves were to be used to determine all the calibration parameters, which were used in the

analysis. Since both the gain and the timing fluctuate depending on the temperature, the calibration parameters were determined at hourly intervals.

2.5 Čerenkov Counters

In the flight of 1994, we installed three acrylic Čerenkov counters in the istrument to identify low energy antiproton candidates more confidently. They were placed below the pressure vessel at the exterior, for there was no room for extra detectors inside, inclining to the negative deflection side to identify antiprotons. The Čerenkov counters were composed of Kuraray paraglas acrylic plates and Hamamatsu Photonics R5542SP PMTs which were produced with special care for the use in the vacuum. The plate was 3cm thick, 24 cm wide and 150 cm long including 25cm of tapering part to each end, which functioned as a light guide. The refractive index of the acrylic is 1.522 and the attenuation length 5 m both at 400 nm wave length, at the peak of the sensitivity of the PMTs, yielding a threshold velocity of $\beta \sim 0.657$, which corresponds to a rigidity of 0.817GV for protons. The R5542SP PMT has 19 stages of proximity fine-mesh dynodes and provides a high gain of about 10^7. It kept the gain in the 1.5kG magnetic field of the superconducting solenoid, the direction of which inclined 15 degrees from the axis of the PMT. The photo-cathode of the PMT is 64 mm or larger in diameter and very sensitive to faint light. Each counter was wrapped with a 20μm-thick aluminized mylar sheet for an improvement of the light collection, and a 100μm-thick black vinyl sheet to shield the counter from the external light.

A beam test was carried out at $\pi 2$ beam line of KEK PS before the installation. The result exhibited the effectiveness in proton (antiproton) identification out of the background from light particles up to 1.7GeV/c in case the particles pass through the counter with small incident angles.

2.6 Trigger

The BESS trigger system was designed for the primary objective of the BESS experiment, to detect signals of antiprotons and antiheliums efficiently. We adopted a trigger scheme biased toward negative charged particles in order to reduece the high trigger rate due to the large geometrical acceptance, in which events of protons and heliums, the dominant component of the cosmic radiation, were to be discarded and the population of negative charged particles were to be relatively enriched in the collected data. For a diagnostic purpose, samples of unbiased events were also collected and used to obtain the efficiency of the biased trigger and the fluxes of positively charged particles. The trigger system was also equipped with two other trigger modes one for a study of future experiment plan on gamma rays, and the other for external inputs used in calibrations on ground.

The BESS trigger system is composed of three trigger modules (T0 Trigger, Track Trigger and Master Trigger), and produces two level triggers (T0 and MT).

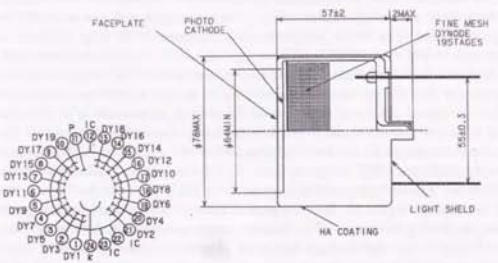

Figure 2.18: Schematic diagram of the photomultipliers for the Čerenkov counters.

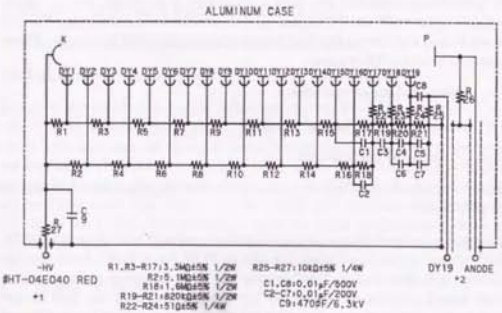

Figure 2.19: The high voltage bleeder circuit of the photomultipliers for the Čerenkov counters.

The T0 trigger module produces T0 data words and "T0" triggers from the coincidence of the signals of the TOF scintillation counters. These first level triggers are "fast" triggers to start digitizations of the read-out signals and also activate the other trigger modules. The Track Trigger module produces "TT" data words from the hit patterns in IDCs and ODCs. These signals assure that an incident particle passed through drift chambers (JET/IDCs/ODCs) while "T0" triggers do not, though they are rather slower because of drift time in drift chambers and cannot be used as "fast" triggers. The main purpose of Track Trigger module is to bias the events to be collected toward those of negatively charged particles. The sign of the deflection of incident particles are to be determined by the hit patterns. The Master trigger module produces "MT" triggers from T0 data words and TT data words, some of which are "biased" triggers for negatively charged particles and others are "unbiased" sampling triggers of "T0" triggers. These are the second level triggers to start data gathering processes. The Master trigger module also produces "fast clear" signals to stop the digitizations and reset the read-out and the trigger modules in case that a "MT" trigger is not produced after the system is activated by a "T0" trigger.

2.6.1 T0 Trigger

The T0 triggers are the first level or "fast" triggers to start the read-out electronics digitizing the signals. Which are produced in the T0 trigger module from the signals of the TOF scintillation counters, and once a T0 trigger is produced, no T0 trigger will be produced again until the T0 trigger module is reset by a clear pulse, i.e. the T0 triggers are locked out during the digitizing and data gathering processes. There are four modes to produce T0 triggers:

- Low — aiming at charged particles.
- High — aiming at $Z \geq 2$ charged particles.
- Gamma — aiming at gamma-rays.
- External — initiated by an input signal and used for diagnoses and calibrations of the instrument.

A "Low" trigger is produced from a simple coincidence of a TOFU hit and a TOFL hit. A "High" trigger is produced when the hits in TOFU and TOFL both provide high amplitudes. It is clear that a "Low" trigger will be produced at the same time. A gamma-ray would possibly be converted into an electron-positron pair at the coil of the magnet and detected at the drift chambers and the TOFL scintillation counters. In such a case, there are no hits in TOFU and some hits in TOFL. A "Gamma" trigger is produced from a TOFL hit using TOFU hits as vetoes.

The signals from two ends of a TOF counter are different in timing and amplitude depending on the z-coordinate of the impact point of the incident particle. The timing difference reaches about 6ns and the amplitude ratio about 3. This feature can be used to check consistency with the trajectory of the particle obtained from

the hits in drift chambers. However, to make a trigger, we need a confident signal from a counter to indicate a hit, and require both signals from two ends. In addition, as mentioned above, the trigger scheme is pulse-height dependent and the source signals for the trigger are desired to be independent of the hit points. The signals from 19th dynodes of two PMTs of a counter are put into an analog summation circuit, where each signal is integrated with a time constant 20ns and the signals are summed up into an output signal. The summed signals are fed into the two-level discriminator (2LD) modules, in which two thresholds are set for all eight input channels. The lower thresholds were set to be 30 mV, which corresponds to half of the pulse height of signals from minimum ionizations. The higher were set so as to descriminate $Z \geq 2$ particles. They were set to be 150mV in BESS-93 flight and optimized for individual PMTs before the BESS-94 flight using the BESS-93 flight data, varying from 160mV to 250mV corresponding to the variation of PMT gains, A 2LD module provides two output signals "Low" and "High", corresponding to the two level thresholds. For each of the thresholds, the logical "OR" of the descriminated signals of the eight channels makes an output signal. There used two 2LD modules, one for 4 TOFU counters and the other for 6 TOFL counters, and 4 output signals were provided.

The T0 trigger module used the four signals of 2LD modules to produce T0 triggers by following logics;

- T0-Low — TOFU·2LD-Low $\wedge$ TOFL·2LD-Low
- T0-High — TOFU·2LD-High $\wedge$ TOFL·2LD-High
- T0-Gamma — $\overline{\text{TOFU·2LD-Low}}$ $\wedge$ TOFL·2LD-Low
- T0-External — External input

The module is equipped with trigger reduction circuits for all four modes to be used when the T0 trigger rate is too high. The reduction rates 1/N are set by a CAMAC command, and they can be changed even during the flight. In the experiment, since we activated T0-Gamma mode only for a study of the gamma-ray triggering, and the trigger rate for the mode is about the sum of the single rate of the TOFL counters reaching a too high rate of about 20kHz, the reduction rate for the mode was selected to be 1/256. The reduction rates for other trigger modes were set to 1/1, i.e. no reduction, and not needed to be changed during the experiment.

2.6.2 Track Trigger

The Track Trigger module provides the TT data words from the hit pattern of IDCs and ODCs, which were used to produce the triggers "biased" toward negative charged particles. In Fig 2.20 is shown the basic concept of the TT. The signal of the sense wires of IDCs and ODCs are discriminated and fed into the coincidence modules. They are then combined into "hit-cell" signals by requiring the coincidence of two nearest wires in different layers of each IDC/ODC by which spurious hits caused by electric noise or by radiations from local radio-activated materials are

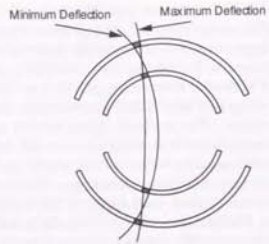

Figure 2.20: Basic scheme of the Track Trigger.

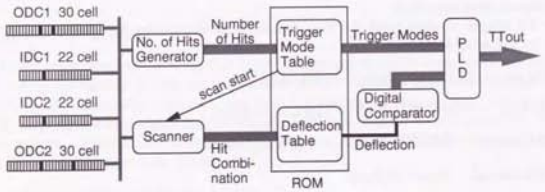

Figure 2.21: Block diagram of TT process.

eliminated, and the width of the possible range of the hit points are halved. Total of 30 and 22 cells are defined in each ODC and IDC, respectively. The hit-cells give coarse hit position information with a resolution of the cell width, i.e. about 50mm, and a combination of three or four hit-cells from four drift chambers provides rough estimation of the deflection ($\equiv$ rigidity^{-1}) of the incident particle. The two trajectories in Figure 2.20 are shown to illustrate the possible maximum and minimum deflections for a certain combination of hit-cells. We define the mean value of two deflections as a deflection of the hit-cell combination. By calculating the deflection for all hit-cell combinations, and storing them in a look-up table beforehand, a quick deflection analysis is possible without any time-consuming calculation.

The Track Trigger module consists of a 2Mbyte read only memory (ROM) as the look-up table and a microcode-programmable sequencer, and carries out the event selection by their deflection (Figure 2.21). The selection scheme can be programmed with 8 modes and output data of the module are 8-bit data words corresponding to

them. The modes were programmed as follows;

- Mode 1: *$\bar{p}$-severe* — A mode to select antiprotons. The numbers of hit cells in the four drift chambers are strictly limited.
- Mode 2: *$\bar{p}$-loose* — A mode to select antiprotons. The numbers of hit cells in the four drift chambers are less limited.
- Mode 3: *$\overline{He}$-severe* — A mode to select antiheliums. The numbers of hit cells in the four drift chambers are strictly limited.
- Mode 4: *$\overline{He}$-loose* — A mode to select antiheliums. The numbers of hit cells in the four drift chambers are less restricted.
- Mode 5: *Missing-a-hit* — A mode to select negatively charged particles with only three hit cells in four chambers. The chambers have some 'dead' region near the sense wires for the signals of the hits near the wires are fed into the electronics earlier than the trigger activates them. The events of negatively charged particles with such a 'missing hit' can be selected here.
- Mode 6: *Multi-hit 1* — A mode to select negatively charged particles which could not selected the modes above. This time extra hits due to noise or interactions are considered.
- Mode 7: *Multi-hit 2* — The same as Mode 6. The number of extra hits are less restricted.
- Mode 8: *Gamma* — A mode to select gamma-ray events in which the incident gamma-ray is converted into a electron-positron pair, making hits in two IDCs and the bottom ODC.

The selections are performed in two stages, number-of-hits selection and deflection selection.

number-of-hits selection

Events with too few or too many hit cells were eliminated before examining the deflection of tracks. Most of the events with showers or without tracks in JET chamber were rejected by this selection. Different selection conditions were set for the individual selection modes. The "number of hits generator" logic circuit yields the total number of hit-cells of each drift chamber, the set of which makes a address of the "Trigger Mode Table", which is stored in a half of the ROM look-up table. The combinations and the permutations of the numbers of hit-cells are examined by this table and resulting Trigger Mode bits are produced. The number of hits conditions for each trigger mode are summarized in Table 2.3. If any of the number-of-hits selection conditions is satisfied, a "scan-start" will be issued to the scanner so as to initiate the deflection selection.

Table 2.3: The conditions of the Track Trigger Nhit selection. C(i,j,k,l) means any combination of N_{i1},N_{i2},N_{o1},N_{o2} matches (i,j,k,l) and P(i,j,k,l) means the permutation (N_{iu},N_{il},N_{ou},N_{ol}) matches (i,j,k,l), where N_{iu} – the number of hit-cels in upper IDC, N_{il} – the number of hit-cels in lower IDC, N_{ou} – the number of hit-cels in upper ODC, N_{ol} – the number of hit-cels in lower ODC.

Mode	BESS-93	BESS-94
1	C(1,1,1,1)	C(1,1,1,1), C(1,1,1,2)
2	C(1,1,1,2)	C(1,1,1,3), C(1,1,2,2)
3	C(1,1,1,1)	C(1,1,1,1), C(1,1,1,2)
4	C(1,1,1,2)	C(1,1,1,3), C(1,1,2,2) C(1,1,2,3), C(1,2,2,2) C(1,2,2,3), C(2,2,2,2) C(1,1,3,3)
5	C(0,1,1,1)	C(1,1,1,1), C(1,1,1,2)
6	P(1,1,1,i),(i=3,4) P(1,1,2,j),(j=2,3,4)	P(1,1,i,j),(i,j=1,2,3,4)
7	P(2,i,j,k),(i=1,2) (j=1,2,3),(k=1,2,3,4) except for P(2,1,1,1)	—
8	P(0,i,j,k) (i,j,k=1,2)	P(0,i,j,k) (i,j,k=1,2)

deflection selection

The events that have passed through the number-of-hits selection are then subject to the deflection selection. All possible combinations of hit-cells are scanned and the pattern of the four hits (one hit in each drift chamber) makes an address to refer the "Deflection Table", which is stored in the other half of the ROM look-up table. The output deflection is compared with the seven threshold values, each of which corresponds to one of the selection modes, except that the thresholds for Multi-clear and Multi-dirty are common. If the deflection is above some of the thresholds, i.e., the track has more negative deflection than the threshold, a bit correspondig to the mode in the TT output data word is asserted.

The Mode 2 and 4 ($\bar{p}$ and $\overline{\mathrm{He}}$ loose) were less accurate in deflection resolution than Mode 1 and 3, and their deflection threshold were set higher than that of Mode 1 and 3. Since the population of heliums in the cosmic rays are less than protons, the deflection threshold of Mode 3 and 4 were set looser than that of Mode 1 and 2. The Mode 6 and 7 in BESS-93 flight were prepared as an insurance against the case that the Mode 1 to 4 did not work well. In fact, the efficiency of the number-of-hits selection was very low because of much more extra hits than expected, which were produce by cross-talks. In BESS-94 flight, the thresholds of the discriminators were tuned and the number-of-hits conditions were less strict, the efficiency was much higher than in BESS-93 flight. The Mode 6 was used especially aiming to select antiprotons which annihilated at the bottom of the instrument.

Figure 2.22 shows the efficiency of the rigidity selection as a function of deflection calculated by the simulation. The threshold values indicate the deflections where the efficiency become 50%. The left figure is for the threshold used for the $\bar{p}$ selection in the BESS-93 flight. The right figure is for the threshold used for an antihelium selection. The curve for the $\bar{p}$ selection is set being shifted to the negative direction compared to that for the antihelium selection because a large number of protons should be cut more tightly by the rigidity selection.

2.6.3 Master Trigger and Fast Clear

The Track Trigger module only concerns the number of hit-cells and deflection of the particles. The Master trigger module combines the signal size information from the T0 Trigger module, with which protons and heliums are discriminated, and the track information from the Track Trigger module, with which the signs of the charge of the particles are discriminated. Here the categorizaion $\bar{p}$ and $\overline{\mathrm{He}}$ in the Track Trigger module are added the real sense. The Master Trigger module also generates unbiased triggers by sampling the T0 Trigger at a rate. There equipped 12 sampling circuits corresponding to 4 T0 Trigger modes and 8 Track Trigger modes. In a sampling circuit is used a count down IC, and loading a number N to it, a reduction rate $1/(N+1)$ will be obtained. The MT trigger is generated as the logical 'OR' of the twelve modes. If no MT trigger is generated, a fast clear signal is issued to the "Fast Clear" module. The Fast Clear module issues clear signal to all read-out electronics and then clear the lock-out of the T0 Trigger module making the system ready for

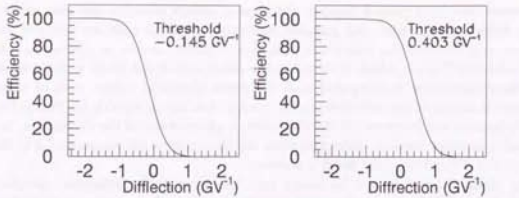

Figure 2.22: Simulated Track Trigger efficiency. (a) for the $\bar{p}$ search (b) for the antihelium search.

the next event.

2.7 Data Acquisition System

The BESS data acquisition system is required to handle a high trigger rate of about 2kHz due to the large geometrical acceptance and a large data size of about 1.2kbytes per event yielded by the large number of signal read out. The system has a capability to gather the data of each single event within 1.2ms, utilizing multi-processor and pipe-line scheme, and to store the data up to 10Gbytes with a recording rate of 500kbytes/s [44]. Thus, it is necessary to reduce the trigger rate down to a few hundred hertz so as to restrain the dead-time of the system at an approvable amount. As described in Section 2.6, the trigger system is capable to reduce the second level (MT) trigger rate. The parameters of reduction scheme are adjusted to make a MT trigger rate of about 100 to 200 Hz.

It is also important for a balloon-borne experiment to reduce the power consumption. The amount of batteries possible to be loaded is limited in view of the maximum total weight of the payload. A larger power consumption demands more batteries resulting in a smaller margin of the weight, or shortens the exposure time of the experiment. It also produces a larger amount of heat in the instrument and causes a cooling problem. To avoid these problems, most of the electronics are self-made or custom-made being reduced in power consumption while retaining the processing speed and desired resolutions.

Figure 2.23 shows schematic view of the BESS data acquisition system. The system is composed of four subsystems which function as follows:

- Communication subsystem manages the communication between the data acquisition system on-board and the ground system. It receives the commands from the ground system and deliver them to the proper subsystem. It also receives the data and the messages from the subsystems and send them to the ground system.
- Monitor subsystem gathers the house-keeping data such as temperatures and pressures inside and outside of the instrument.
- Event process subsystem gathers the event data and make event frames, then perform the on-line software reduction of the data.
- Data storage subsystem records the event data and house-keeping data gathered by the Event process subsystem and the Monitor subsystem, and also the commands and messages the Communication subsystem receives.

The four subsystems are linked with each other by a serial bus line composing a local network based on Corvus Omni-net protocol.

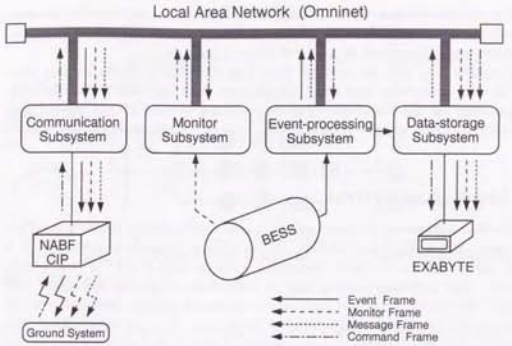

Figure 2.23: Schematic diagram of the data acquisition system

2.7.1 Communication subsystem

The Communication subsystem is constructed in a STD-bus crate and controlled by a NEC V40 (μPD70208) CPU on a Yamashita Systems CMOS CPU-F microcomputer board [46]. It interfaces with the command/telemetry device provided by NSBF (the consolidated instrument package; CIP), and with the Omni-net bus. The commands transmitted from the ground station to the payload are received by

CIP, from which 16-bit data words are supplied with a strobe signal. The communication subsystem takes in those signals via photo-couplers for electrical isolation. The command words were sent at a rate of about 1 word/s.

The telemetry data such as messages from four subsystems, house keeping data from the Monitor subsystem, and event sample data from the Data process subsystem are gathered via the Omni-net. The data are fed to the CIP via a serial line and transmitted to the ground station. The capacity of the transmission was 10 kbyte/s.

2.7.2 Monitor subsystem

The Monitor subsystem is composed of a controller module constructed in a STD-bus crate and a digitizing module. The controller module is governed by a NEC V40 (μPD70208) CPU on a Yamashita Systems CMOS CPU-F microcomputer board. The dizitizing module has 64 individual differential-amplifiers and one analog-to-digital converter and digitize various sensor signals: temperatures (16 points), pressures (10 points), magnet status (16 points), chamber high voltage status (10 points), and solar sensors and clinometers. The digitized data are sent to the Communication subsystem as telemetry data, and to the Data storage subsystem so as to be recorded in the magnetic tapes. Thus, the house-keeping data can be monitored during the flight as well as can be used in the off-line analysis.

2.7.3 Event Process subsystem

Figure 2.24 shows the block diagram of the Event Process subsystem together with the Data Storage subsystem. The main function of the subsystem is realized by INMOS transputers (shadowed boxes in the figure), which have a processing speed of 20 MIPS and a capability of parallel processing realized by hardware. The interfaces with the Omni-net is realized by Mikasa System Engineering pro216/II microcomputer board on which a NEC V50 (μPD70216) CPU is installed. The transputers are connected by point-to-point serial links, which has maximum transmission rate of 1 Mbyte/s. Four such links are equipped in each transputer and a complicated network can be constructed easily with a flexible configuration.

The signals from the detectors are fed into the ADC and TDC modules in the two CAMAC crates and FADC modules in the FADC crate. The CAMAC and FADC crate controllers are self-made using a transputer in each of them, and gathers the digitized read-out signals in parallel. The FADC crate controller also functions as the event builder (EVB) and makes the event frames, packing the digitized data received from the CAMAC crate controllers with the FADC data. The event frames are fed into the transputer bank, where a single transputer processes the data, driven by the data, and functions as a filter. Thus, 9 events are possible to be processed at a time and the next event data can be gathered while the transputer bank is processing the previous event data. The number of transputers in the bank can be increased if necessary. The command links in the transputer bank is separated from the event data links, therefore the full band width of the event data links can be

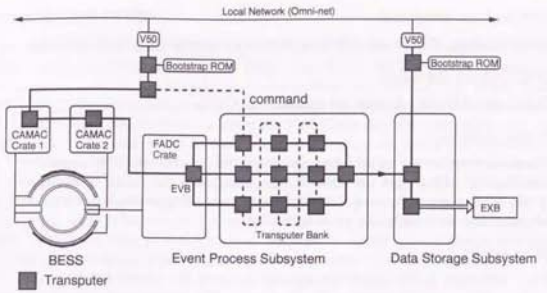

Figure 2.24: The block diagram of the Data Process and the Data Storage subsystem. A net work of transputers are constructed for the main function of the subsystems.

utilized by the event frame flow. The data transmission by point-to-point links has an advantage that no arbitration method is needed.

CDC crates

The signals from the sense wires of IDCs and ODCs are fed into the CDC crates, where the amplifiers, the discriminators and the coincidence circuits are installed. The input signals from the drift chambers are amplified and then fed to the discriminators. The output signal of the discriminators are used as the input signals of the coincidence modules and also as the stop signals for the TDC modules in the CAMAC crate. The coincidence signals are used as the input to the Track Trigger module, providing the hit-cell information. The thresholds of the discriminators were too low in BESS-93, and as a result, there were noise hits in coincidence signals due to the cross-talks. This caused a lower efficiency of the Track Trigger in BESS-93.

CAMAC crates

Two CAMAC crates are used in the data acquisition system and contain the read-out modules such as ADCs and TDCs, and the trigger modules. Each crate is controlled by an intelligent crate-controller equipped with a transputer [45]. Thus, the data digitized at the modules in the CAMAC crates are gathered in parallel by the two crate controllers. The initial set up of the modules are also done by the crate controllers automatically. The modules installed in the CAMAC crates are:

- TOF read-out electronics

  Discriminators, TDCs, and ADCs to digitize the signals from TOF counters.

- ODC read-out electronics

  TDCs, and ADCs to digitize the signals from ODCs

- Trigger modules

  Discriminators for the signals from the scintillation counters (TOF counters) and T0, TT, MT trigger modules. Trigger conditions can be set or changed by the crate controller, using CAMAC commands. Trigger modes and other informations are read by the crate controller.

- 24-bit scalers

  Two 12-channel 24-bit scalers are installed to count the numbers such as the number of triggers, the number of coincidences. The trigger rates, the trigger efficiencies, and the dead time are derived using the scaler data. The scaler data are read only once a second to reduce the total data amount and the data gathering time.

- Event-timing module

  An event-timing module with a 0.1ms resolution is installed to obtain the time when the events are occurred.

- Gate generators

  Gate generators to make the gates for ADCs, the start pulses for TDCs and clear pulses for the adequate modules.

The data read from the modules are packed in the crate controllers and are transferred to the Event Builder via serial links. The CAMAC data of a single event amounts to about 300 bytes.

FADC crate

In the FADC crate are installed FADC modules, a compressor module, and a crate controller [43]. The signals from JET chamber and the vernier signals from IDCs are fed into FADC modules, and digitized with 8-bit resolution and 35-ns sampling period. The digitized values are stored into fast-in-fast-out (FIFO) memories after the zero-suppression process. The compressor module compresses the FADC data read from the FIFO's and extract the information of each pulse, such as timing, width, total charge, and the first two signal height data with which the pulse height can be estimated. The pulse information data are stored into the FIFO on the compressor module, and then read by the crate controller.

The FADC data of a single event amounts to about 700-900 bytes and are transferred to the Event Builder via the internal memory bus, since the Event Builder process runs on the FADC crate controller.

Event Builder (EVB)

The data collected in parallel in the two CAMAC crates are transferred to the FADC crate controller via the serial links. The Event Builder process running in the transputer of the FADC crate controller gathers the CAMAC and FADC data, and packs them into a event frame. After packing the data, the Event Builder clears the CAMAC and FADC modules using the Fast Clear module, and prepare for the next event. Then, one of three data transferring processes sends the event frame to the transputer bank via the corresponding serial link. The data transferring processes run in parallel to each other, and also to the data gathering and event building processes. Thus, the event gathering and event building processes can be active even when a huge event or two take time to be transferred to the transputer bank. The event data of a single event amounts to about 1.0-1.2 kbytes typically and the event building process completes within 1.2ms from the T0 trigger.

Transputer Bank

The role of the transputer bank is a event-driven filter to sieve the events using the detector informations. It contains nine transputers (fifteen or more can be installed if necessary), arranged in three-by-three array (or three-by-n) and receives the event frames from the Event Builder via three serial links. All the transputers are programmed the same, and the individual transputer processes one event at a time. Thus, nine events can be processed in parallel.

The filtering process removes the junk events with too much FADC data, that is, with too many hits in JET chamber and IDC, and the events in which ODC hits and TOF hits are inconsistent. About 2% of the events were removed by this process, and the numbers of events removed in these categories are added to the scaler data and also sent to the ground system. The process also removes the overflowed TDC data which do not contain hit informations, and reduce the event data size. The whole process completes within at most 20ms and the transputer bank can handle 450 events per second.

In future the filter process will be more sophisticated in order to reduce the number of events to be recorded more effectively, and thus, to loosen the Track Trigger selection conditions. The reduction methods are in study using the real flight data.

2.7.4 Data Storage subsystem

In a part of Figure 2.24 is shown the Data Storage subsystem. In the subsystem the data frames received from other subsystems are recorded into cartridge tapes. A Mikasa System Engineering pro216/II microcomputer board with NEC V50 (μPD70216) CPU was employed for the communication via OMNI net. Transputer modules are employed for the main tasks of the data storage, one of which was a module specialized for the SCSI bus control. The monitor frames and the message frames are transferred via Omni-net, while the event frames are via a serial link which connected a transputer in the Data Process subsystem to another in

the Data Storage subsystem. Two EXABYTE EXB-8500 8mm tape data recorders were employed as the storage devices. The capacity of the tapes was 5 Gbytes each, providing 10 Gbytes of storage capacity in two tapes. The maximum data recording speed was 500 kbytes/s.

Chapter 3

Flight

The BESS apparatus was launched from Lynn Lake, Manitoba Canada in the evening of July 26. of 1993, and of July 31. of 1994 [47] close to the solar minimum as shown in Figure 3.1. The payload was lifted by a $8.3\times10^5 m^3$ ($2.9\times10^7 ft^3$) balloon filled with helium. The suspended weight was 2,700 kg consisting of 2,060 kg BESS apparatus, 330 kg ballast and others. The payload achieved a float altitude of 36 km, corresponding to 5 g/cm^2 of residual atmosphere above, for a duration of 17 hours. During the level flight, as shown in Figure 3.2, the latitude varied between 56°48'N and 57°52'N, while the longitude varied between 101°25'W and 117°30'W in the flight of 1993, and the latitude varied between 55°41'N and 56°04'N, while the longitude varied between 101°03'W and 114°15'W in 1994 flight. Over these flights, the magnetic cut-off rigidity seemed to be lower than the instrumental cut-off, for there were no significant changes in the spectral shape of the proton flux obtained in the analysis. The payload landed near High Level in 1993 and near Slave Lake in 1994, both in Alberta, after drifting 900 - 1000 km during 21 hours and 23 hours of flight respectively. The environment in the pressure vessel was kept in good state, as shown in Figure 3.3, 3.4, the temperature of JET drift chamber was kept within 9.5°C and 35.8°C and the pressure was kept within 1120g/cm^2 and 1200g/cm^2 in 1993. Adjusting the insulations made a better environment in 1994, the temperature within 17.5°C and 32.2°C and the pressure within 1170g/cm^2 and 1230g/cm^2.

The BESS instrument was activated for 14 hours in 1993 flight and for 16 hours in 1994 flight, including short run for trigger tuning, actual data acquisition run, and calibration run. Trigger parameters (T0 sampling rate and TT thresholds) were carefully adjusted to achieve the desired trigger rate, based on the trigger rate obtained in the short pilot run just before the level flight. The actual trigger rate derived from the scaler data was 83 to 92 Hz in 1993 flight, 139 to 142 Hz in the first half of 1994 flight, and 100 to 104 Hz in the second half, while the T0 coincidence rate was 2.3 to 2.4 kHz in 1993 and 2.3 kHz in 1994. A calibration run of 5 to 10 minutes was carried out every hour to re-adjust the thresholds for FADC data suppression as low as possible, while the pedestal value of FADC outputs varied depending on temperature. During the data acquisition run of 11.7 hours (1993 flight) and 11.1hours (1994 flight), 3.6×10^6 events and 4.8×10^6 events were recorded, while 9.97×10^7 and 9.35×10^7 of cosmic rays made coincidence at the T0 level, and of

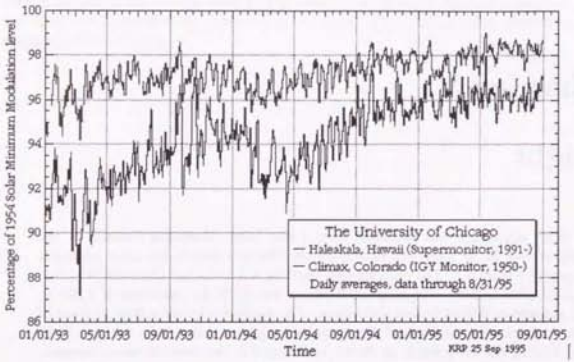

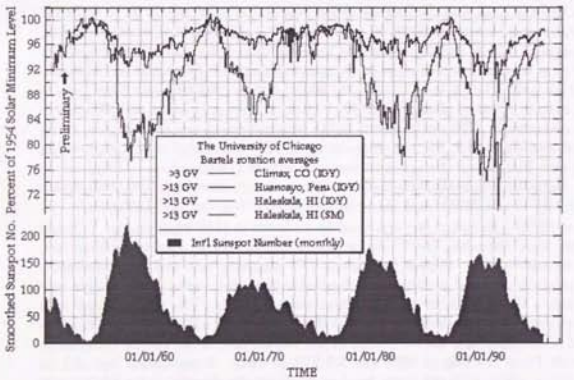

Figure 3.1: The data of neutron monitors provided by the University of Chicago.

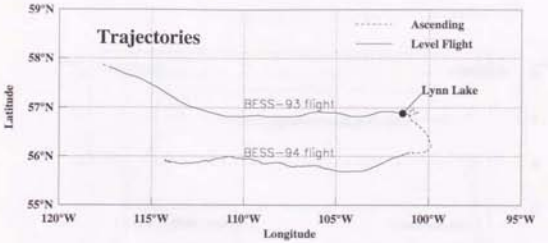

Figure 3.2: BESS-93 and BESS-94 flight trajectory in longitude and latitude

which 7.27×10^7 and 6.14×10^7 made T0 trigger. The 'live time' or effective exposure time can be derived from the ratio of T0 trigger to T0 coincidence, 73.0% and 65.7%, as 3.1×10^4sec (8.6 hours) and 2.6×10^4sec (7.3 hours). The 'dead time' consisted of decision time before fast clear, ($80\mu s \times 2.3$ kHz = 18%), and process time of data acuisition, (1 ms $\times$ 90 Hz = 0.09). The amount of the data recorded during the experiments were 4.8Gbytes (5.2×10^9bytes) and 8.2Gbytes (8.8×10^9bytes).

Table 3.1 summarizes the T0 trigger, and Table 3.2 summarizes the Master trigger (MT).

Table 3.1: The conditions of the T0 trigger and the trigger rates.

	TOFU		TOFL		Ext	Sample	Accept	T0
Mode	Low	High	Low	High		Rate	Rate	Trigger
T0 Low	1	x	1	x	x	1/1	2.3 kHz	1.7 KHz
T0 High	x	1	x	1	x	1/1	660 Hz	610 Hz
T0 gamma	0	0	1	x	x	1/256	19 kHz	75 Hz
T0 extern	x	x	x	x	1	1/1	0 Hz	0 Hz
Total							2.4 kHz	1.7 kHz

1 : Signal should be asserted.
0 : Signal should not be asserted.
x : Signal is not concerned.

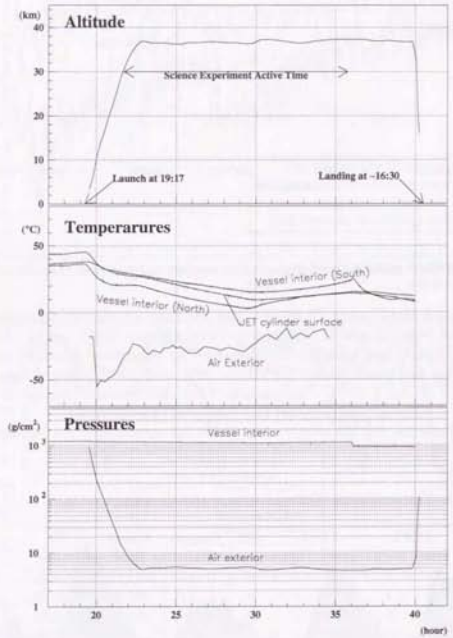

Figure 3.3: House-keeping data on altitude, temperatures and pressures in BESS-93 flight.

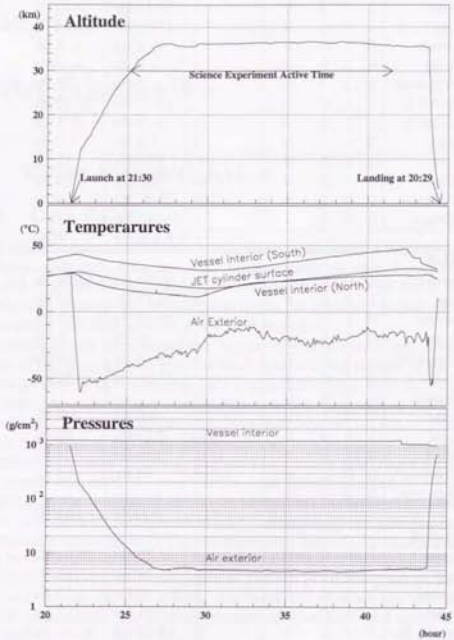

Figure 3.4: House-keeping data on altitude, temperatures and pressures in BESS-94 flight.

Table 3.2: The settings of the Master Trigger and the trigger rate.

	MT Mode	T0 Mode Mask				Sampling	Accepted	Triggered
Flight 93								
Biased	$\bar{p}$ severe	1	0	0	0	1	12-14 Hz	9-10 Hz
	$\bar{p}$ loose	1	0	0	0	1	17-19 Hz	13-14 Hz
	$\overline{\text{He}}$ severe	0	1	0	0	1	2- 3 Hz	1- 2 Hz
	$\overline{\text{He}}$ loose	0	1	0	0	1	5- 7 Hz	4- 5 Hz
	Missing-a-hit	1	1	0	0	1	3 Hz	2 Hz
	Multi-hit 1	1	1	0	0	1	14-17 Hz	10-12 Hz
	Multi-hit 2	1	1	0	0	1	7- 9 Hz	5- 7 Hz
	Gamma	0	0	1	0	1	0.6 Hz	0.4 Hz
Unbiased	T0 Low	1	0	0	0	1/140	2.3 kHz	12 Hz
	T0 High	0	1	0	0	1/40	650 Hz	12 Hz
	T0 Gamma	0	0	1	0	1/100	72-75 Hz	0.5 Hz
	T0 Extern	0	0	0	1	1	—	—
Total							2.3-2.4kHz	87Hz
Flight 94 First Half								
Biased	$\bar{p}$ severe	1	0	0	0	1	35-39 Hz	22-24 Hz
	$\bar{p}$ loose	1	0	0	0	1	16-17 Hz	10 Hz
	$\overline{\text{He}}$ severe	0	1	0	0	1	13-14 Hz	8-9 Hz
	$\overline{\text{He}}$ loose	0	1	0	0	1	10 Hz	6 Hz
	Missing-a-hit	1	1	0	0	1	11-14 Hz	7-9 Hz
	Multi-hit 1	1	1	0	0	1	37-39 Hz	23-25 Hz
	Undefined	1	1	0	0	1	—	—
	Gamma	0	0	1	0	1	0.9 Hz	0.6 Hz
Unbiased	T0 Low	1	0	0	0	1/60	2.2 kHz	23 Hz
	T0 High	0	1	0	0	1/15	340 Hz	14 Hz
	T0 Gamma	0	0	1	0	1/100	70 Hz	0.4 Hz
	T0 External	0	0	0	1	1	—	—
Total							2.3kHz	140kHz
Flight 94 Second Half								
Biased	$\bar{p}$ severe	1	0	0	0	1	34-36 Hz	24-25 Hz
	$\bar{p}$ loose	1	0	0	0	1	16 Hz	11 Hz
	$\overline{\text{He}}$ severe	0	1	0	0	1	16 Hz	11 Hz
	$\overline{\text{He}}$ loose	0	1	0	0	1	11 Hz	7 Hz
	Missing-a-hit	1	1	0	0	0	16-19 Hz	11-13 Hz
	Multi-hit 1	1	1	0	0	1/2	37-39 Hz	25-27 Hz
	Undefined	1	1	0	0	1/2	—	—
	Gamma	0	0	1	0	1	1 Hz	0.7 Hz
Unbiased	T0 Low	1	0	0	0	1/120	2.3 kHz	13 Hz
	T0 High	0	1	0	0	1/30	320 Hz	7 Hz
	T0 Gamma	0	0	1	0	1/100	70 Hz	0.5 Hz
	T0 External	0	0	0	1	1	—	—
Total							2.3kHz	100 Hz

Chapter 4

Data Analysis

4.1 Event Reconstruction

4.1.1 Data Extraction

As already mentioned in Chapter 3, the data acquisition was stopped every hour to take some calibration data, yielding 12 data acquisition runs in each flight of 1993 and 1994. The off-line calibrations were made on each run to derive temperature-dependent or pressure-dependent parameters, for instance, timing offsets in TOF measurement and drift velocity in the drift chambers.

In Table 4.1 are summarized the number of events in each run, where T0 is the number of the T0 triggers at the first level, Master is the number of the MT trigger, i.e., the number of the events the data acquisition system collected. The right half of the table shows the trigger modes of the recorded data, each of which corresponds to the Master Trigger mode (see also Table 3.2).

The first step of the data processing was to decompress the raw flight data and extract properties of hits in detector components and trigger conditions. The event frames had different sizes varying from several hundred to three kilo bytes depending on the number of hits in detectors, and variable length data format is needed. The ZEBRA [48] system of CERN program library was employed to store the properties extracted from the raw flight data, since its dynamic data structuring capability with tree structures of data storage units and linkage of these structures. The HEPDB [49] database management package of CERN program library, which is available in the ZEBRA system, was employed to store the geometries of the detector components, the read-out channel assignment tables and the calibration parameters.

Primary calibrations were performed to obtain pedestals and gain factors. After initial calibrations, pattern recognition was performed using the hits of JET chamber to find tracks of the incident particles and track infomation banks are formed. The hits of IDC, ODC and TOF made by the particle were acquired by extrapolating the fitted trajectory of the track and then linked to the track information bank. Thus, all informations of the hits which an incident particle induced on the detectors were to be retrieved by accessing the track information bank, and the properties of the

Table 4.1: The data amount in the BESS flights.

run #	time ($\times 10^3$s)	T0 ($\times 10^6$)	Master ($\times 10^5$)	Record ($\times 10^5$)	T0 L ($\times 10^4$)	T0 H ($\times 10^4$)	MT $\bar{p}$ ($\times 10^4$)	MT $\overline{\text{He}}$ ($\times 10^4$)
93-13	3.29	5.82	2.89	2.84	4.09	4.19	10.14	2.87
14	2.80	4.95	2.45	2.41	3.49	3.57	8.74	2.49
15	3.80	6.70	3.31	3.25	4.71	4.81	11.75	3.29
16	2.90	5.11	2.51	2.48	3.60	3.66	8.88	2.46
17	3.54	6.25	2.98	2.94	4.40	4.46	10.45	2.83
18	4.21	7.38	3.50	3.44	5.22	5.24	12.12	3.21
19	4.06	6.93	3.44	3.39	4.89	4.90	11.21	2.77
20	4.58	7.73	3.90	3.83	5.47	5.48	13.65	3.65
21	3.46	5.89	3.09	3.04	4.15	4.14	10.83	3.02
22	2.16	3.67	1.93	1.90	2.59	2.55	6.73	1.93
23	3.53	5.41	2.88	3.15	4.24	4.18	11.15	3.22
24	4.06	6.89	3.74	3.68	4.85	4.74	13.54	3.95
93-total	42.39	72.73	36.63	36.35	51.71	51.92	129.19	35.68
94-6	3.81	5.51	5.37	5.26	9.29	5.32	20.54	6.13
7	3.21	4.66	4.55	4.45	7.85	4.56	17.14	5.27
8	3.04	4.42	4.31	4.22	7.46	4.30	16.15	4.95
9	3.32	4.72	4.62	4.52	7.95	4.62	17.18	5.41
10	3.74	5.41	5.24	5.11	9.12	5.30	19.03	6.09
13	2.16	3.16	3.01	2.93	5.31	3.08	10.54	3.57
15	3.11	4.98	3.24	3.18	4.12	2.36	15.90	5.86
16	5.44	8.76	5.54	5.45	7.24	4.06	26.92	10.21
17	3.14	5.00	3.14	3.08	4.12	2.28	15.11	5.86
18	2.34	3.80	2.36	2.32	3.13	1.69	11.39	4.40
19	3.50	5.67	3.52	3.45	4.70	2.51	16.91	6.58
20	3.27	5.33	3.30	3.24	4.41	2.33	15.90	6.14
94-total	40.08	61.43	48.18	47.21	74.70	42.41	202.71	70.47
Total	82.47	134.16	84.81	83.56	126.41	94.33	331.90	106.15

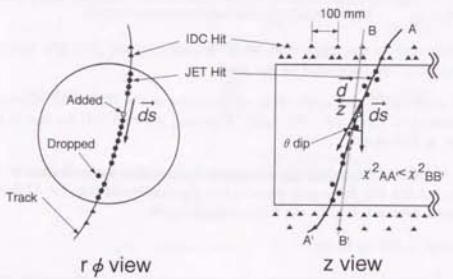

Figure 4.1: Method of the rigidity measurement.

particle were to be obtained.

Detailed calibrations were performed using the track informations retrieved as above. In order to reduce the time consumption or the process, the informations of the track and associated hits were stored into data summary files, which are flat files consisting of fixed length records. The results of the calibrations were put into the database, and pattern recognition and track fitting were performed in the ZEBRA-based system again. The final data summary files were obtained from the re-created track information banks and were used for the further analysis.

4.1.2 Track Reconstruction

The rigidity of a particle was determined by the JET and IDC drift chambers. First the transverse rigidity (R_t), the rigidity component perpendicular to the magnetic field direction, was determined by circular fitting in the $r\phi$-plane (Fig. 4.1).

The position of the hits are three-dimensionally determined by the time index and the charge of signals. Cylindrical coordinates (r, ϕ, z) were employed in the analysis, with the magnet field direction being parallel to the z-axis. The wires are parallel to the z-axis and the drift of electrons are described in the $r\phi$-plane. The hit position in the $r\phi$-plane is calculated by its drift time and the drift velocity. Although the drift length x and the drift time t are nearly proportional, some nonlinear effects exist due to distortion of the electric field. Such nonlinearity was corrected by a three-order polynomial function fitted to the deviation of the hit positions.

In order to select the hits induced by the particle in the trajectry fitting, the following algorithm was employed.

1. Select 'good' hits, which are defined as hits with enough charge and width.
2. Find trajectories by connecting the 'good' hits in JET chamber and perform circular fitting.
3. Extrapolate each of the trajectories to IDCs to find 'good' IDC hits near the trajectory, they are associated to the track.
4. Perform trajectory fitting again using all hit points in the JET and IDCs which are associated to the track. We used "Karimaki method"[51] for the fitting algorithm at this stage.
5. Scan all of 'good' hits in JET chamber and check if they are well close to the track, i.e., within the distance 5 times of the position resolution, 5σ. Only the hits checked here are used in the following processes.
6. Repeat step 4) and 5) twice.

The resultant R_t should be then corrected for non-uniformity of the magnet field, which varies up to 10%. Monte Carlo calculations with the computed magnetic field indicates that the correction factor to the rigidity of various trajectories, expressed as a function of the track position, path length, and mean strength of B field, is able to obtain the corrected rigidity which is within an accuracy of 1% from the actual one.

To obtain R from R_t into the total rigidity (R), we find the dip angle θ_{dip}, which is defined as an angle between the $r\phi$-component ($d\vec{s}$) and the z-component ($d\vec{z}$) of R, by fitting in the yz-plane (Fig. 4.1). We use a similar iterative procedure as used in the $r\phi$ fitting to eliminate irrelevant hits. The selected hits are fitted to a sine-curve. Since the IDCs provide the only z positions modulo 100mm, all possible combinations of the IDC hits are examined. The resultant θ_{dip} are obtained from the combination having minimum χ^2 value in the fitting.

Finally rigidity R are derived from R_t and θ_{dip} as,

$$R = \frac{R_t}{\cos\theta_{dip}}.$$

4.1.3 Time of Flight Measurement

Figure 4.2 illustrates the measurement scheme of time-of-flight (TOF). The TOF between top and bottom TOF hodoscopes is calculated for each track by the following procedure. We use here the suffix 'elec' for the PMT on the side of the electronics and the suffix 'tank' for the PMT on the side of the helium reservoir tank.

1. Correct a timing walk using the charge information for each PMT. We use following formulae:

$$\hat{t}_{elec} = t_{elec} - a_i/\sqrt{q_{elec}},$$

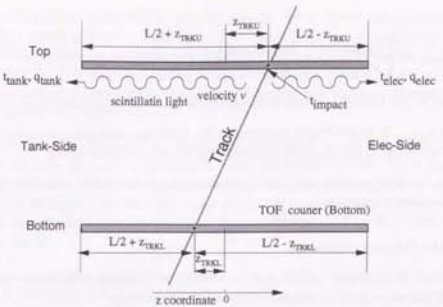

Figure 4.2: Method of the TOF measurement.

and

$$\hat{t}_{tank} = t_{tank} - a_i/\sqrt{q_{tank}},$$

where $t_{elec,tank}$ is the measured timing, $\hat{t}_{elec,tank}$ the timing after the correction, q the measured charge of the PMT, and a_i is the parameter of the ith PMT. Parameter a was determined by the beam test.

2. Derive the timing that the particle passed through the counter (t_{impact}) from the corrected timing of each PMT. Using the z-impact point (z_{trku}, z_{trkl}) of the particle which is calculated by extrapolating the combined track, t_{impact} is obtained for elec-side as,

$$t_{impact\_elec} = \hat{t}_{elec} - \frac{\frac{L}{2} - z_{trku,trkl}}{v_{eff}} - t_{offset}(z_{trku,trkl}),$$

and for tank-side as,

$$t_{impact\_tank} = \hat{t}_{tank} - \frac{\frac{L}{2} + z_{trku,trkl}}{v_{eff}} - t_{offset}(z_{trku,trkl}),$$

where v_{eff} is the effective light velocity in the counter and L is the length of the counter including light guides. The second term is the propagation time for the scintillation light to reach to each PMT. The last term $t_{offset}(z)$ is the timing offset as a function of the z position. This is introduced to correct the velocity variation depending on the z position and is determined by calibration for each counter. The averaged impact time of the counter is then obtained

as;

$$t_{impact} = \left(\frac{t_{impact\_elec}}{\sigma_{elec}(z)^2} + \frac{t_{impact\_tank}}{\sigma_{tank}(z)^2}\right) \Big/ \left(\frac{1}{\sigma_{elec}(z)^2} + \frac{1}{\sigma_{tank}(z)^2}\right),$$

where $\sigma(z)$ is the timing resolution of the each PMT as a function of z.

3. The value t_{impact} is individually calculated for both top and bottom counters, and then the TOF is obtained as the time difference between them.

The $\beta \equiv v/c$ of the particle can be determined from the TOF and the path length derived from the trajectory.

4.1.4 $\mathrm{d}E/\mathrm{d}x$ Measurement

The energy deposit of a particle, $\mathrm{d}E/\mathrm{d}x$, in a scintillator is derived from the pulse size of the PMT output, which is measured by ADC as a charge.

1. Subtract the pedestal value from the ADC count and correct it for the gain of PMT and ADC.

   $$q = (\mathrm{count} - \mathrm{pedestal})/gain$$

   The gain is determined by the calibration to normalize the energy deposit $\mathrm{d}E/\mathrm{d}x$ of energetic protons to be 1.

2. Correct the z dependence of the signal amplitude due to the attenuation or loss of scintillation light using the z-impact position of the track. The detailed study shows that the measured charge $q_{measured}$ has the z-dependence as follows:

   $$q_{measured} \simeq (a + be^{cz})dE \ ,$$

   where a,b and c are parameters that should be determined by the calibration, and $\mathrm{d}E$ is the deposited energy.

3. Average the energy deposit dE derived from the PMT signals of two ends.

4. Divide the average energy deposit by the path length in the scintillator through which the particle passed. This gives $\mathrm{d}E/\mathrm{d}x$ in the TOF counters.

4.2 Simulation

Monte Carlo (M.C.) simulations were performed in the analysis for the following purposes:

- The behavior of antiprotons in the matter is different from those of protons primarily due to annihilation process. Some portion of antiprotons will be lost through annihilation both in the atmosphere and in the instrument. We use the Monte Carlo simulation to know this effect for protons and antiprotons both in the atmosphere and in the instrument.

- In identifying antiprotons, we rely mainly upon three key properties of the event; rigidity, $\beta(\equiv v/c)$, $\mathrm{d}E/\mathrm{d}X$. Due to interactions or accidental hits, some of them might be far from the expected value. In such cases, other particle species such as electrons might mimic antiprotons. These faking processes and their probability should be investigated by the Monte Carlo simulation as well as by the real data.

- Although the solenoid coil produced an almost uniform magnetic field, we should take account of the slight non-uniformity in order to make a precise rigidity measurement. Simulating the magnetic field and tracing the path of the incident particles by small steps, we can find the difference between the true rigidity and the mesured rigidity determined by the curvature of the circular fit.

We have built a simulation model of the BESS instrument based on the GEANT/GHEISHA [50] code, assembling the detector components, support frames and others which are defined with the actual dimensions and materials. The material distribution in the instrument have been well reproduced in the model. Figure 4.3 shows the view of the simulated BESS instrument.

In the analysis using the simulated events, we extracted the physics informations from the simulated detectors. Since the signals generated by the detector components include no measurement errors and statistical fluctuations, we smeared those signals with the detector resolutions to reproduce the measured detector performance. We adjusted following parameters to reproduce the detector responses:

- Resolution of the position measurement in JET chamber and IDC.

- Efficiency of detecting hits by JET chamber.

- Number of photo-electrons in each PMT for minimum ionizing particles.

- TOF counter resolution.

Although the major features of the detector responses could be well reproduced by tuning these parameters, some differences still remained and could affected the various selections as follows. The effects of them should be considered in the use of the efficiencies.

- In finding tracks in the JET chamber, the analysis program for the Monte Carlo simulation used the information provided by the GEANT code. This means that the efficiency of track finding was 100% in the Monte Carlo simulation. On the other hand, the analysis program for the real data searched for tracks testing the possible combinations of hits in JET chamber. Some tracks may have not been recognized, causing a lower track finding efficiency.

- There were extra hits in the real JET chamber that did not associate to any track. Most likely such hits were "noise hits" induced by electro-magnetic noises or by electron emissions from the HV wires near the cylinger wall.

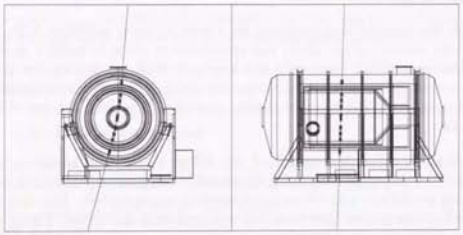

Figure 4.3: Simulated BESS detector

Some of them were "after pulses" following signal pulses, which could have been produced by the diffusion of the electrons. Others could be the hits produced by the particle whose track was not recognized. Such the extra hits from these origins cannot be produced in the Monte Carlo simulation and hence caused a difference in the selection efficiency.

- There were some electric-induced crosstalks in the IDC and ODC read-out, which affected the cell hit pattern of the IDC and ODC, causing some inefficiency of the TT Nhit selection. This effect was not taken in the simulation.

- We used the primary kinematics with only one particle in the simulation, while, in the observed data, there were multi-track events, which contained two (or more) unrelated tracks, the extrapolation of which did not intersect each other. The efficiency of the single track selection must have been affected by multi-track events.

4.3 Event Selections

The event selections were applied in order to obtain fiducial events with 'good' measurements, excluding the events with multi-track, large scatterings or accidental hits, which probably do not provide correct particle properties. The selection criteria are summarized in Table 4.2, the details of which are described in the following sections.

4.3.1 Event Reconstruction Requirement

The T0 trigger requires only the coincidence of the hits at the top and the bottom scintillation counters. The MT trigger requires the hits in IDCs and ODCs. Thus, there are events in which the incident particle did not pass through through JET chamber, or left too few hits in it to reconstruct the track with a desired accuracy. We exclude such events and use events with a long enough track in the analysis, which corresponds to a reduction of the geometrical acceptance of the instrument.

There also events which contain multi-tracks or too many hits in the detectors. A shower-like event with too many hits makes it difficult to reconstruct the tracks, and a multi-track event is not fiducial in the TOF measurement, for more than one track might have passed through the same scintillator, or the incident particle might have been scattered and changed its direction and energy.

Following cuts were applied to obtaine reconstructible events with a good single track which passed through the fiducial region of JET chamber.

1. N_{TOFU}=1 N_{TOFL} = 1

   There should be one and only one hit in the scintillation counters both at the top and at the bottom.

2. $N_{longtrack}$=1

   The number of tracks with 10 or more hits found in JET chamber should be one and only one.

3. $N_{expect} \geq 16$

   The number of hits in JET chamber expected from the trajectory N_{expect} is 16 or more. This cut defines the fiducial region of the JET chamber and eliminates the track which scratches the outermost region, where the position measurement is less accurate than the central region due to the distortion of the electric field.

4. $N_{cenhit} \geq 12$

   The number of hits in the central region of JET chamber is 12 or more. This cut also defines the fiducial region of the JET chamber and eliminates the track which scratches the outermost region, where the position measurement is less accurate than the central region due to the distortion of the electric field.

Table 4.2: Summary of the event selection cuts.

Cut No.	Description	BESS-93	BESS-94	Total
	Total Number of events	3,635,151	4,721,400	8,356,551
	(unbiased events)	(1,055,537)	(1,189,870)	(2,245,407)
Event Reconstruction Requirement				
1.....	Hits in TOF	$N_{TOFU} = N_{TOFL}$=1		
2.....	Single and long track	$N_{longtrack}$=1		
3.....	Expected hits in JET	$N_{expect} \geq 16$		
4.....	Hits in central region of JET	$N_{cenhit} \geq 12$		
5.....	$r\phi$-trajectory agreement with TOF hit counter	$R_{\rm TOFU}\Delta\phi_{\rm U} < W_{\rm TOF}/2 + 10.0$mm $R_{\rm TOFL}\Delta\phi_{\rm L} < W_{\rm TOF}/2 + 10.0$mm		
	Number of events after the cuts	2,124535	2,643,951	4,768,486
	(unbiased events)	(385,136)	(465,857)	(850,993)
Track Quality Cut				
1.....	Hits other than track hits	$N_{extrahit} \leq 30$	$N_{extrahit} \leq 40$	
2.....	Unused hits in $r\phi$-track fitting	$N_{trackhit} - N_{r\phi-fit} \leq 8$		
3.....	Hits used in $r\phi$-track fitting	$N_{r\phi-fit} \geq 10$		
4.....	Hits used in z-track fitting	$N_{z-fit} \geq 5$		
5.....	χ^2 in $r\phi$-track fitting	$\chi^2_{r\phi} < 4$		
6.....	χ^2 in z-track fitting	$\chi^2_z < 4$		
7.....	$r\phi$-trajectory agreement with IDC hits	$\min(\Delta(r\phi)_{\rm IDC1i}, \Delta(r\phi)_{\rm IDC1o}) < 2.0$mm $\min(\Delta(r\phi)_{\rm IDC2i}, \Delta(r\phi)_{\rm IDC2o}) < 2.0$mm		
8.....	z-trajectory agreement with IDC hits	$\min(\Delta z_{\rm IDC1i}/3, \Delta z_{\rm IDC1o}) < 2.0$mm $\min(\Delta z_{\rm IDC2i}/3, \Delta z_{\rm IDC2o}) < 2.0$mm		
	Number of events after the cuts	1,648,656	2,074,294	3,722,950
	(unbiased events)	(301,346)	(365,611)	(666,957)
TOF quality Cut				
1.....	z-trajectory agreement with TOF counter	$\lvert z_{\rm U}\rvert < 500$mm $\lvert z_{\rm L}\rvert < 500$mm		
2.....	Trigger time	$\lvert T_{trig}\rvert < 1.5$ns		
3.....	z-trajectory agreement with TOF hits (timing)	$(\Delta z_{\rm TOFU})^2 + (\Delta z_{\rm TOFL})^2 < (90.0\text{mm})^2$		
4.....	z-trajectory agreement with TOF hits (amplitude)	$(\Delta R_{\rm TOFU})^2 + (\Delta R_{\rm TOFL})^2 < 0.7^2$		
	Number of events after the cuts	1,325,058	1,595,543	2,920,601
	(unbiased events)	(244,640)	(283,803)	(528,443)

5. $R_{\rm TOF}\Delta\phi_{\rm TOFU} < W_{\rm TOF}/2 + 10.0$mm, $R_{\rm TOF}\Delta\phi_{\rm TOFL} < W_{\rm TOF}/2 + 10.0$mm

   where $R_{\rm TOF}$ is the distance from the center of the instrument to the center of a TOF counter, $R_{\rm TOF}\Delta\phi$ is the distance in ϕ-direction from the trajectory to the center of the nearest hit TOF counter, and $W_{\rm TOF}$ is the width of a TOF counter. In the $r\phi$-plane, the extrapolated trajectory should pass through a hit TOF counter with an accuracy of 10mm.

In total 4,768,486 events passed these cuts.

4.3.2 Track Quality Cut

Following cuts were applied to ensure a quality of the single track.

1. $N_{\rm extrahit} \leq 30$ (BESS-93), $N_{\rm extrahit} \leq 40$ (BESS-94)

   To exclude multi-track events and noisy events, the number of JET hits not concerned with the track $N_{\rm extrahit} \equiv N_{\rm totalhit} - N_{\rm trackhit}$ is to be limited.

2. $N_{\rm trackhit} - N_{r\phi\text{-fit}} \leq 8$

   As mentioned in Section 4.1.1, not all the JET hits are used in trajectory fitting. If the number of hits used in trajectory fitting $N_{r\phi--fit}$ is too small comparing to that of track-associated hits $N_{\rm trackhit}$, the quality of the track informations are possibly not good.

3. $N_{r\phi-fit} \geq 10$

   The accuracy of the track informations depends on the number of hits used in the trajectory fitting.

4. $N_{z-fit} \geq 5$

   Since the number of wires to determine z-position is less than that for $r\phi$-position determination (See Figure 2.7 in Chapter 2.), the limit on the number of utilized hits in z-trajectory fitting is lowered than in $r\phi$-fitting

5. $\chi^2_{r\phi} < 4$

6. $\chi^2_z < 4$

   The goodness of fits can be checked using the reduced chi-square parameters:

$$\chi^2_{r\phi} \equiv \frac{1}{\sqrt{N_{r\phi-fit} - 3}} \sqrt{\sum \frac{(\Delta(r\phi)_i)^2}{\sigma^2_{r\phi,i}}},$$

$$\chi^2_z \equiv \frac{1}{\sqrt{N_{z-fit} - 3}} \sqrt{\sum \frac{(\Delta(z_i))^2}{\sigma^2_{z,i}}}.$$

7. $\min(\Delta(r\phi)_{\rm IDC1i}, \Delta(r\phi)_{\rm IDC1o}) < 2.0$mm,
   $\min(\Delta(r\phi)_{\rm IDC2i}, \Delta(r\phi)_{\rm IDC2o}) < 2.0$mm

8. $\min(\Delta z_{\mathrm{IDC1i}}/3, \Delta z_{\mathrm{IDC1o}}) < 2.0\mathrm{mm}$,
   $\min(\Delta z_{\mathrm{IDC2i}}/3, \Delta z_{\mathrm{IDC2o}}) < 2.0\mathrm{mm}$

   The IDC hits are outermost hits used in trajectory fitting and provide informations independent of JET hits. Especially desired precision of the informations in z-fit are obtained only by using IDC hits. We required that at least one good hit in each IDC is close enough to the trajectory. In the data summary files are stored the informations of one hit in each layer of IDCs (IDC1i for the inner layer of the upper IDC, or IDC1; IDC2o for the outer layer of the lower IDC, or IDC2, and so on), and at least one hit of the two layers of each IDC is required to be consistent with the trajectory.

Figures 4.4 to 4.10 show the histograms of these track-quality variables together with the cut boundaries. Open histograms are for the events that pass the single-track selection, and the shadowed histograms are for the events that remain after applying the track-quality cut. In total 3,722,950 events passed these cuts.

4.3.3 TOF Quality Cut

The identification of antiprotons is performed by resolving their mass. The accuracy of the mass measurement mainly depends on the accuracy of the TOF measurement, that of rigidity measurement being much higher. The TOF measurement of an incident particle might be disrupted by a coincident hit of another cosmic ray particle or of a radiation from local radio-activated materials.

There is a time difference between the signals from the two ends of a TOF counter due to the propagation time of the scintillation light from impact points to PMTs, which depends on z-position. The size of the signals are also different due to the attenuation and the loss in reflections, which is also z-dependent. The timing difference reaches about 6ns and the amplitude ratio about 3. These features can be used to check consistency with the fitted trajectory obtained from the hits in drift chambers.

1. $|z_{\mathrm{TRKU}}| < 500$ mm , $|z_{\mathrm{TRKL}}| < 500$ mm .

   The measurements show odd behavior in small regions at the ends of the TOF couners. This is because some of the incident particles do not pass through the scintillater but through the light guide while the position calculated from the extrapolation of the fitted trajectories are within the scintillater. The conservative fiducial region of the TOF counters are defined as $|z| < 500$mm, while the scintillators occupied the region $|z| < 550$mm.

2. $|T_{trig}| < 1.5$ ns

   The T0 trigger was generated using the signals of the TOF counters. The trigger timing depended on the signals of the bottom TOF counters and is deducible from the timing and the amplitude of the signals of the bottom TOF counters. The distribution of the derived trigger timing has its peak at 0 ns and a spread due to the trigger circuit. Thus, the consistency of the siganls of the bottom TOF counters with the actual trigger timing can be examined using the derived trigger timing T_{trig}.

3. $(\Delta z_{\mathrm{TOFU}})^2 + (\Delta z_{\mathrm{TOFL}})^2 < (90\mathrm{mm})^2$.

   The z-coordinate of a hit in a TOF counter is determined using the time difference;

   $$z_{\mathrm{TOF}} = v_{\mathrm{propagation}} \cdot \Delta t/2 \ .$$

   If this value is not consistent with the fitted trajectory within the resolution of time measurement, the TOF measurement is wrong due to some accidental hit or the trajectory is wrong.

4. $(\Delta R_{TOFU})^2 + (\Delta R_{TOFL})^2 < (0.7)^2$.

   The ratio of the size, or the amplitude, of the signals from the two ends of a counter will be a monotone function of z. Since the z-dependence is due to attenuation and loss, the size of a signal read out from a end of a TOF counter will be expressed as:

   $$A \simeq \exp(a + bz) \ ,$$

   where a and b are constant peculiar to the read out channel. The ratio of the amplitude from two sides, $A_{\mathrm{L}}/A_{\mathrm{R}}$, will then be proportional to z.

   $$R \equiv \log(A_L/A_R) \simeq cz \ ,$$

   where c is constant peculiar to the counter. Actually, the values A deviate from the exponential function of z, and so do R from the linear function:

   $$R = f(z) \equiv cz + \varepsilon(z) \ .$$

   Even so, the value $\Delta R \equiv R - f(z)$ will offer a good parameter of consistency between the hit and the trajectory.

Figures 4.11 to 4.13 show the histograms of these variables together with the cut boundaries. Open histograms show the distribution of the events which passed the single track selection, and shadowed are for those after the subsequent track quality cut. Hatched histograms are for the events that passed the TOF quality cut. In total 2,920,601 events passed these cuts.

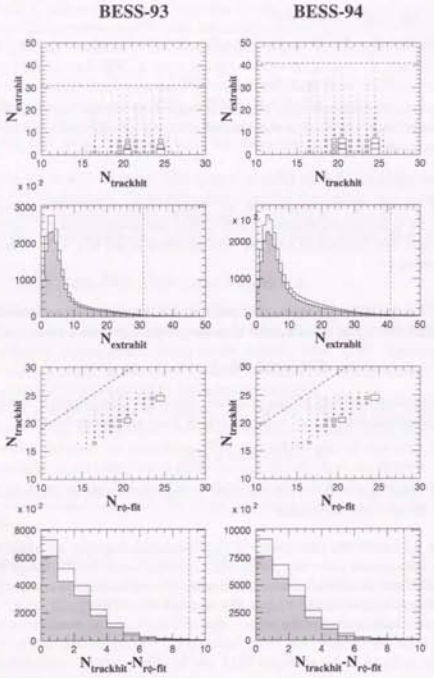

Figure 4.4: Track Quality Cut 1,2.

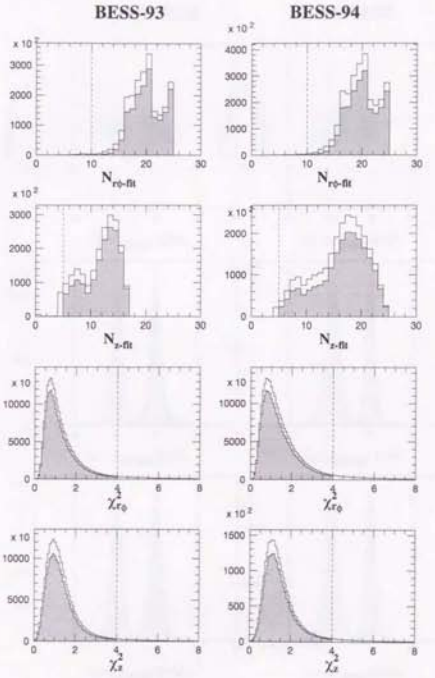

Figure 4.5: Track Quality Cut 3,4,5,6.

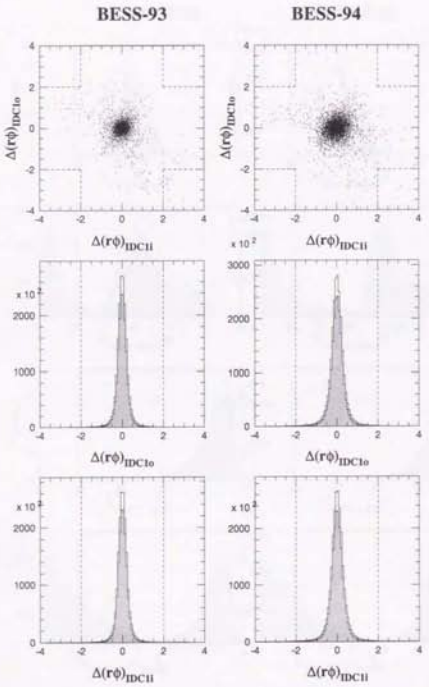

Figure 4.6: Track Quality Cut 7.

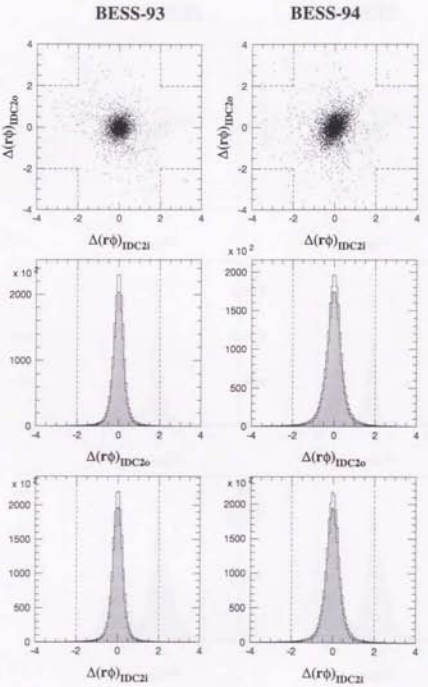

Figure 4.7: Track Quality Cut 8.

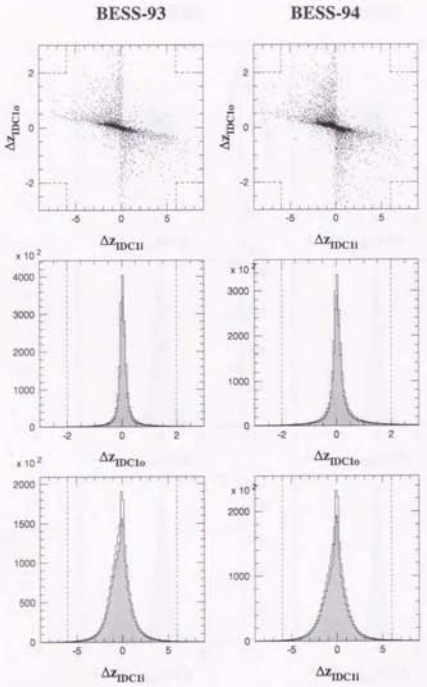

Figure 4.8: Track Quality Cut 9.

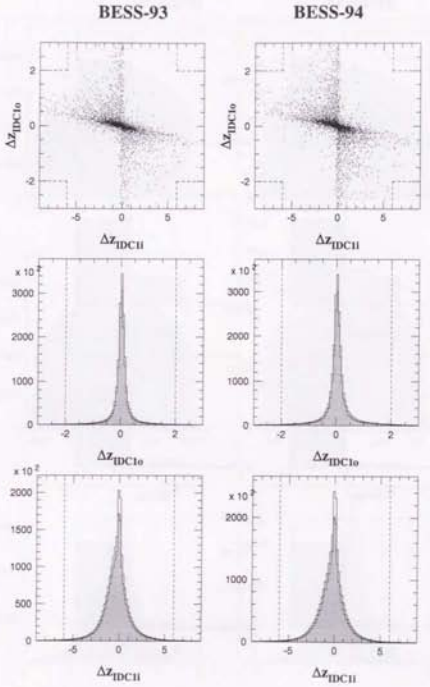

Figure 4.9: Track Quality Cut 10.

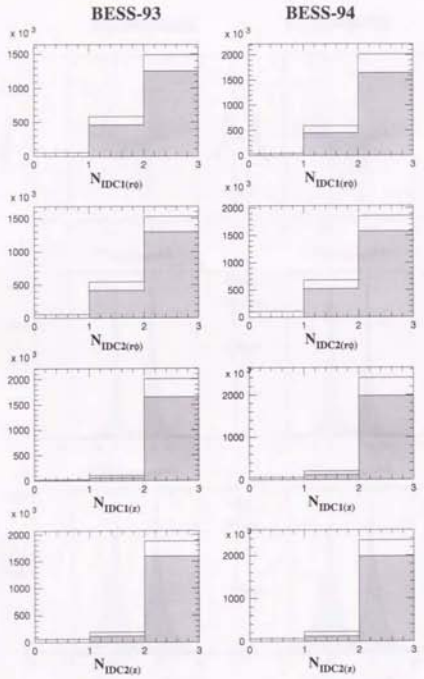

Figure 4.10: Number of hits in each IDC. The Track Quality Cut 10 requires at least one hit in each of the upper and lower IDC (IDC1 and IDC2).

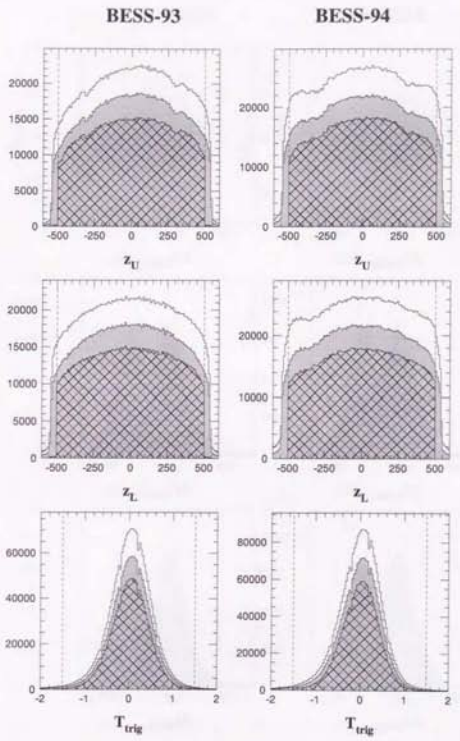

Figure 4.11: TOF Quality Cut 1,2.

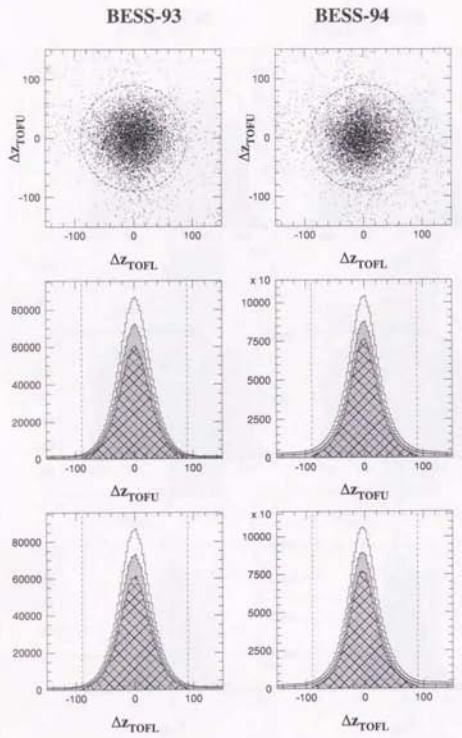

Figure 4.12: TOF Quality Cut 3.

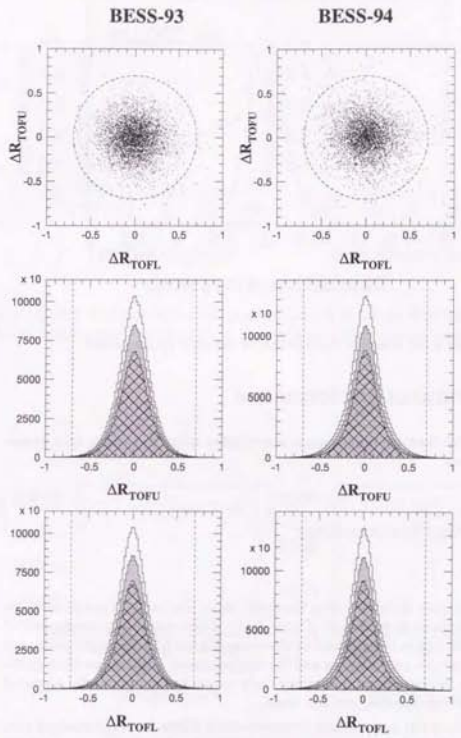

Figure 4.13: TOF Quality Cut 4.

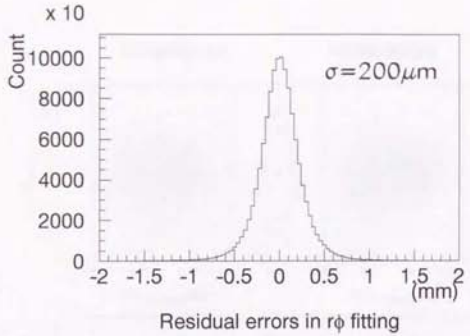

Figure 4.14: Residual distribution of the JET $r\phi$ hit points.

4.4 Instrument Performance

The quality of the detector performance was checked using the events that passed the event selection.

4.4.1 Rigidity Spectrometer

JET chamber

Based on the residuals obtained using the fitted track, the overall resolution in the $r\phi$-plane was estimated to be 200μm (Figure 4.14). These resolutions are dependent on the drift length due to the diffusion of electrons. Figure 4.15 shows the resolution as a function of (a) the drift distance and (b) the inclination angle of the track in the $r\phi$-plane relative to the vertical line, where both resolutions are gradually degraded according to the drift distance and the angle.

The resolution of the z-coordinate measurement is 2.2cm for single-charged particles (Figure 4.16(a)), being worse than the expected value of 1cm, since all the charge information below the threshold value is lost using the zero-suppress and compress scheme, and cannot be precisely corrected. On the other hand, 1.4 cm of resolution is obtained for multiple-charged (Figure 4.16(b)) because they are less affected by the threshold effect.

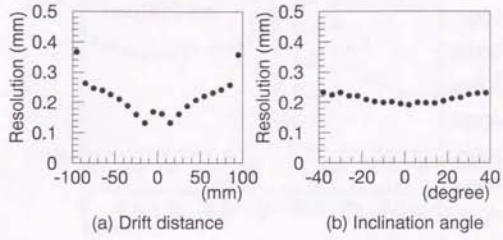

Figure 4.15: JET chamber $r\phi$ resolution as a function of (a) the drift distance, and (b) the inclination angle of the track in the $r\phi$-plane relative to the vertical line.

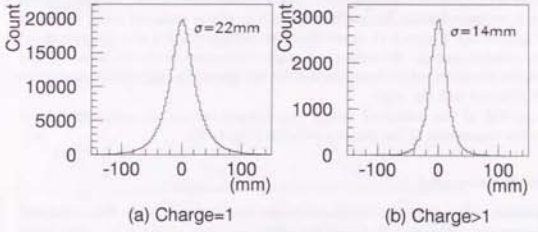

Figure 4.16: Residual distribution of the JET hit points along the z-coordinate for (a) single-charged and (b) multiple-charged particles.

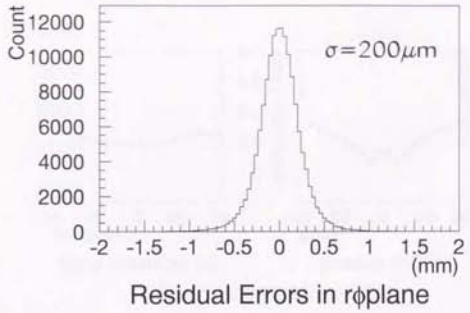

Figure 4.17: Residual distribution of the IDC $r\phi$ hits.

Inner drift chambers

The hit positions of the IDC/ODC in the $r\phi$-plane are determined using the measured drift time. Briefly, the drift velocity is calibrated using the sum of the drift times of the inner and outer layers of the IDC/ODC, after which the polynomial corrections are applied to minimize errors in the tracks. The overall resolution in the $r\phi$-plane is estimated to be 200μm based on the residuals obtained using the fitted track (Figure 4.17). Figure 4.18 shows the $r\phi$ resolution of IDCs as a function of (a) the drift distance, and (b) the inclination angle of the track in the $r\phi$-plane relative to the radial direction, where both resolutions are gradually degraded according to the drift distance and the angle.

The spread of the measured values of ε around the model calculation curve provides the estimation of the z-axis resolution (Fig 4.19).

Rigidity spectrometer

The estimated errors of the rigidity measurement were obtained in the final combined $r\phi$-fitting process. Figure 4.20 shows the estimated error of the $1/R_t$. The plane histogram is for all the events that passed the selection and the shadowed histogram is for the case that $N_{fit} > 20$. Both histograms have a clear peak around $\Delta(1/R_t) \sim 0.05$. According to the following relation,

$$\Delta\left(\frac{1}{R_t}\right) = \frac{\Delta(R_t)}{R_t^2} = \frac{\Delta(R_t)}{R_t}\frac{1}{R_t},$$

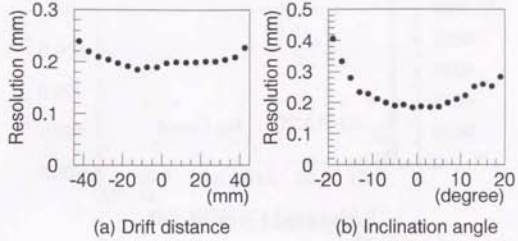

Figure 4.18: IDC $r\phi$ resolution as a function of (a) the drift distance, and (b) the inclination angle of the track in the $r\phi$-plane relative to the radial direction.

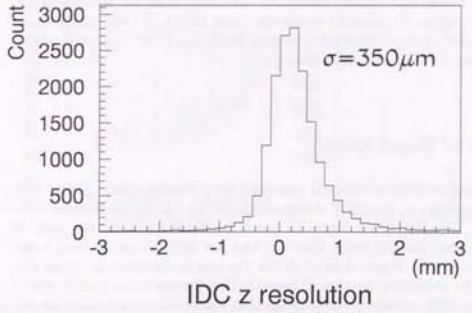

Figure 4.19: Spatial resolution of the z-coordinate measurement in the IDC.

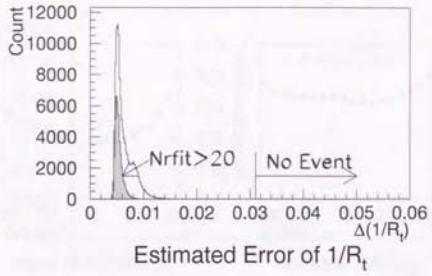

Figure 4.20: The estimated error of $1/R_t$ in the $r\phi$ fitting.

the $\Delta(1/R_t)$ is decomposed into fractional errors of rigidity ($\Delta(R_t)/R_t$) and inverse rigidity ($1/R_t$). The value of 0.005 thus indicates the particles with the transverse rigidity of up to 200 GV are at least 1σ away from the particles with the opposite charge. It is noted that no event with $\Delta(1/R_t)$ of more than 0.031 – were observed and therefore all events with rigidity below 1 GV are more than 30σ away from the negative rigidity region. Figure 4.21 shows the mean of the $\Delta(1/R_t)$ distribution as a function of the absolute rigidity for the case that $N_{rfit} > 20$. Almost constant values are obtained in the entire rigidity range.

4.4.2 Time of Flight System

The performance of the TOF system was examined using the flight data. Figure 4.22 shows the z-dependence of the PMT charge measured for the proton samples with above 3 GeV/c. The line in the figure indicates the fitted curve for the peak of the distribution using the following equation, i.e., $a + be^{cz}$, where a,b, and c are parameters to be fitted. Figure 4.22(a) shows the charge distribution versus the z-coordinates. The resolution determined from the distribution below peak is about 10% at the center of the counter, which means that about forty photo-electrons are obtained for energetic protons. At the center of the counter, the timing resolution of about 300 ps was observed. Figure 4.23(b) shows the timing resolution versus square root of the number of the photo-electrons (N_{pe}). The linear correlation between two variables is clearly observed.

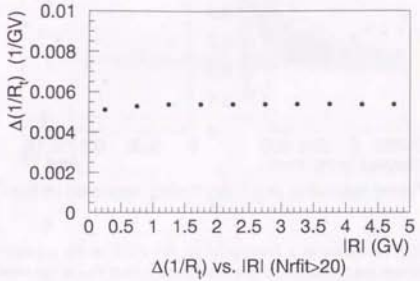

Figure 4.21: $\Delta(1/R_t)$ as a function of the absolute rigidity.

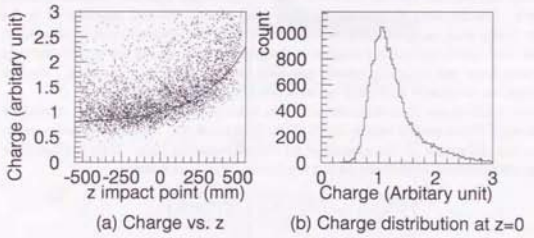

Figure 4.22: Distribution of the normalized TOF signal amplitudes measured by ADCs. (a) z-position dependence of the amplitude. (b) Distribution of the amplitudes at the center of the counter ($z = 0$).

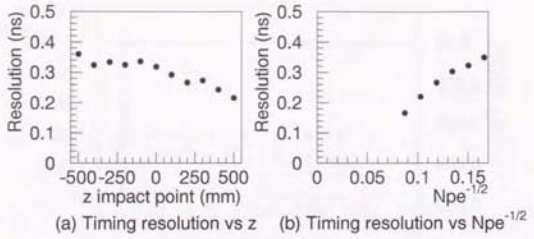

Figure 4.23: The TOF resolution as a function of (a) the PMT vs the z-position, and (b) Relation between the timing resolution and square root of N_{pe} at the center.

TOF measurement

The quality of the TOF and β measurement can be checked by utilizing the unbiased trigger sample. In Figure 4.24 the scatterplots of $1/\beta$ vs. rigidity shows the clear separation of protons, heliums, their isotopes, and pions/muons/electrons. The plots of flight data is shown in Figure 4.24(a) and the result from Monte Carlo simulation is shown in Figure 4.24(b). The Monte Carlo data are produced by isotropically injecting the protons having the same rigidity spectrum into the simulated BESS detector. Distribution of the particles including albedo are well reproduced in the Monte Carlo data except for the energetic electron, He, and isotopes of proton. It is clear that the down going particles in the positive β^{-1} region are unambiguously separated from the up-going albedo particles in the negative β^{-1} region. Various particles can be clearly identified up to a few GV of the rigidity.

Figure 4.25 shows the resolution of β^{-1} in a few rigidity intervals. The resolution was about 0.06 for proton events and 0.07 for light particles. The difference is mainly due to the difference of the quantities of the scintillation light. Two independent measurement errors contribute to the resolution of β^{-1} as follows:

$$\left(\frac{\Delta\beta^{-1}}{\beta^{-1}}\right)^2 = \left(\frac{\Delta TOF}{TOF}\right)^2 + \left(\frac{\Delta\ell_{path}}{\ell_{path}}\right)^2,$$

$$(\Delta TOF)^2 = (\Delta t)^2 + \left(\frac{\Delta z}{v_p}\right)^2,$$

where ℓ_{path} is the path-length of the trajectory between the TOF counters, t the measured time, z the lengthwise positon of the hits of TOF counters and v_p the propagation velocity of scintillation light. Figure 4.26 shows the resolution of β^{-1} as a function of β^{-1}.

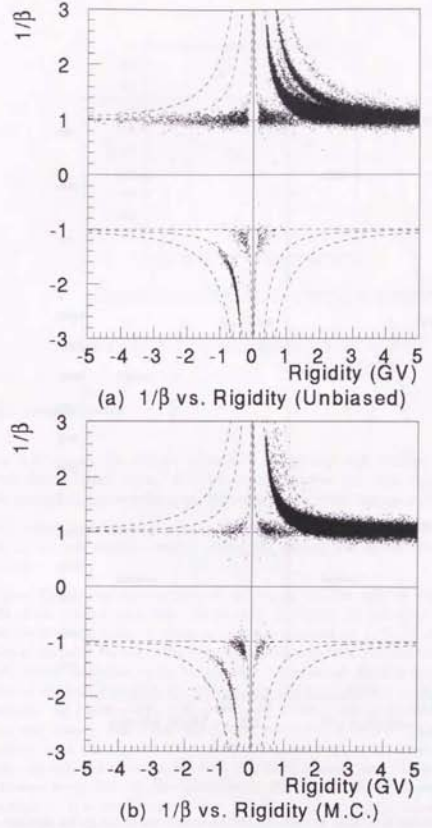

Figure 4.24: $1/\beta$ vs Rigidity of (a) unbiased data sample and (b) Monte Carlo data sample.

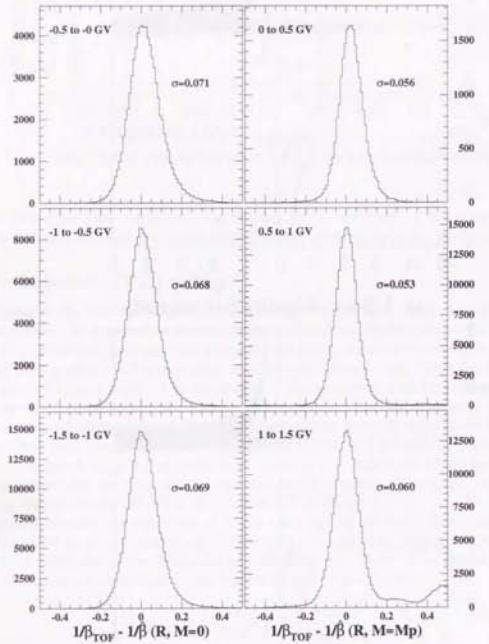

Figure 4.25: Distribution of $1/\beta$ in respect to the expected value for given rigidity R and mass M.

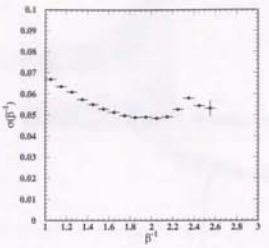

Figure 4.26: Velocity resolution as a function of β^{-1}.

$\mathrm{d}E/\mathrm{d}x$ measurement

Figure 4.27 shows the $\mathrm{d}E/\mathrm{d}x$ measured at the top and bottom TOF scintillators for the unbiased data. We can clearly observe the clear bands of protons, muons/pions/electrons deuterons, ^{3}He, and ^{4}He in both figures.

It is noted that the top and the bottom scintillators show different $\mathrm{d}E/\mathrm{d}x$ behavior in the low rigidity region, where the energy loss in the detector becomes significant.

Figure 4.28 shows various plots of $\mathrm{d}E/\mathrm{d}x$ at the low rigidity region: (a) shows $\mathrm{d}E/\mathrm{d}x$ of the bottom scintillator for protons, (b) shows $\mathrm{d}E/\mathrm{d}x$ of the top scintillator for albedo-protons, both of which are tightly selected by $1/\beta$, (c) is $\mathrm{d}E/\mathrm{d}x$ of the bottom scintillator for the proton samples produced by th Monte Carlo simulation, and (d) is the same plot as (c) except that the absolute rigidity scale is artificially multiplied by factor of 1.03 for the supposition that rigidity might be measured incorrectly. All plots exhibit similar feature; $\mathrm{d}E/\mathrm{d}x$ increases with the decrease of rigidity and steeply falls down around the rigidity of 0.45 GV. This indicates that the proton with the rigidity below 0.45 GV loose most or all kinetic energy while passing through the material between the TOF counter and the central detector. This feature is sensitive to the rigidity scale and can be utilized to check the rigidity measurement. It is clear from (d) that 3% change of the rigidity scale causes significant discrepancy between $\mathrm{d}E/\mathrm{d}x$ of the real data and that of the Monte Carlo data. Based on these results, we conclude that the absolute rigidity is correctly measured within an accuracy of 3%.

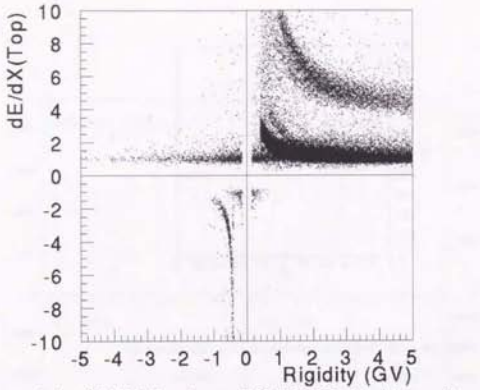

(a) dE/dX(Top) vs. RIGIDITY (Unbiased)

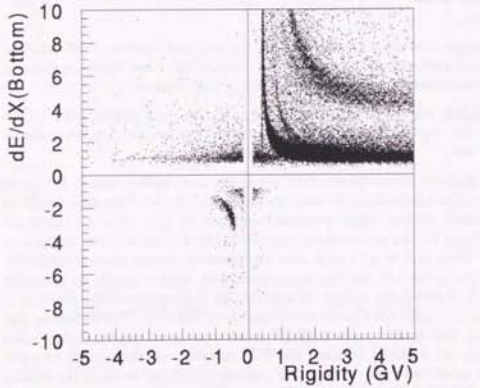

(b) dE/dX(Bottom) vs. RIGIDITY (Unbiased)

Figure 4.27: dE/dx distribution of the Unbiased samples.

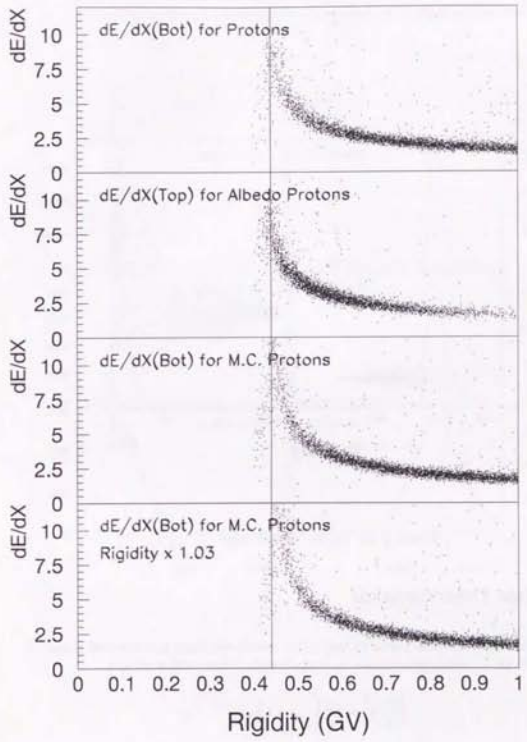

Figure 4.28: dE/dx of the stopped protons.

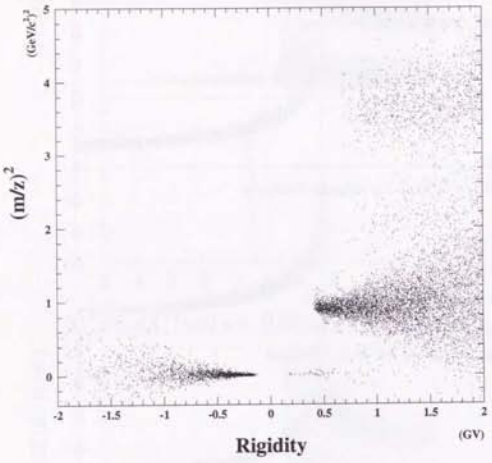

Figure 4.29: $(m/z)^2$ distribution.

4.4.3 Mass Determination

The mass of the incident particles are to be calculated from the velocity β and the rigidity R as:

$$\left(\frac{m}{z}\right)^2 = R^2\left(\frac{1}{\beta^2} - 1\right).$$

Figure 4.29 shows the distribution of the measured mass and rigidity, and the mass distributions in certain rigidity regions.

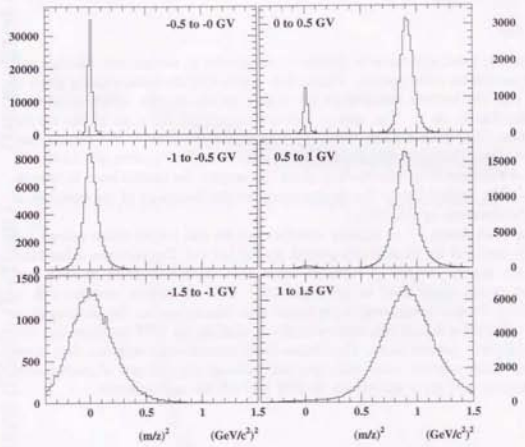

Figure 4.30: $(m/z)^2$ distribution at various rigidities.

4.5 Selection of Proton/Antiprotons Events

In Section 4.3 are described the selection criteria of fiducial events. Here we discuss the criteria to select proton/antiproton events. The particle identification is made using the mass determined by the rigidity, the velocity and the energy deposit.

Downward movement

Since we are going to derive the flux of protons and antiprotons at the top of the atmosphere, the further analysis are limited to the events with downward moving particles.

dE/dx cut

We utilize the band structures in dE/dx – rigidity plot to extract only protons and antiprotons among other species. Figure 4.31 shows dE/dx-versus-rigidity plots of the top and the bottom scintillators for a pure proton sample, which is selected by cutting tightly on β. The central line corresponds to the peak of the dE/dx distribution. The dashed lines define the "proton dE/dx-band". We require that antiprotons as well as protons must have the dE/dx in this "proton dE/dx-band".

Figure 4.32 shows the distribution of dE/dx around the proton peak at various rigidities. The dashed line in the figures represent the boundary of the selection of protons/antiprotons by dE/dx.

Figure 4.33 shows β^{-} vs rigidity distributions for the events which passed the event selection and for those which passed the dE/dx cut The particles other than protons are largely reduced at rigidities below 1GV. It is also worth to note that off-timing events distributed in the region $\beta^{-1} < 1$ are clearly sweeped out in Fig. 4.33(b). They are supposed to be events with interactions in the instrument, a number of particles depositting large energies in total in the TOF counters and disrupting the time measurement. The Monte Carlo simulations confirmed that there are events which pass the event selection, event though they consist of multi tracks or interactions, and show odd values in TOF and dE/dx measurement.

β cut

According to the resolution of β^{-1} shown in Figure 4.26, the β^{-1} of relativistic particles are distributed around $\beta^{-1} = 1$ with a variance $\sigma^2 \sim 0.0046$. The number of events with rigidities $-2 < R < 0$ is about 1.14×10^4 after the dE/dx cut, and supposing the distribution to be normal, or Gaussian, the expected number of events to be found with $\beta^{-1} > \beta_{cut}^{-1}$ is;

$$\begin{cases} 1 & (\beta_{cut}^{-1} = 1.25; 3.7\sigma) \\ 0.1 & (\beta_{cut}^{-1} = 1.29; 4.3\sigma) \\ 0.01 & (\beta_{cut}^{-1} = 1.33; 4.8\sigma) \end{cases}$$

There could be a fraction beyond the normal distribution caused by some interaction, and the validity of the estimation are to be examined using the number of events with

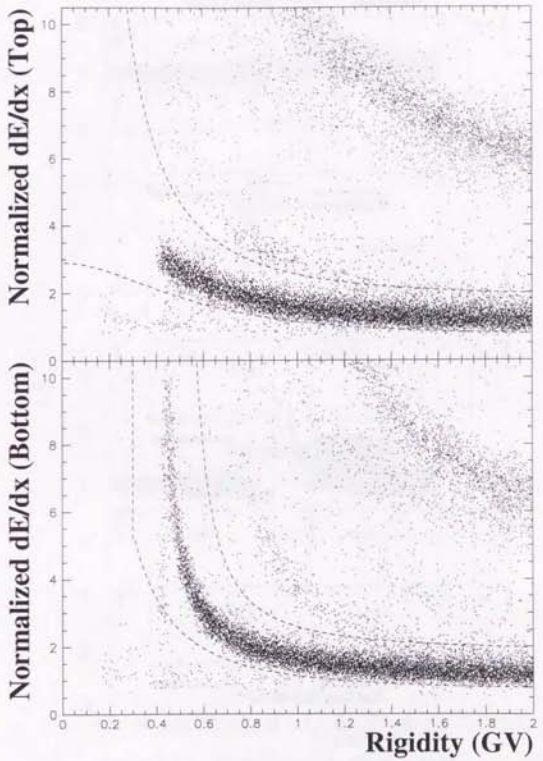

Figure 4.31: Proton dE/dx cut

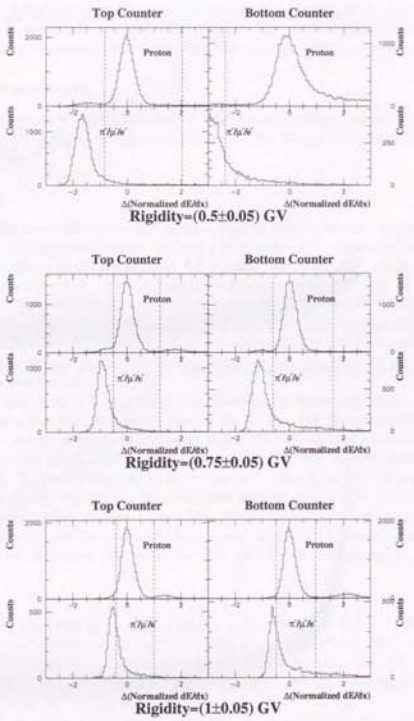

Figure 4.32: $\mathrm{d}E/\mathrm{d}x$ distribution relative to the proton peak. dashed lines represent the boundary of the $\mathrm{d}E/\mathrm{d}x$ cut at the rigidity.

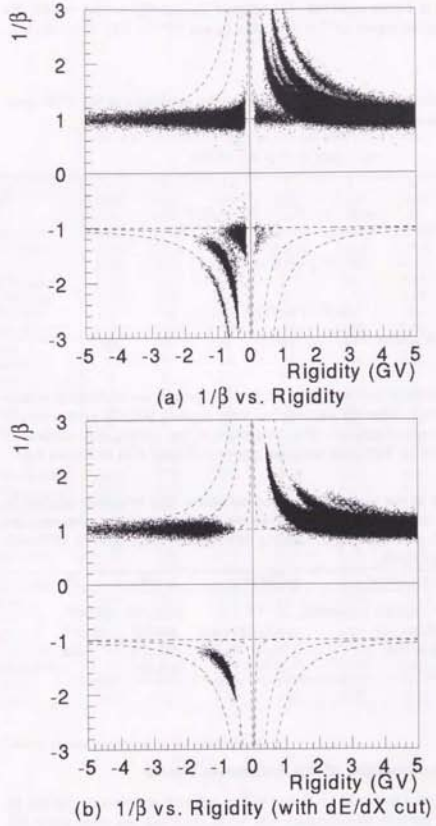

Figure 4.33: β^{-} vs rigidity for all event samples (a) before $\mathrm{d}E/\mathrm{d}x$ cut and (b) after $\mathrm{d}E/\mathrm{d}x$ cut.

$\beta^{-1} < 1 - (\beta_{cut}^{-1} - 1)$ or higher rigidities. We adopted the cut $\beta_{cut}^{-1} = 4.5\sigma = 1.31$. No events were found in the region $(\beta^{-1} < 0.69, R < 0)$ nor $(\beta^{-1} > 1.31, R < -2GV)$.

Mass cut

The resolution of calculated mass is dominated by the resolution of the TOF measurement. Thus, a mass-identifying cut

$$m_p - \Delta m < m < m_p + \Delta m$$

is equivalent to

$$\beta_p^{-1} - \Delta(\beta^{-1}) < \beta^{-1} < \beta_p^{-1} + \Delta(\beta^{-1}) \,,$$

where

$$\beta_p^{-1} = \sqrt{1 + (m_p/R)^2} \,.$$

We adopted

$$\Delta(\beta^{-1}) = 2\sigma(\beta^{-1})$$

with $\sigma(\beta^{-1})$ shown in Figure 4.26.

In Table 4.3 are summarized the cuts used to select proton and antiproton events after the event selection. After all the cuts had been applied, 202,427 proton events and 8 antiproton events remained. The properties of the proton and antiproton events are summarized in Table 4.4, and also shown in Figure 4.34 to Figure 4.43.

Table 4.3: Summary of the proton/antiproton selection. The cuts were applied in the order as shown here. The numbers of events which passed the cuts are also shown as N_+ and N. correspondig to those in the rigidity range 0.5 – 1.5GV and −1.5 – −0.5GV, respectively.

Cut No.	Description	Value	N_+	N.
1	Downward movement	$\beta > 0$	467,172	103,001
2	dE/dx cut	dE/dx–band	349,747	11,394
3	Mass cut	$m_p \pm 2\sigma_p(E)$	325,238	462
4	β cut	$\beta^{-1} > 1.31$	202,427	8

Supplementary Confirmation of the Antiproton Events

We selected the antiproton events by their rigidity, velocity and energy deposit at TOF counters. The particle identification was made resolving the mass using the rigidity and TOF after the dE/dx cut. There are some other informations obtained from the instrument:

Table 4.4: The properties of the antiproton events.

Property	1	2	3	4	5	6	7	8
Flight	1993	1993	1993	1993	1993	1993	1994	1994
Run	14	15	18	19	22	24	6	16
Event No.	535375	711708	1695042	2197801	3164639	3597064	456938	949486
Rigidity(GV)	-1.083	-0.914	-0.794	-0.994	-0.939	-0.933	-1.069	-0.620
β	0.743	0.696	0.651	0.756	0.692	0.704	0.737	0.564
$(dE/dx)_{\rm TOFU}$	1.29	1.35	1.70	1.47	1.61	1.33	1.48	1.74
$(dE/dx)_{\rm TOFL}$	1.51	1.89	1.90	1.17	1.37	1.73	1.88	3.04
$E^{\rm TOA}$(MeV)†	531	413	338	467	432	430	522	248
(Mass(GeV/c^2))^2	0.949	0.889	0.860	0.741	0.959	0.887	1.014	0.845
N_{expect}	23	20	20	24	17	20	20	20
$N_{trackhit}$	24	21	19	24	18	20	22	21
N_{conhit}	24	21	19	24	18	20	22	21
$N_{extrahit}$	5	4	5	20	2	10	11	7
$N_{r\phi-fit}$	24	19	19	24	18	19	21	20
N_{z-fit}	24	19	19	24	18	19	21	20
$\chi^2_{r\phi}$	0.48	0.72	0.60	0.93	1.14	2.10	1.09	1.39
χ^2_z	2.16	1.14	1.20	0.76	0.45	0.76	1.13	1.31
$\Delta(r\phi)_{\rm IDC1o}$(mm)	0.09	0.23	-0.07	-0.15	-0.32	-0.20	-0.47	0.46
$\Delta(r\phi)_{\rm IDC1i}$(mm)	-0.07	-0.10	—	0.30	-0.31	-0.20	-0.29	—
$\Delta(r\phi)_{\rm IDC2o}$(mm)	0.02	0.39	0.16	-0.40	0.15	0.11	0.03	-0.14
$\Delta(r\phi)_{\rm IDC2i}$(mm)	-0.07	0.03	0.26	0.03	-0.41	0.19	0.19	0.10
$\Delta z_{\rm IDC1o}$(mm)	0.31	-0.08	0.04	0.02	-0.13	—	0.21	0.05
$\Delta z_{\rm IDC1i}$(mm)	-0.77	1.24	-0.32	0.10	1.13	-0.08	-0.05	0.06
$\Delta z_{\rm IDC2o}$(mm)	0.16	-0.02	0.10	-0.10	-0.02	0.04	0.04	0.05
$\Delta z_{\rm IDC2i}$(mm)	-1.26	0.26	-1.14	0.42	0.43	0.03	-0.11	-1.36
$z_{\rm U}$(mm)	54.6	-191.8	-22.5	418.4	-423.9	-102.9	-35.7	449.1
$z_{\rm L}$(mm)	-290.0	-117.3	173.3	95.0	-201.8	411.1	280.0	-160.6
T_{trig}(ns)	0.06	0.07	0.15	0.26	0.32	0.54	-0.16	-0.17
$\Delta z_{\rm TOFU}$(mm)	14.8	5.2	1.80	30.5	-17.58	27.16	29.42	8.97
$\Delta z_{\rm TOFL}$(mm)	13.1	-19.4	2.01	20.3	-33.45	43.61	-10.32	4.18
$\Delta A_{\rm TOFU}$	0.22	-0.04	-0.12	-0.003	0.04	0.24	0.03	0.05
$\Delta A_{\rm TOFL}$	0.03	-0.11	-0.00	0.07	0.13	-0.17	0.03	-0.12

† The kinetic energy at the top of the atmosphere.

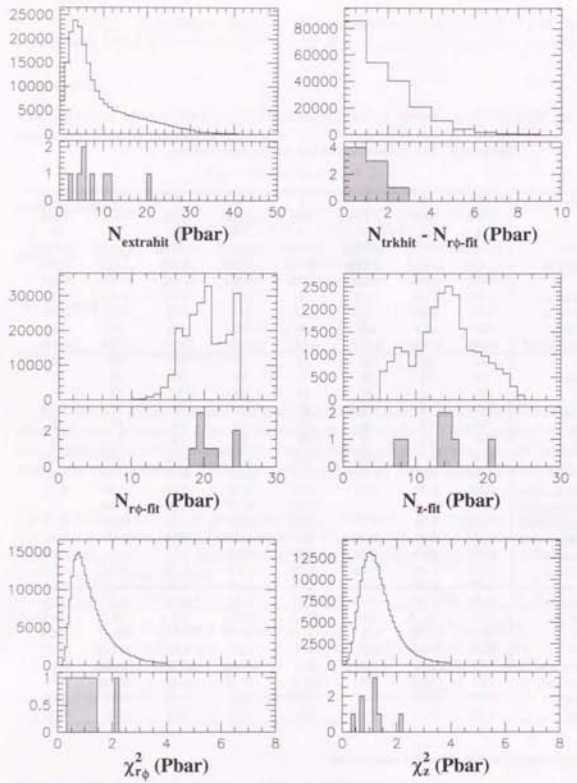

Figure 4.34: The properties of the proton/antiproton events (1). The open histgrams show the distribution for the proton events and the shadowed ones for the antiproton events.

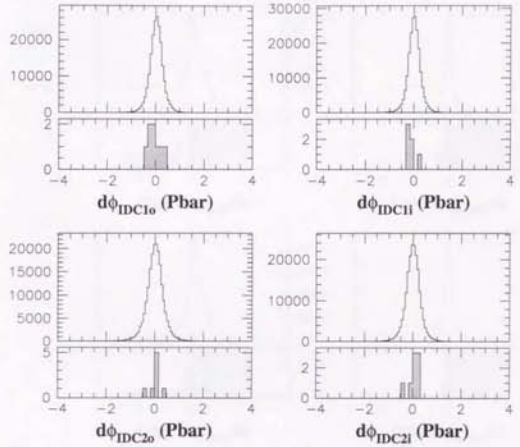

Figure 4.35: The properties of the proton/antiproton events (2). The open histgrams show the distribution for the proton events and the shadowed ones for the antiproton events.

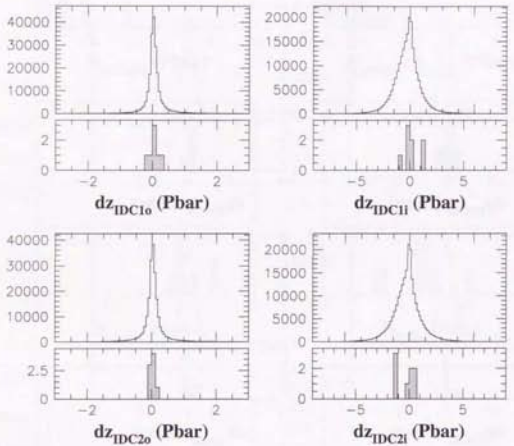

Figure 4.36: The properties of the proton/antiproton events (3). The open histgrams show the distribution for the proton events and the shadowed ones for the antiproton events.

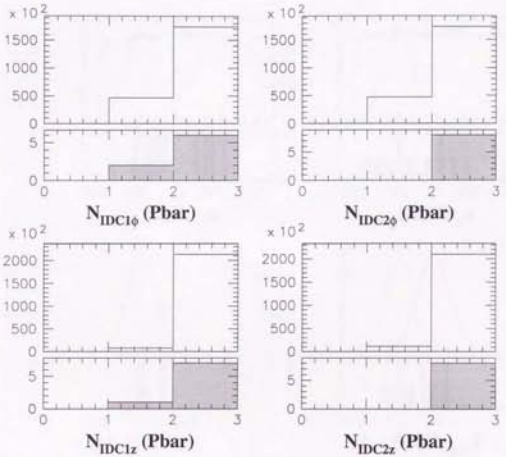

Figure 4.37: The properties of the proton/antiproton events (4). The open histgrams show the distribution for the proton events and the shadowed ones for the antiproton events.

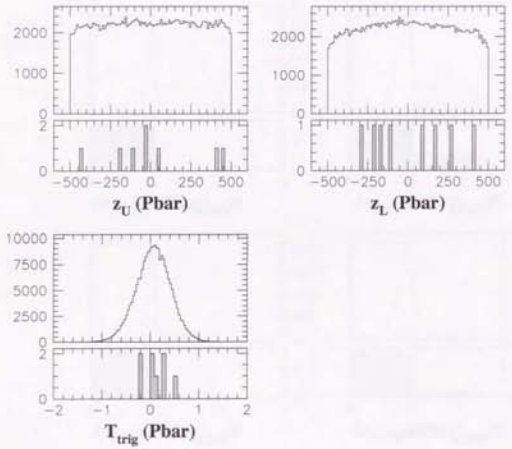

Figure 4.38: The properties of the proton/antiproton events (5). The open histgrams show the distribution for the proton events and the shadowed ones for the antiproton events.

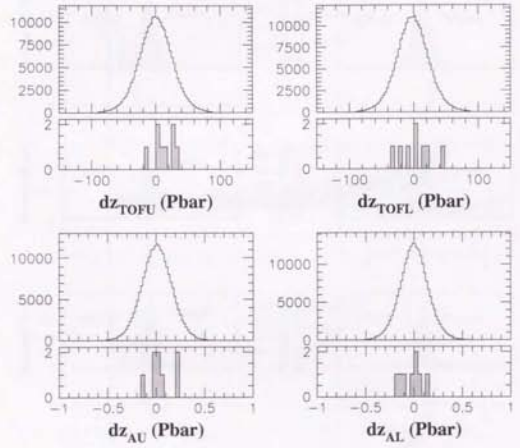

Figure 4.39: The properties of the proton/antiproton events (6). The open histgrams show the distribution for the proton events and the shadowed ones for the antiproton events.

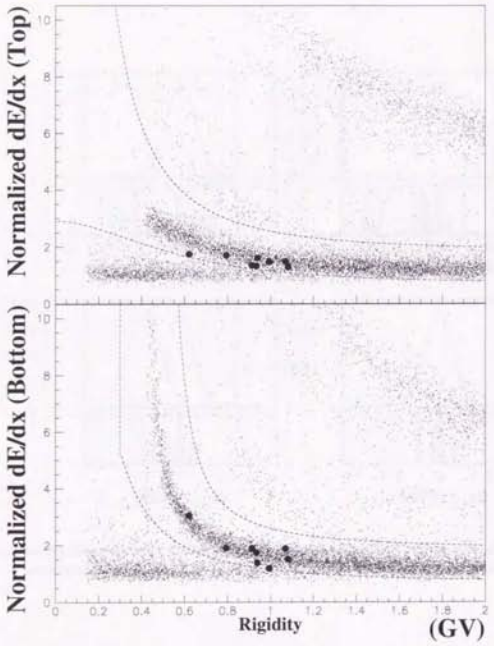

Figure 4.40: Distribution of $\mathrm{d}E/\mathrm{d}x$ vs Rigidity of the antiproton events (filled circles). The dots are of the events which passed the event selection.

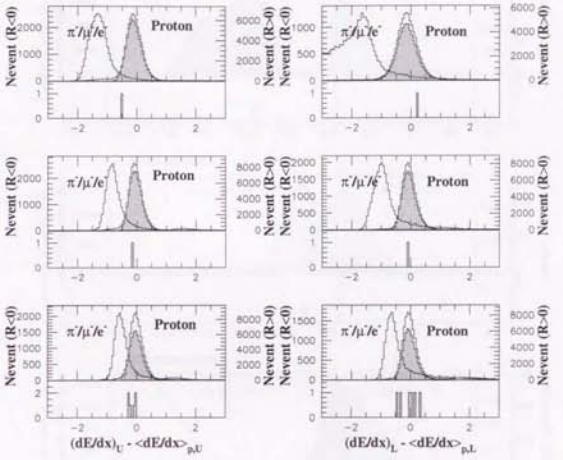

Figure 4.41: The $\mathrm{d}E/\mathrm{d}x$ distribution of the proton/antiproton events. The shadowed histgrams show the $\mathrm{d}E/\mathrm{d}x$ of the of the proton/antiproton events. The distribution of those of events which passed the event selection are shown as the open histgrams for a comparison.

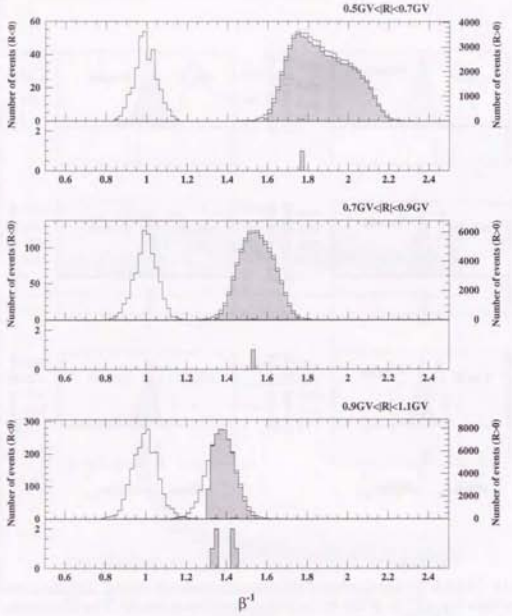

Figure 4.42: The β^{-1} distribution of the proton/antiproton events. The shadowed histgrams show the β of the of the proton/antiproton events. The β distribution of the events which passed the event selection and the $\mathrm{d}E/\mathrm{d}x$ cut are shown as the open histgrams for a comparison.

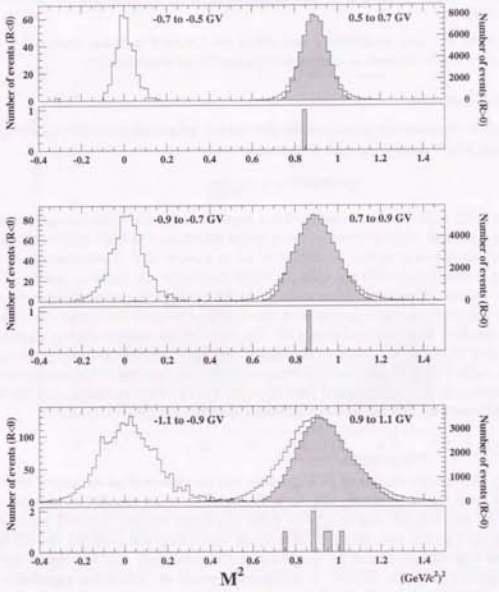

Figure 4.43: The mass of the proton/antiproton events. The shadowed histgrams show the distribution of the properties of the antiproton/proton events. The open histgrams show the distribution of those of events after the dE/dx cut for a comparison.

- Čerenkov light signals — the velocity dependence of the signal size of the Čerenkov counters can be utilized to separate antiproton events from negatively charged light particles.
- dE/dx in JET chamber — the energy deposit in the chamber gas offers a good means of particle identification, for a number of hits can be processed statistically providing a better resolution than in dE/dx measurement in TOF counters.

Although they are very preliminary and could not be used as main means of the selection, they could be used as means of supplementary confirmation.

Čerenkov Counters

The Čerenkov counters can provide a supplementary information for the velecity of the particles which passed through the counters as:

$$pulsesize \propto 1 - \frac{1}{n^2\beta^2},$$

where n = 1.522 is the refractive index of the counter. Since the Čerenkov lights are emitted at a limited angle relative to the incident direction, the light collection efficiency depends not only on the z-position which is a parameter of attenuation, but also on the incident angle and the velocity which determine the emission angle relative to the counter dimension. After calibrating these effects the velocity-dependent signal size was derived, and together with the rigidity the mass-dependent distribution were obtained as shown in Figure 4.44. The distribution independent of rigidity in the left half of the figure is that of relativistic particles and the rigidity-dependent one in the right half is of protons. Unfortunately, the trajectories of the antiproton events collected in BESS-94 did not pass through the Čerenkov counters, and there were no informations utilized in the confirmation of the antiproton selection.

JET dE/dx

The energy deposits in the gas of JET chamber can be measured as the size of readout signals from the sense wires. Taking a trancated mean of the dE/dx measured at individual sense wires, nearly typical value of dE/dx can be obtained without affected by the Landau tail. However, due to the use of slow-gas mixture, the space charge near the wire produced by the avalanche is significant and the signal size is not proportional to the dE/dx. A preliminary result of calibrating signal-size-to-dE/dx relation made on some of the data, including two antiproton events, has shown the dE/dx of the antiproton events are consistent with the dE/dx distribution of proton events (Figure 4.45).

4.6 Background Inspection

To ensure that the above candidates are real antiprotons, we investigated background processes which could produce fake antiproton events. The antiproton events are

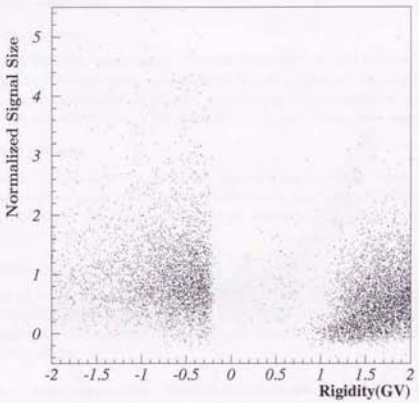

Figure 4.44: Distribution of Čerenkov signal size vs rigidity. There were no antiproton events which passed through the Čerenkov counters.

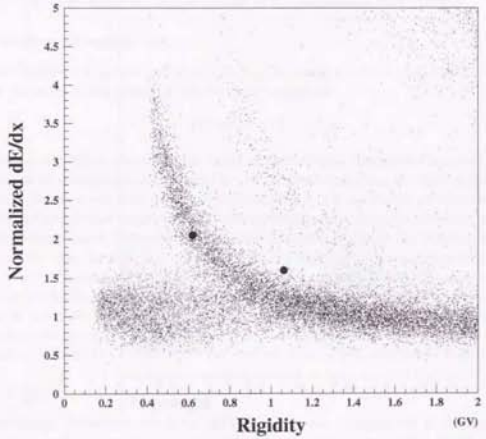

Figure 4.45: Distribution of JET dE/dx vs rigidity. The antiproton events are marked with filled circles. Since the calibration is on the way, this is the preliminary plot and only two events are displayed. The runs which includes the other antiproton events are not calibrated yet.

mass-resolved, the mass determined by velocity and rigidity. Background events could be produced by the errors in TOF or rigidity measurement. We categorized the background processes into following cases:

1. Negative charged muons/pions/electrons

   Since the TOF measuremnt is less confident than that of rigidity, negative charged particles are the most likely to fake antiproton events, their curvature of the trajectory being of the same signature as that of antiprotons. A few nanoseconds of the error in TOF could lead to a wrong recognition of the event as of an antiproton.

2. Albedo protons

   Albedo particles which came into the instrument at the bottom, went up and exited at the top, have opposite-curvature to that of down-going particles. The main component of albedo particles, protons, could compose a kind of background when their TOF were wrong by more than ten nanosecond.

3. Proton spillover

   Some of the positive charged particles with high rigidity could be recognized as negative charged particles due to the worse resolution in the higher rigidity measurements. This kind of background would be dominated by protons which dominate in the cosmic rays.

4. Protons scattered in the instrument

   Some of the incident particles could have been scattered in the instrument, their rigidity being measured incorrectly to the extent that the curvature were recognized as of negative. The dominant component of this kind of background is also protons.

For above cases, we examined likelihood of background production using the real flight data and the Monte Carlo data.

Light negative particles

Although the antiproton events are selected to locate more than 4σ away from the center of the distribution of the relativistic particles, using the β^{-1} resolution 0.072 at $\beta = 1$, where $3.2 \times 10^{-5}\%$ of the relativistic particles could spill over, the probability of the spill is based on the Gaussian distribution and the measured velocity of electrons/muons/pions would distribute beyound it due to some extra hits produced by interactions in flight or another accidentally incident particle. We performed Monte Carlo simulations to estimate the probability beyond the Gaussian distribution, for electrons, muons and pions. Since the fraction of the electron/muon/pion components in the observed negative charged particles are not known, we examined every species with more than five times as many simulation events as observed negative charged events. Some of the results are shown in Fig. 4.45 to Fig. 4.47. No events

are observed inside the 2σ region of the proton β-distribution at the β^{-1} above 1.31 after the dE/dX cut, although some pions came into the 2 σ range before the cut. We looked into these events closely and have found that they all have interaction of the incident particle in the instrument. Figure 4.48 shows one of the events, in which the incident pion interacted in the magnet and a slow secondary proton from the vertex reached the TOF counter which is on the extrapolation of the track and caused a wrong velocity mesurment. However, the dE/dX cut rejected completely this kind of events. In addition, since most of pions which have been produced in the atmosphere above the instrument decays before reaching the instrument, the number of pions is overestimated in the simulation. We conclude that a probability for pions as well as electrons/muons to fake antiproton events cannot be significant.

Albedo particles

The chance of an albedo particle faking any of the candidates is also extremely small, since the measured β^{-1} of the candidates are all more than 45σ away from those for up-going particles. Figure 4.49 shows β^{-1} distribution which passed the event selection and the proton dE/dX cut in the rigidity range between -0.5GV and -2.0GV. There are no tail events which spill beyond $\beta^{-1} = 0$ both for down-going and up-going particles.

Proton spill-over

The spill-over is due to the low accuracy of the measurement of high rigidities. The relative accuracy in the R_t^{-1} determination was obtained in the process of the track fitting and the mean value of $\Delta(1/R_t)$ is about 0.005GV^{-1} over all rigidities as shown in Figure 4.21. Figure 4.50 shows the Deflection ($\equiv$ Rigidity^{-1}) distribution of all the events that passed the event selection. The spill from the positive deflections to negative deflections appears to be less than 10 events even at -0.1GV^{-1} and rapidly decreases below -0.1GV^{-1}. These facts suggest that the expected number of events of protons which spill down to -1.0GV^{-1} is negligibly small.

Events with scattered particle

The above consideration includes only the resolution of rigidity measurement. As in the TOF measurement, interactions could provide another background source beyond the fluctuations due to resolution. A track of a particle which was scattered in the midst of JET chamber shows a wrong deflection and could fake a wrong rigidity. However, absolute curvatures are large enough at rigidities $|R| \leq 1$GV and such events that fake a wrong curvature with scatters would be identified by the large χ^2 in track fitting. Figure 4.51 shows an event in which the incident particle is negatively deflected and the fitted track yields negative curvature, however, the χ^2 of fit is too large to be selected with track quality cuts. A close investigation shows the incident particle has positive curvature with a scatter point in the midst of JET chamber. Thus, it is very unlikely to fake a low energy antiprotons by a scattered particle.

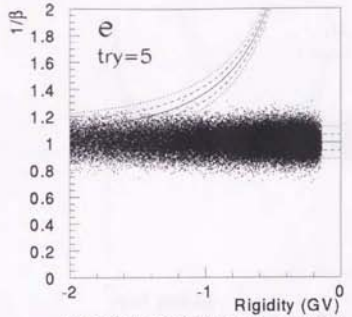

(a) 1/β vs. Rigidity (M.C. electron)

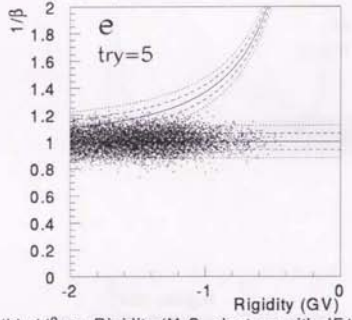

(b) 1/β vs. Rigidity (M.C. electron with dE/dX cut)

Figure 4.45: β^{-1}-rigidity distribution of electrons from a Monte Carlo simulation. (a) before and (b) after dE/dX cut. Solid, dashed and dotted curves are the expected value, 1σ and 2σ of β^{-1} for antiprotons (upper) and electrons (lower).

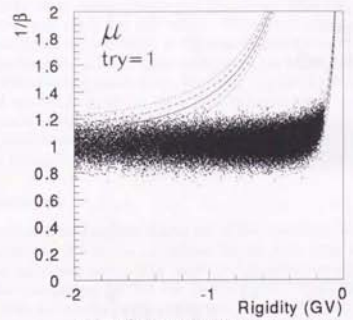

(a) 1/β vs. Rigidity (M.C. muon)

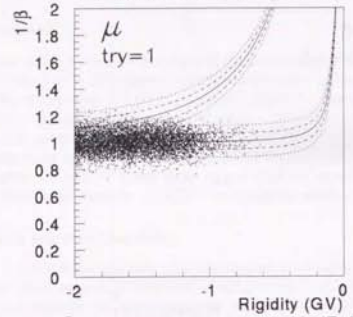

(b) 1/β vs. Rigidity (M.C. muon with dE/dX cut)

Figure 4.46: β^{-1}-rigidity distribution of muons from a Monte Carlo simulation. (a) before and (b) after $\mathrm{d}E/\mathrm{d}X$ cut. Solid, dashed and dotted curves are the expected value, 1σ and 2σ of β^{-1} for antiprotons (upper) and muons (lower).

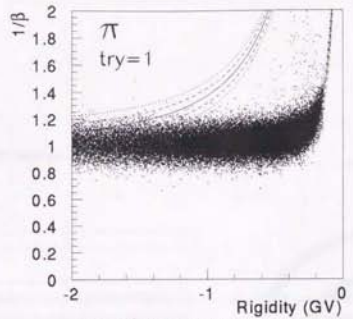

(a) 1/β vs. Rigidity (M.C. pion)

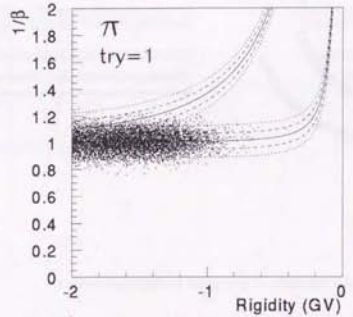

(b) 1/β vs. Rigidity (M.C. pion with dE/dX cut)

Figure 4.47: β^{-1}-rigidity distribution of pions from a Monte Carlo simulation. (a) before and (b) after $\mathrm{d}E/\mathrm{d}X$ cut. Solid, dashed and dotted curves are the expected value, 1σ and 2σ of β^{-1} for antiprotons (upper) and pions (lower).

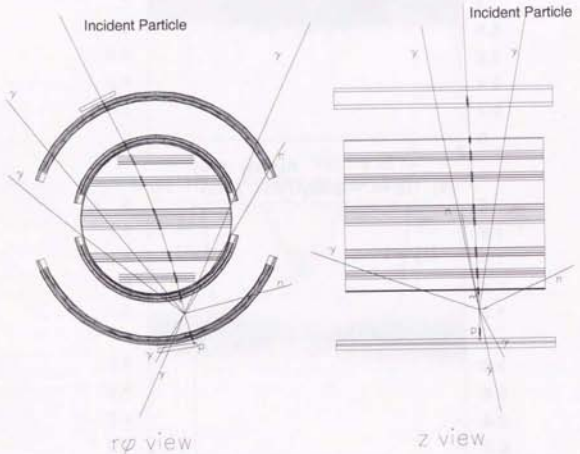

Figure 4.48: An example of potential background events.

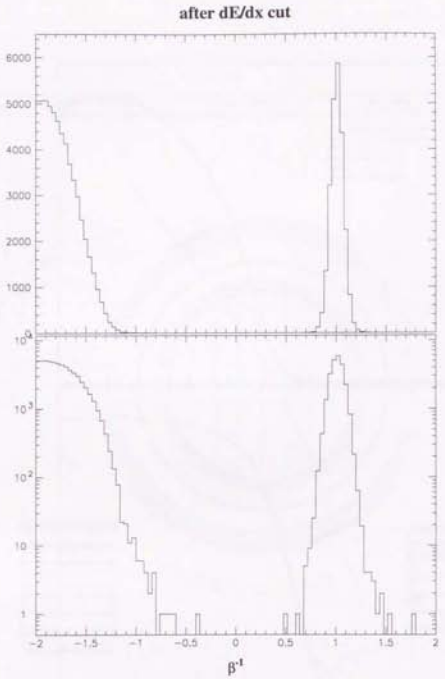

Figure 4.49: β^{-1} distribution of negative-charged particles at rigidities -2GV to -0.5GV, after $\mathrm{d}E/\mathrm{d}X$ cut. The two graphs are for the same histogram with linear and logarithmic scales.

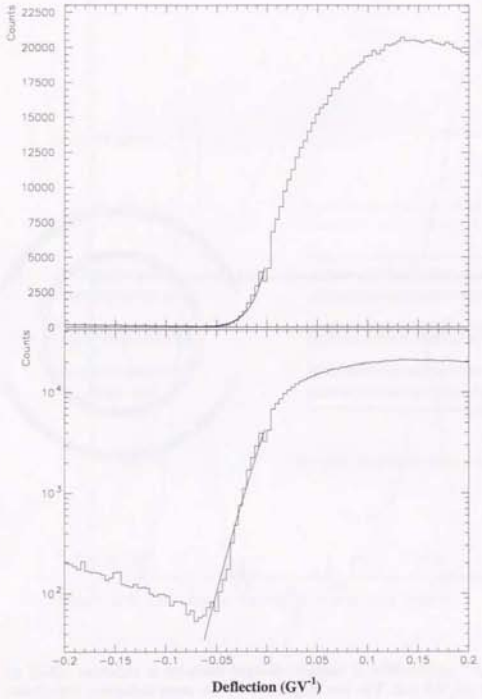

Figure 4.50: Relative accuracy of the rigidity measurement. The two graphs are for the same histogram with linear and logarithmic scales.

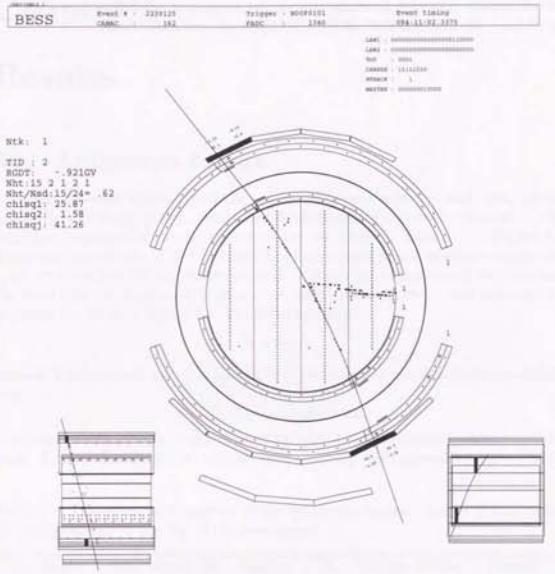

Figure 4.51: A background event with scattered particle. Although the curvature of the fitted trajectory is negative, the χ^2 of the fit is too large and the track obviously shows a kink in the midst and a positive curvature before and after the kink.

An important remark is to be added to all above background estimations. Since the antiproton events are mass-resolved, the region in which antiprotons can be faked is very small comparing to the error distribution of TOF or rigidity measurement. Thus, the probability to fake an antiproton event is much smaller than, for instance, the probability to fake an opposite signed curvature or to obtain a large error in TOF measurement. Detailed investigations on the antiproton candidates provided no sign of fake. We conclude that all the candidates are real antiprotons.

Chapter 5

Results

5.1 Antiproton Events

After the event selection and the proton/antiproton selection had been applied to the data, 202,427 proton events and 8 antiproton events were obtained. The principal properties of the antiproton events are listed in Table 5.1. Figure 5.1 shows the distribution of β^{-1} and rigidity of the events which remainiend after the event selection and the dE/dx cut together with the cut boundaries of the beta and the mass cuts. In Figure 5.2 is shown the distribution of $(\beta\gamma)^{-1}$ and deflection of the same events as in Figure 5.1. From the equation

$$P = m\gamma\beta\,,$$

where P is momentum and m is mass, $(\beta\gamma)^{-1}$ is obviously propotional to the deflection

$$(\gamma\beta)^{-1} = (m/ze)\cdot \text{deflection}\,,$$

There can be seen straight bands of particles with the inclinations depending on their mass. In both figures the antiproton events marked with asterisks ($*$) are clearly

Table 5.1: The principal properties of the antiproton events. Energy (TOA) is for the kinetic energy at the top of the atmosphere.

	Flight	Run	Event No.	Rigidity (GV)	β	Energy (TOA) (MeV)	$(\text{Mass})^2$ $(\text{GeV/c}^2)^2$
1	BESS-93	14	535375	-1.083	0.743	531	0.949
2	BESS-93	15	711708	-0.914	0.696	413	0.889
3	BESS-93	18	1695042	-0.794	0.651	338	0.860
4	BESS-93	19	2197801	-0.994	0.756	467	0.741
5	BESS-93	22	3164639	-0.939	0.692	432	0.959
6	BESS-93	24	3597064	-0.933	0.704	430	0.887
7	BESS-94	6	456938	-1.069	0.737	522	1.014
8	BESS-94	16	949486	-0.620	0.564	248	0.845

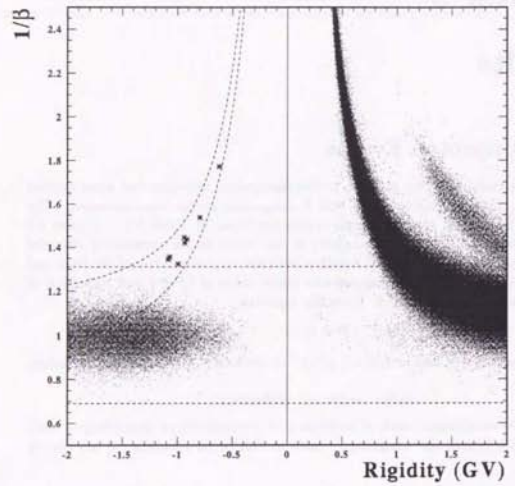

Figure 5.1: The identification of antiproton events (1). All the events that passed the event selection and the dE/dx cut are plotted. The dashed curves and the dashed line are the boundaries for the mass cut and the beta cut. The antiproton events are marked as ∗.

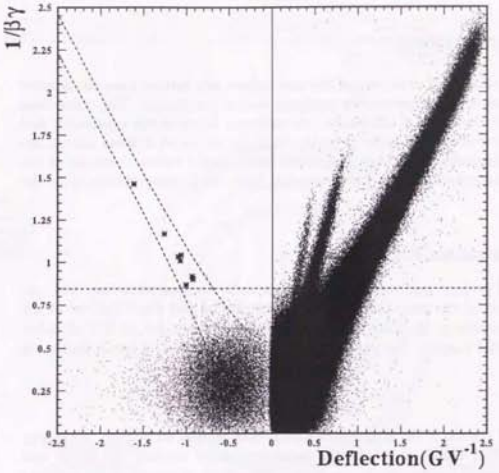

Figure 5.2: The identification of antiproton events (2). The same events as in (1) are plotted. The dashed curves and the dashed line are again the boundaries for the mass cut and the beta cut. The antiproton events are marked with asterisks (∗).

seen forming antiproton bands. Figure 5.3 to 5.10 show the reconstructed image of the antiproton events. There one can see the negatively curved tracks defined with enough hits. The trajectories are fitted to the hits in JET and IDCs excellently, and consistent with the hits in ODCs and TOFs, showing no signature of interactions nor large scattering. The events were no doubt made by incident antiprotons.

5.2 Corrections

The antiproton flux at the top of the atmosphere was derived from the number of the mass-resolved antiprotons by applying several corrections. The corrections were made for the selection efficiencies, the exposure factor of the experiment and the atmospheric effects. In order to make use of the measured incident angles, the calculations depending on energy were made based on the reduced energies at the top of the atmosphere, which were converted from the energies measured in the instrument.

5.2.1 Ionization Energy Loss

The observed protons and antiprotons had lost their energies while they had traversed 5 g/cm^2 of the atmosphere above the instrument and also 7.5g/cm^2 of the upper half material of the instrument before they were detected at JET chamber in the solenoidal magnet. The energy of a particle after traveling into a depth x is given as:

$$E(x) = E(0) - \int_0^x \frac{dE}{dx}(E)dx.$$

The energy at the top of the atmosphere E(0) is then derived when $E(x)$, the energy measured at JET chamber, dE/dx, the ionization energy loss per unit depth, and x, the thickness of the materials, are given. The actual thickness of the material for a particle to traverse was more than the minimum value (5+7.5)g/cm^2, due to the inclination of the trajectory. The energy loss at the individual steps, at the detector components of the instrument and in the atmosphere, were computed taking account of the angles between the trajectory and the tangent planes of the detector components and the incident zenith angle.

5.2.2 Exposure Factor

The geometrical acceptance of the BESS instrument was calculated by the Monte Carlo simulation to be about $0.5m^2sr$. The energy dependent acceptance is shown in Figure 5.11 denoted as 'SΩ'. The 'live time' were 3.1×10^4sec (8.6 hours) in BESS-93 flight and 2.6×10^4sec (7.3 hours) in BESS-94 flight. The total exposure factors for the flights were $S\Omega t^{93} \simeq 1.6\times10^4 m^2sr$·sec in BESS-93 and $S\Omega t^{94} \simeq 1.3\times10^4 m^2sr$·sec in BESS-94.

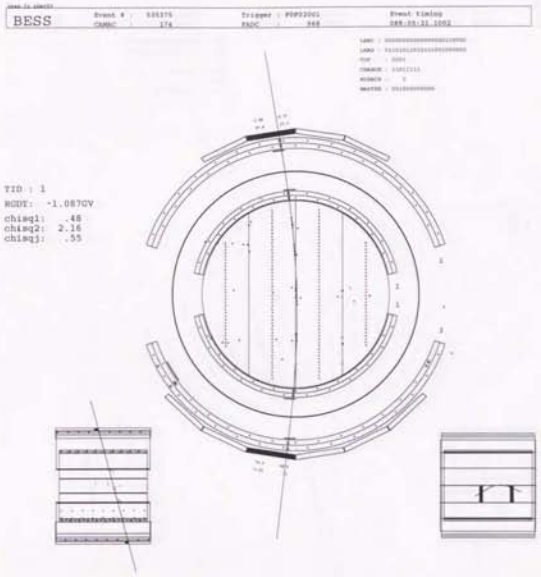

Figure 5.3: Event display of a $\bar{p}$ event collected in BESS-93 Run14.

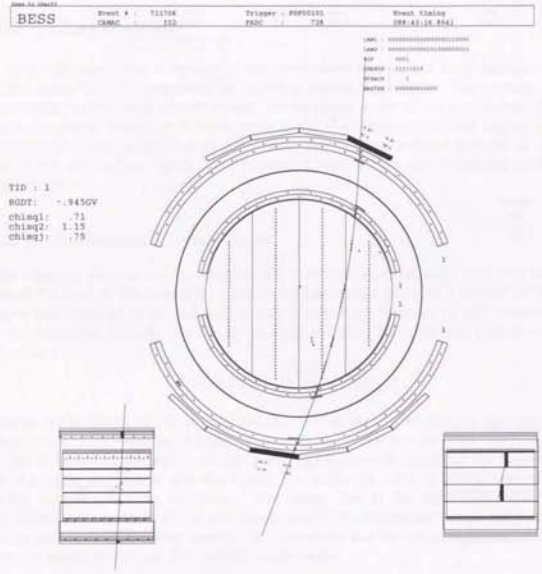

Figure 5.4: Event display of a $\bar{p}$ event collected in BESS-93 Run15.

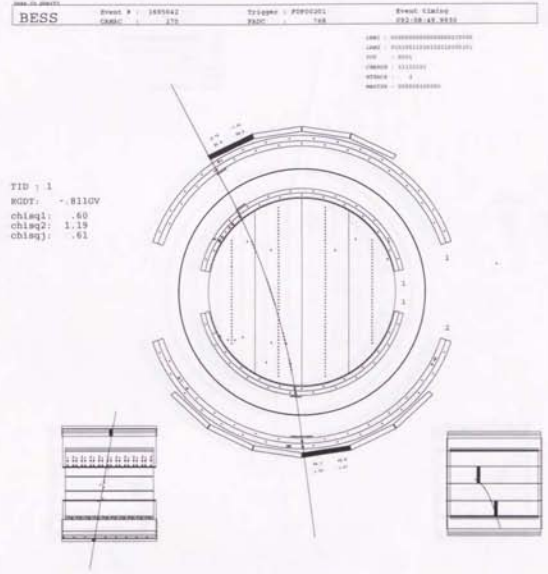

Figure 5.5: Event display of a $\bar{p}$ event collected in BESS-93 Run18.

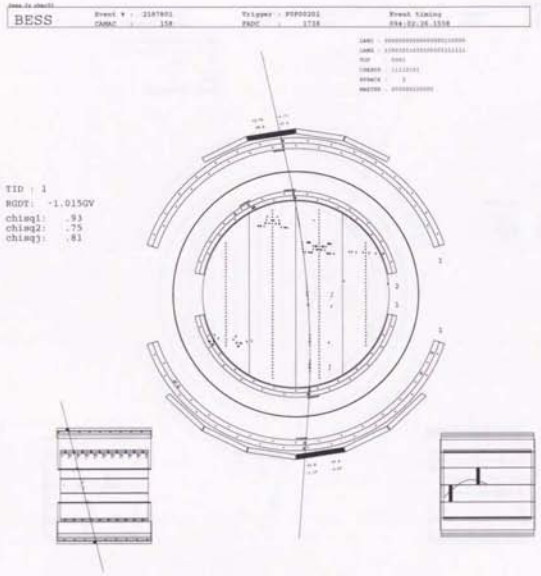

Figure 5.6: Event display of a $\bar{p}$ event collected in BESS-93 Run19.

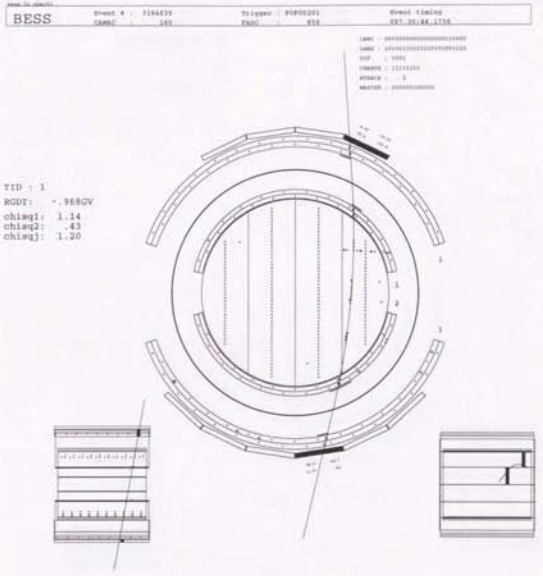

Figure 5.7: Event display of a $\bar{p}$ event collected in BESS-93 Run22.

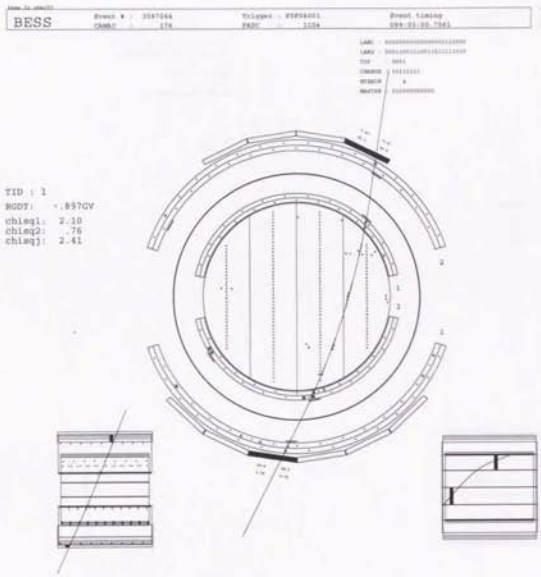

Figure 5.8: Event display of a $\bar{p}$ event collected in BESS-93 Run24.

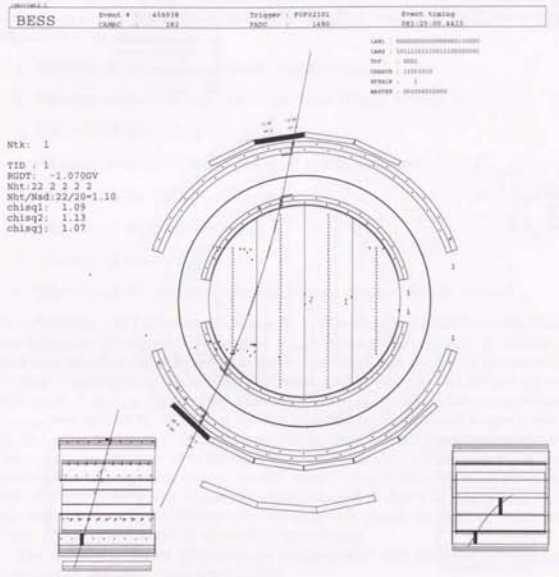

Figure 5.9: Event display of a $\bar{p}$ event collected in BESS-94 Run6.

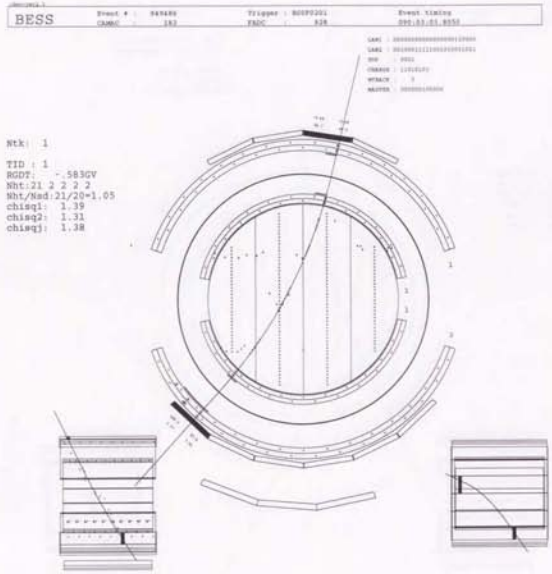

Figure 5.10: Event display of a $\bar{p}$ event collected in BESS-94 Run16.

5.2.3 Selection Efficiencies

The efficiencies of the selection cuts including the instrumental loss were derived from the actual flight data for proton events, except for the good single track selection, which was obtained from Monte Carlo simulations. In order to obtain the efficiencies for antiproton events, we calculated the ratios of the efficiencies for antiproton events to those for proton events. The efficiencies for antiproton events were derived by multiplying the calculated ratios and the actual efficiencies for proton events. The efficiencies to be obtained are:

1. Efficiency of the good single track selection (ε_{single}).
2. Efficiency of the Nhit selection in the Track Trigger module ($\varepsilon_{\text{TT-nhit}}$).
3. Efficiency of the track quality cut (ε_{tk}).
4. Efficiency of the selection for the good timing measurement. (ε_{tf}).
5. Efficiency of the $\mathrm{d}E/\mathrm{d}X$ cut ($\varepsilon_{dE/dx}$).
6. Efficiency of the mass cut (ε_{mass}).
7. Efficiency of the β cut (ε_{β}).
8. Efficiency of the deflection selection in Track Trigger module ($\varepsilon_{\text{TT-def}}$).

The efficiencies 1 to 7 are shown in Figure 5.11. Whereas the geometrical acceptance was defined as T0 trigger to be invoked, ε_{single} includes the efficiency of forming a track long enough to be analyzed. The antiproton events had undergone the selection in Track Trigger module, the efficiency of which are expressed as the product of two efficiencies — $\varepsilon_{\text{TT-nhit}}$ for the Nhit selection and $\varepsilon_{\text{TT-def}}$ for the deflection selection. $\varepsilon_{\text{TT-nhit}}$ were derived by simulating the Nhit selection on the unbiased trigger events. As for $\varepsilon_{\text{TT-def}}$, it cannot be derived by combining the efficiency for the actual proton events and the efficiency rate for the simulated antiproton/proton events. It was derived from the unbiased trigger sample events with negative charged particles. The efficiency of the Track Trigger deflection selection is shown in Figure 5.12. It is only needed to obtain the efficiency for the antiproton events, for most of the proton events are extracted from the unbiased trigger sample.

The samples to derive efficiencies for proton events were obtained by applying loose cuts on the good single track events;

- z=1
  Very loose cuts on $\mathrm{d}E/\mathrm{d}x$ at TOF counters just to rejecting events with z$\geq$2.
- $\left|\frac{1}{\beta} - \sqrt{\left(\frac{m_{\mathrm{p}}}{R}\right)^2 + 1}\right| < 0.3$
  A loose cut corresponding about $4\sigma_{\beta}$.

Since the events with positive rigidities were dominated by protons and heliums, the above cuts were efficient enough to extract proton event samples.

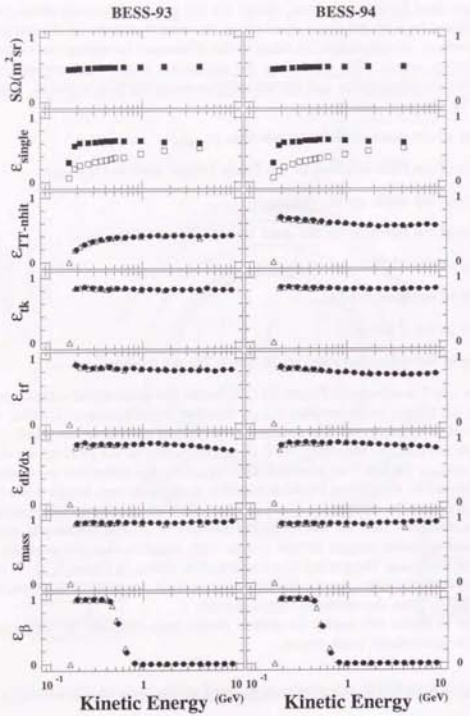

Figure 5.11: Instrumental and selection efficiencies for protons/antiprotons. Filled and open squares are calculated by simulation for protons and antiprotons, respectively; filled circles are obtained from flight data for protons; open triangles are for antiprotons, derived combining the flight data for protons and the efficiency ratio of antiprotons to protons.

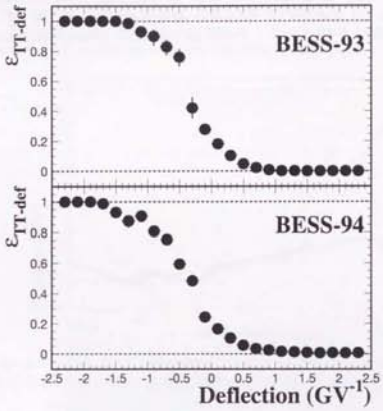

Figure 5.12: Track Trigger deflection selection efficiency

5.2.4 Atmospheric Secondary Production

Both protons and antiprotons can be produced above the instrument by collisions of the cosmic rays with the nuclei in the atmosphere. The observed number of the protons and antiprotons may include the atmospheric secondaries and these portions should be subtracted in order to obtain the primary flux at the top of the atmosphere. Figure 5.13 shows the calculated ratio of secondary protons to primary protons [52]. The ratio changes depending on the solar modulation, and we need to know the amount of the solar modulation at the time of BESS-93 and BESS-94 flights. As shown in Figure 3.1 in Chapter 3, the solar modulation was very close to the minimum and we adopted the ratio for minimum solar modulation. Figure 5.14 shows the calculations on secondary antiproton flux [6, 53, 54]. We adopted the flux by Mitsui [6], for it is based on the most detailed calculations,

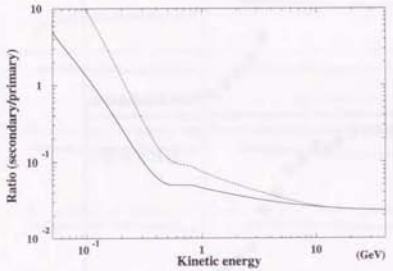

Figure 5.13: Secondary proton flux to primary proton flux ratio. at an atmospheric depth $5 g/cm^2$ for minimum solar modulation (solid curve) and for maximum (dashed curve).

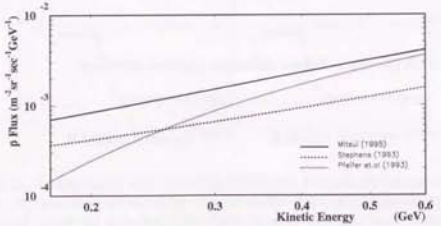

Figure 5.14: Secondary antiproton flux at an atmospheric depth $5 g/cm^2$.

performed three-dimensionally, including detailed effects of nuclear interactions in antiproton productions, and inelastic collisions of produced antiprotons. The dependence on the solar modulation is negligibly small for the secondary antiproton flux. The abscissa of these plots are the energy beneath the $5 g/cm^2$ of the atmosphere, and are needed to be converted into the energy at the top of the atmosphere in order to be applied to our data.

5.2.5 Re-entrant Albedo Particle

There could be 're-entrant albedo' particles which produced in deeper atmosphere than $5 g/cm^2$, moving upward at first, and then deflected by the geomagnetic field and enter the instrument moving downward. Calculations based on trajectory-tracing method were performed whereby the orbit of a particle of specified rigidity

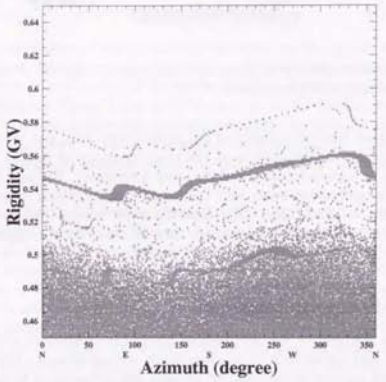

Figure 5.15: Rigidity cut-off for a zenith angle 0.495rad at a location in BESS-94 flight. Calculated for a location at 55°52.46N, 108°18.5W and 36.5km (119.76kft) above sea level, and a time 16:11(GMT) of August 1. of 1994. In the shaded region cosmic ray particles are forbidden to reach the instrument penetrating the magnetosphere. To the contrary, the particles in the open region are possibly cosmic-origin. The lowest energy antiproton event which was observed at this location and with this zenith angle, has the rigidity high enough to be of cosmic origin. The original program is provided by Dr. Shibata of Aoyama Gakuin University, based on the work of Reference [55].

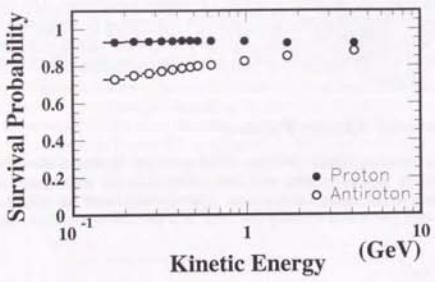

Figure 5.16: Survival probability of protons/antiprotons for 5g/cm^2 of the atmosphere. The losses are due to interactions.

was numerically traced through a model of the geomagnetic field, and whether the trajectory was extended to the outside of the magnetosphere or not for a given zenith and azimuth at a given location and time was determined. Figure 5.15 shows a calculation for the antiproton event with the lowest rigidity, which indicates the antiproton of rigidity −0.62GV had come from the outer space. The same thing can be said on the other antiproton events, i.e. they all are of cosmic origin and no correction factor is needed for re-entrant albedo particles.

5.2.6 Losses in the Atmosphere

Interactions in the 5 g/cm^2 of the atmosphere above the instrument reduce the number of protons and antiprotons to be observed in the experiment. Figure 5.16 shows the estimated survival probability for protons and antiprotons to penetrate 5g/cm^2 of the atmosphere for various initial energies at the top of the atmosphere [31]. The survival probability for antiprotons declines at low energies due to the annihilations, while that for protons is almost constant over the entire energy range.

5.2.7 Interactions in the Atmosphere

The ionization energy loss and the decrease of the flux due to the interactions in the atmosphere are considered in Section 5.2.1 and Section 5.2.6. In this section, we consider the deformation of the antiproton spectrum due to elastic and inelastic interactions with the nuclei in the atmosphere.

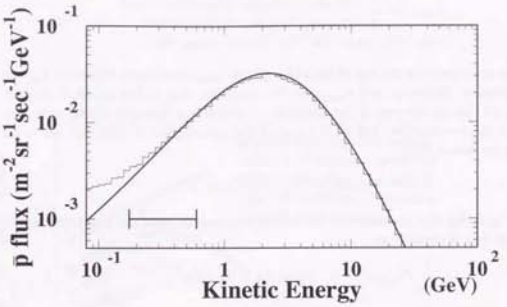

Figure 5.17: Deformation of the antiprotons spectrum due to 5g/cm^2 of the residual atmosphere above the instrument, calculated by a Monte Carlo simulation. The predicted antiproton flux at the top of the atmosphere based on the standard leaky box model (the curve, see Figure 1.1 or 5.19) is assumed as the incident spectrum. The energy losses by strong interactions produce low energy antiprotons and deform the spectrum (the histogram, made by the Monte Carlo simulation). The deformation is negligibly small at the energies covered by this experiment (the horizontal bar).

A fraction of the antiprotons incident onto the atmosphere will suffer elastic or inelastic interactions in traveling through the 5g/cm^2 of the air, producing secondary antiprotons with lower energies. This might result in a deformation of the measured spectrum. In order to see the magnitude of the effect, a Monte Carlo simulation was performed, in which the energy and the angular distribution of the secondary antiprotons was simulated [6] rather precisely at all incident antiproton energies. The resultant antiproton spectrum at 5g/cm^2 of the atmospheric depth is shown in Figure 5.17 as the histogram and is compared to the assumed incident spectrum of the leaky box model (solid curve). As seen in the Figure, the spectrum deformation is negligibly small at least in the energy range covered by this experiment. We thus neglect this effect in deduceing the spectrum at the top of the atmosphere from the obtained specturm at 5g/cm^2 of the atmospheric depth.

5.2.8 Summary of Corrections

The number of events observed in the instrument is converted into the expected number of incident particles using the selection efficiencies;

$$N_{in}(E) = N_{obs}(E) \,/\, \varepsilon(E)$$
$$\varepsilon(E) = \varepsilon_{trig}(E)\varepsilon_{sel}(E)$$

$$\varepsilon_{trig} = \begin{cases} \varepsilon_{TT-nhit} \cdot \varepsilon_{TT-def} & (for antiprotons) \\ \varepsilon_{TT-nhit} \cdot r_{sample} & (for protons) \end{cases}$$
$$\varepsilon_{sel} = \varepsilon_{single} \cdot \varepsilon_{tk} \cdot \varepsilon_{tf} \cdot \varepsilon_{dE/dx} \cdot \varepsilon_{mass} \cdot \varepsilon_{\beta},$$

where E is the energy at the top of the atmosphere, ε_{trig} the trigger efficiency, ε_{sel} the overall selection efficiency, and r_{sample} is the sampling rate of the unbiased trigger. The reduced flux at the top of the instrument, which is a function of the energy at the top of the atmosphere, not at the top of the instrument, is then derived using the exposure factor $S\Omega t$;

$$F_{TOI}(E) = N_{in}(E)/S\Omega(E)\, t.$$

This flux includes the atmospheric secondary component, and the primary component of the flux is derived as:

$$F'_{TOI}(E) = F_{TOI}(E) - F_{air}(E)$$
or
$$F'_{TOI}(E) = F_{TOI}(E)/(1 + R_{air}(E))$$

where $F_{air}(E)$ is the atmospheric secondary flux and $R_{air}(E)$ the ratio of the atmospheric secondary flux to primary flux. The flux at the top of the atmosphere is then obtained applying the correction factor for the atmospheric loss $1/\eta$;

$$F_{TOA}(E) = F'_{TOI}(E)/\eta(E)$$

Summarizing the above steps, one can obtain a formula;

$$F_{TOA}(E) = \frac{N_{obs}(E)}{\varepsilon(E)} \cdot \frac{1}{S\Omega(E) \cdot t} \cdot \frac{1}{1 + R_{air}(E)} \cdot \frac{1}{\eta(E)} \tag{5.1}$$

or

$$F_{TOA}(E) = \left(\frac{N_{obs}(E)}{\varepsilon(E)} \cdot \frac{1}{S\Omega(E) \cdot t} - F_{air}(E) \right) \cdot \frac{1}{\eta(E)} \tag{5.2}$$

5.3 Proton Flux

The proton flux at the top of the atmosphere is derived using the formula (5.1) in Section 5.2.8;

$$F_p = \frac{N_p^{obs}}{\varepsilon_p S\Omega t} \cdot \frac{1}{1 + R_p^{air}} \cdot \frac{1}{\eta_p}, \tag{5.3}$$

where the subscripts p denote that the value for of protons; for instance, N_p^{obs} is the number of the observed proton events. and ε_p the total selection efficiency for proton events. Figure 5.18 shows the proton flux obtained from the BESS-93 and BESS-94 data. Both before and after the atmospheric corrections, the correction for the losses and for the secondary productions, are plotted. Also shown are the calculations of

95/12/08 11:42

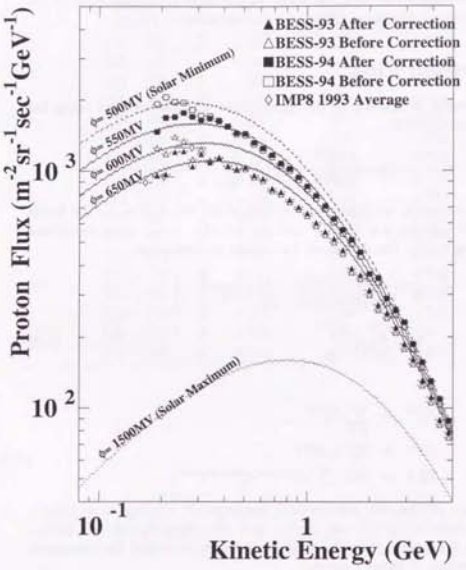

Figure 5.18: Proton fluxes obtained for BESS-93 (triangles) and BESS-94 (squares) flights, being compared to a model of the proton flux fitted to the LEAP experiment [57]. The open marks are the flux before applying the atmospheric corrections, the filled are after the corrections.

proton flux derived from an assumed interstellar spectrum $F(p) \propto p^{-\gamma}$ [56], where p is momentum and $\gamma \simeq 2.74$ [57]. The effect of solar modulation is calculated using the force field approximation [58], in which a single parameter ϕ indicates the amount of modulation. The spectra of BESS-93 and BESS-94 proton flux show an agreement with ϕ=650MV and 550MV respectively. The flux of BESS-93 is also in agreement with the year-averaged data from the *IMP 8* satellite (see, for example, Reference [59] for description of the experiment), which were kindly provided by Dr. E. S. Seo of University of Maryland (Private communication).

5.4 Antiproton Flux

The flux of antiprotons at the top of the atmosphere was also derived using the formula (5.2) in Section 5.2.8;

$$F_{\bar{p}} = \left(\frac{N_{\bar{p}}^{obs}}{\varepsilon_{\bar{p}} S\Omega t} - F_{\bar{p}}^{air} \right) \cdot \frac{1}{\eta_{\bar{p}}}$$

To obtain a better statistics, we combined the data of the two flights, for the fluxes under different solar activity, $\phi = 650MV$ and $\phi = 550MV$ do not show significant differences according to [6]. The combined flux would be derived as:

$$\begin{aligned} F_{\bar{p}} &= \left(\frac{N_{\bar{p}}^{93} + N_{\bar{p}}^{94}}{\varepsilon_{\bar{p}}^{93} t^{93} + \varepsilon_{\bar{p}}^{94} t^{94}} \cdot \frac{1}{S\Omega} - F_{\bar{p}}^{air} \right) \cdot \frac{1}{\eta_{\bar{p}}} \\ &= \frac{N_{\bar{p}}^{obs} - N_{\bar{p}}^{air}}{\varepsilon_{\bar{p}} S\Omega \, t \, \eta_{\bar{p}}} \end{aligned} \tag{5.4}$$

where

$$\begin{aligned} N_{\bar{p}}^{obs} &= \sum_{year} N_{\bar{p}}^{year} \\ N_{\bar{p}}^{air} &= F_{\bar{p}}^{air} \varepsilon_{\bar{p}} S\Omega \, t \\ \varepsilon_{\bar{p}} S\Omega \, t &= S\Omega \cdot (\sum \varepsilon_{\bar{p}}^{trig,year} \varepsilon_{\bar{p}}^{sel,year} t^{year}) \end{aligned}$$

are the total number of observed antiprotons, the expected number of secondary antiprotons to be observed in the two flights, and the effective exposure factor, respectively. Table 5.2 summarizes the number of antiprotons and the correction factors at small intervals of kinetic energies.

For a better statistics again, we cumulated these values in the energy intervals 175 to 350MeV, 350 to 500MeV and 500 to 600MeV;

$$F'_{\bar{p}}(ER) \equiv \frac{\sum_{ER} (N_{\bar{p}}^{obs}(E_i) - N_{\bar{p},i}^{air}(E_i))}{\sum_{ER} (\varepsilon_{\bar{p}}(E_i) S\Omega(E_i) \, t \, \eta_{\bar{p}}(E_i))} \tag{5.5}$$

where ER is the energy range of cumulation. This time the expected value of $F_{\bar{p}} = F_{\bar{p}}(E)$ in the individual elements of cumulation are obviously not the same,

Table 5.2: Summary of the number of antiprotons and the correction values to derive the $\bar{p}$ flux. $N_{\bar{p}}^{obs}$ is the number of observed antiprotons, $N_{\bar{p}}^{air}$ the expected number of background antiprotons produced in the atmosphere, $\varepsilon_{\bar{p}} S\Omega t$ the effective exposure factor, and $\eta_{\bar{p}}$ the probability for an antiproton to penetrate $5g/cm^2$ of the atmosphere.

Energy (MeV)	$N_{\bar{p}}^{obs}$	$N_{\bar{p}}^{air}$	$\varepsilon_{\bar{p}} S\Omega t$ ($\times 10^3 m^2 sr \cdot sec$)	$\eta_{\bar{p}}$
175 – 200	0	0.021	1.37	0.735
200 – 225	0	0.037	1.93	0.744
225 – 250	1	0.050	2.14	0.752
250 – 275	0	0.063	2.30	0.759
275 – 400	0	0.080	2.51	0.765
300 – 325	0	0.099	2.74	0.770
325 – 350	1	0.114	2.77	0.774
350 – 375	0	0.129	2.80	0.778
375 – 400	0	0.146	2.85	0.782
400 – 425	1	0.163	2.89	0.785
425 – 450	2	0.178	2.88	0.788
450 – 475	1	0.183	2.72	0.791
475 – 500	0	0.181	2.50	0.794
500 – 525	1	0.171	2.20	0.796
525 – 550	1	0.155	1.86	0.799
550 – 575	0	0.135	1.52	0.801
575 – 600	0	0.114	1.21	0.803

hence;

$$\overline{F_{\bar{p}}}(ER) \equiv \frac{\int_{ER} F_{\bar{p}}(E) dE}{\int_{ER} dE} \neq \frac{\int_{ER} F_{\bar{p}}(E) \varepsilon_{\bar{p}} S\Omega(E) \, t \, \eta_{\bar{p}}(E) dE}{\int_{ER} \varepsilon_{\bar{p}} S\Omega(E) \, t \, \eta_{\bar{p}}(E) dE} \simeq F'_{\bar{p}}(ER)$$

where $\overline{F_{\bar{p}}}(ER)$ is the average flux in a energy range ER. Yet the error of the $F'_{\bar{p}}(ER)$ as a estimator of $\overline{F_{\bar{p}}}(ER)$ would be limited as:

$$| \overline{F_{\bar{p}}}(ER) - F'_{\bar{p}}(ER) | < \max\{F_{\bar{p}}(E); E \text{ in } ER\} - \min\{F_{\bar{p}}(E); E \text{ in } ER\} \tag{5.6}$$

We adopted the $F'_{\bar{p}}(ER)$ as the estimator of $\overline{F_{\bar{p}}}(ER)$ and the cumulated number of antiprotons and correction factors are summarized in Table 5.3.

Table 5.3: The cumulated values and the $\bar{p}$ flux.

Energy (MeV)	$N_{\bar{p}}^{obs}$	$N_{\bar{p}}^{air}$	$\varepsilon_{\bar{p}} S\Omega t \eta_{\bar{p}}$ $(m^2 sr \cdot sec)$	$F_{\bar{p}}(ER)$ $(m^{-2} sr^{-1} sec^{-1} GeV^{-1})$
175 – 350	2	0.465	1.70×10^{3}	5.15×10^{-3}
350 – 500	4	0.981	2.18×10^{3}	9.23×10^{-3}
500 – 600	2	0.575	1.36×10^{3}	1.05×10^{-2}

Statistical error

The statistical error of the flux was derived from 84.13% C.L. upper and lower limits, which corresponds to 1σ of a Gaussian distribution. The upper and lower limits on the number of antiprotons, N^U and N^L, were defined by the equations for a Poisson process with background [60];

$$CL \geq \left(\sum_{n=0}^{n_0} e^{-(\mu_B+N^U)} \frac{(\mu_B+N^U)^n}{n!}\right) \Big/ \left(\sum_{n=0}^{n_0} e^{-\mu_B} \frac{\mu_B^n}{n!}\right) \tag{5.7}$$

$$CL \geq \left(\sum_{n=n_0}^{\infty} e^{-(\mu_B+N^L)} \frac{(\mu_B+N^L)^n}{n!}\right) \Big/ \left(\sum_{n=n_0}^{\infty} e^{-\mu_B} \frac{\mu_B^n}{n!}\right) \tag{5.8}$$

where CL is the confidence level, n_0 the observed number and μ_B the mean of the background. The statistical errors of the antiproton flux are summarized in Table 5.4.

Table 5.4: Statistical errors of the $\bar{p}$ flux.

ER	Energy (MeV)	$N_{\bar{p}}^{obs}$	$N_{\bar{p}}^{air}$	Confidence Limits (84.13% C.L.)	$F_{\bar{p}}(ER)$ $(m^{-2} sr^{-1} sec^{-1} GeV^{-1})$	Error
ER1	175 – 350	2	0.47	≤ 4.13	5.1×10^{-3}	$+8.9\times10^{-3}$
				≥ 0.41		-3.7×10^{-3}
ER2	350 – 500	4	0.98	≤ 6.19	9.2×10^{-3}	$+9.7\times10^{-3}$
				≥ 1.18		-5.6×10^{-3}
ER3	500 – 600	2	0.58	≤ 4.09	1.0×10^{-2}	$+2.0\times10^{-2}$
				≥ 0.40		-0.8×10^{-2}

Systematic error

The expression of the error of the antiproton flux will be derived from equation(5.4), assuming the variables are independent;

$$\left(\frac{\Delta F_{\bar{p}}}{F_{\bar{p}}}\right)^2 = \left(\frac{\Delta N_{\bar{p}}^{obs}}{N_{\bar{p}}^{obs} - N_{\bar{p}}^{air}}\right)^2 + \left(\frac{\Delta N_{\bar{p}}^{air}}{N_{\bar{p}}^{obs} - N_{\bar{p}}^{air}}\right)^2 + \left(\frac{\Delta \varepsilon_{\bar{p}}}{\varepsilon_{\bar{p}}}\right)^2 + \left(\frac{\Delta(S\Omega)}{S\Omega}\right)^2 + \left(\frac{\Delta t}{t}\right)^2 + \left(\frac{\Delta \eta_{\bar{p}}}{\eta_{\bar{p}}}\right)^2 \tag{5.9}$$

The first term is the statistical error argued above, and the others are systematic errors. The systematic errors were categorized as follows;

1. Error of the geometrical acceptance $S\Omega$

   The geometrical acceptance was obtained from the Monte Carlo simulation and there could be an ambiguity due to possible misalignment of the detector components.

   $$\left(\frac{\Delta(S\Omega)}{S\Omega}\right) \simeq \pm 5\%$$

2. Error of the 'live time' t

   The effective exposure time, or 'live time' t was derived from total exposure time and the ratio of the actually issued triggers to the satisfaction of the trigger conditions. The total exposure time was derived by summing up the time difference of the first and the last event of each run. The time information of the events were obtained from the on-board clock with a precision of 0.1ms, which is small enough compared to 7–11ms of the average interval between the events. Supposing this interval to be the ambiguity of the exposure time in each run, it is negligibly small compared to the period of a run which is about one hour. The number of the trigger issued and that of the satisfaction of the trigger condition were more than 1×10^8, therefore, the ratio of them includes negligible error.

   $$\left(\frac{\Delta t}{t}\right) \simeq 0$$

3. Error of the efficiencies

   The efficiencies used in deriving antiproton flux were composed of the actual selection efficiencies for protons and the ratio of efficiencies of antiproton selection to proton selection in the Monte Carlo simulations. The error of them was dominated by the errors in simulations. There were ambiguities in the simulations due to the difference between the simulated and actual responce of the instrument.

   - *responce for protons* — Comparing the efficiencies obtained from simulations and from the flight data, the error was estimated at about 5% at energies below 350MeV (ER1) and 3% above 350MeV (ER2-3). In the

simulation, there could be an error of the reaction cross section of protons on nuclei. Assuming the error to be 30%, this cause errors of efficiencies of 10% at ER1 and 8% at ER2-3. The errors of the efficiencies for protons are, therefore, 11.2% at ER1 and 8.5%

- *responce for antiprotons* — There was no reference to which the efficiencies for antiprotons derived from the simulations be compared, hence the error was deduced without any comparison. Cross sections of interactions could have included uncertainties of about 30%. The uncertainty of the amount of materials in the instrument was estimated at about 4%, which corresponds to the errors about 5% at energies below 350MeV and 2% above 350MeV. We estimated the errors in the efficiency for antiprotons at 30.4% at energies below 350MeV and 30.1% above 350MeV.
- *Rigidity measurement* — The efficiency estimation had been made energy-dependently. The kinetic energy was derived from the rigidity, which is obtained from the curvature of the trajectory. If the measurement of rigidities had been incorrect, references to the efficiencies obtained from the simulations would have been wrong especially at low energies where the efficiency for antiprotons shows a large energy dependence. As indicated in Figure 4.28, 3% of error in rigidities could be found as the shift in the instrumental cutoff. We concluded the error in rigidity measurement was within 3%, causing errors at most 15% in the energy region below 350MeV and 4% above 350Mev.
- *Bias by the selection cuts* — The selection criteria were determined based on the distributions of the cut parameters of the flight data, hence reflecting those of the proton events. If any distribution of the parameters of antiproton events were different from that of proton events, the selection cut would have biased the result. As shown in Figures 4.34 to 4.43, there could not found any proton-antiproton asymmetry in the distribution of the cut parameters beyond the statistical dispersion.

The error in the ratio was then estimated at about 8.6% at energies below 350MeV and 6.2% above 350MeV.

$$\frac{\Delta\varepsilon_{\bar{p}}}{\varepsilon_{\bar{p}}} \simeq \begin{cases} \pm 36\% & (175MeV \leq E < 350MeV) \\ \pm 32\% & (350MeV \leq E < 600MeV) \end{cases}$$

4. Atmospheric losses of antiprotons

The losses of antiprotons due to the annihilations and the inelastic collisions in the atmosphere were estimated by Monte Carlo simulations. There were ambiguities in the estimation due to the cross sections used in the simulation and the simplified model of the atmosphere.

$$\frac{\Delta\eta_{\bar{p}}}{\eta_{\bar{p}}} \simeq \frac{1-\eta_{\bar{p}}}{\eta_{\bar{p}}}\frac{\Delta\sigma_{\bar{p}}}{\sigma_{\bar{p}}} \simeq \begin{cases} \pm 11\% & (175MeV \leq E < 350MeV) \\ \pm 9\% & (350MeV \leq E < 500MeV) \\ \pm 8\% & (500MeV \leq E < 600MeV) \end{cases},$$

where $\sigma_{\bar{p}}$ is the cross section.

5. Atmospheric secondary antiprotons

The calculation of the atmospheric secondary antiproton flux includes uncertainties of cross section of antiproton production and the interactions of produced antiprotons in the atmosphere. The value of $N_{\bar{p}}{}^{air}$ could change by a factor 2 [6]. The corresponding systematic error of the flux was:

$$\frac{\Delta N_{\bar{p}}^{air}}{N_{\bar{p}}^{obs} - N_{\bar{p}}^{air}} \simeq \begin{cases} +36\%/-18\% & (175MeV \leq E < 350MeV) \\ +39\%/-19\% & (350MeV \leq E < 500MeV) \\ +42\%/-21\% & (500MeV \leq E < 600MeV) \end{cases}$$

6. Error due to the cumulation method There would be an error caused by the the energy interval cumulation formula (5.5). Since both of the correction factor $\varepsilon_{\bar{p}}(E)S\Omega(E)\,t\,\eta_{\bar{p}}(E)$ and the observed antiproton flux $F_{\bar{p}}(E)$ seem to be monotonically increasing in the energy range of interest, the error would be smaller than the limit in (5.6). The errors are estimated as follows;

$$\frac{\Delta F_{\bar{p}}}{F_{\bar{p}}} \leq \begin{cases} \dfrac{F_{\bar{p}}(ER2) - F_{\bar{p}}(ER1)}{4F_{\bar{p}}(ER1)} = 20\% & (ER1 : 175MeV \leq E < 350MeV) \\ \dfrac{F_{\bar{p}}(ER3) - F_{\bar{p}}(ER1)}{8F_{\bar{p}}(ER2)} = 7\% & (ER2 : 350MeV \leq E < 500MeV) \\ \dfrac{F_{\bar{p}}(ER3) - F_{\bar{p}}(ER2)}{4F_{\bar{p}}(ER3)} = 3\% & (ER3 : 500MeV \leq E < 600MeV) \end{cases}$$

Table 5.5 summarizes the systematic uncertainties.

Table 5.5: Summary of systematic errors of $\bar{p}$ flux.

Sources	175-350 MeV (%)	350-500 MeV (%)	500-600 MeV (%)
Geometrical acceptance	±5	±5	±5
Effective exposure time	±0	±0	±0
Efficiencies	±36	±32	±32
Atmospheric secondary antiprotons	+36/−18	+39/−19	+42/−21
Atmospheric lossses of antiprotons	±11	±9	±8
Cumulation method	±20	±7	±3
Total	+56/−47	+52/−39	+54/−40

Result

The antiproton flux obtained in the present analysis is:

$$F_{\bar{p}} = \begin{cases} (5.1\ ^{+8.9}_{-3.7}\ ^{+2.9}_{-2.4}) \times 10^{-3} & (175MeV \leq E < 350MeV) \\ (9.2\ ^{+9.7}_{-5.6}\ ^{+4.8}_{-3.6}) \times 10^{-3} & (350MeV \leq E < 500MeV) \\ (1.0\ ^{+2.0}_{-0.8}\ ^{+0.5}_{-0.4}) \times 10^{-2} & (500MeV \leq E < 600MeV) \end{cases}$$

where the first errors are statistical and the second systematic. Figure 5.19 shows the result compared with the predicted spectra and the results of the other experiments.

5.5 $\bar{p}/p$ ratio

To compare our result with the previous experiments, the ratio of the antiproton flux to the proton flux was obtained. According to the formulae (5.3) and (5.4), the averaged antiproton flux in an energy range ER was obtained as:

$$F_{\bar{p}}(ER) \simeq \sum_{ER}(N_{\bar{p}}^{obs} - N_{\bar{p}}^{air}) \Big/ \sum_{ER} \varepsilon_{\bar{p}} S\Omega\, t\, \eta_{\bar{p}} \tag{5.10}$$

The corresponding proton flux is obtained as:

$$F_p(ER) = \sum_{ER} F_p(E_i) \Big/ \sum_{ER} 1 \tag{5.11}$$

$$F_p(E_i) \equiv \sum_{year} \frac{N_{\bar{p}}^{year}(E_i)}{\varepsilon_{\bar{p}}^{year} S\Omega t^{year}\, \eta_{\bar{p}}} \varepsilon_{\bar{p}}^{year} S\Omega t^{year}\, \eta_{\bar{p}} \Big/ \sum_{year} \varepsilon_{\bar{p}}^{year} S\Omega t^{year}\, \eta_{\bar{p}} \tag{5.12}$$

$$= \sum_{year} \frac{N_{\bar{p}}^{year}}{\varepsilon_{\bar{p}}^{year}} \varepsilon_{\bar{p}}^{year} \Big/ \sum_{year} \varepsilon_{\bar{p}}^{year} S\Omega t^{year} (1 + R_p^{air})\, \eta_p \tag{5.13}$$

Since there are large number of proton events and the statistical errors are small enough, the year cumulation was made using the same weight as for antiprotons, and the energy interval cumulation was done to make a simple average. Hence the ratio is obtained as:

$$\frac{\bar{p}}{p} = \frac{\sum_{ER}(N_{\bar{p}}^{obs} - N_{\bar{p}}^{air}) \Big/ \sum_{ER} \varepsilon_{\bar{p}} S\Omega\, t\, \eta_{\bar{p}}}{\sum_{ER}(\hat{N}_p^{obs}/\varepsilon_{\bar{p}} S\Omega t\, (1 + R_p^{air})\, \eta_p) \Big/ \sum_{ER} 1} \tag{5.14}$$

$$\hat{N}_p^{obs} \equiv \sum_{year} \frac{N_{\bar{p}}^{year}}{\varepsilon_{\bar{p}}^{year}} \varepsilon_{\bar{p}}^{year}$$

$$\varepsilon_{\bar{p}} S\Omega t \equiv \sum_{year} \varepsilon_{\bar{p}}^{year} S\Omega t^{year}$$

In Table 5.6 are summarized the cumulated values used in the formula(5.14).

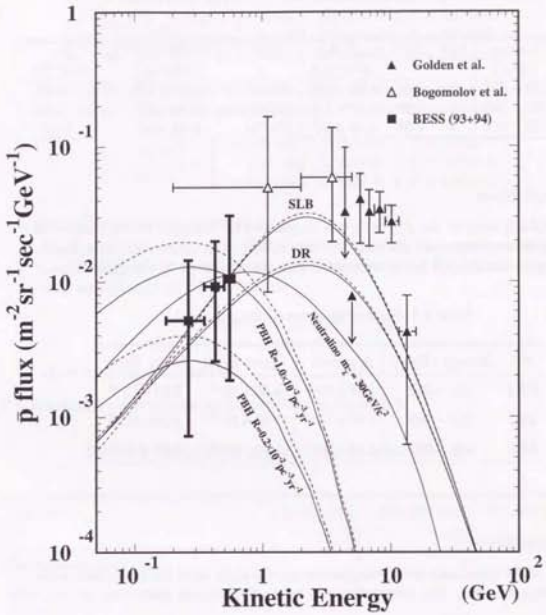

Figure 5.19: Measured $\bar{p}$ flux in comparison with the results of the other experiments and calculations. Filled squares, the present result; filled triangles, Golden *et al.*[23, 24]; open triangles, Bogomolov *et al.*[26, 27, 24]. The curves labeled "SLB" and "DR" are recently calculated by Mitsui [6] based on Standard Leaky Box Model and Diffusive Reacceleration Model, respectively. The dashed curves are for the minimum solar modulation and the solid are for $\phi = 600MV$. The curves labeled "PBH" are calculations on the $\bar{p}$ production by Primordial Black Holes for two values of the evapolation rate R by Maki *et al.*[15]. The dashed and solid curves are again for the minimum and $\phi = 600MV$ solar modulations. The curve labeled "Neutralino" is the calculation from the model of the proton flux (see Figure 5.18) and the $\bar{p}/p$ ratio by Jungman and Kamionkowski based on the $\bar{p}$ production by annihilations of dark matter neutralinos [17].

Table 5.6: The cumulated values used in the $\bar{p}/p$ determination.

ER	Energy (MeV)	$N_{\bar{p}}^{obs}$	$N_{\bar{p}}^{air}$	$\varepsilon_{\bar{p}} S\Omega\, t\, \eta_{\bar{p}}$ $(m^2 sr\, sec)$	N_p^{obs}	$\varepsilon_p S\Omega\, t\, (1+R_p^{air})\, \eta_p$ $(m^2 sr\, sec)$	$\bar{p}/p$ $(\times 10^{-6})$
ER1	175 – 350	2	0.47	1.20×10^4	627598	1.74×10^4	3.58
ER2	350 – 500	4	0.98	1.31×10^4	547830	1.66×10^4	7.00
ER3	500 – 600	2	0.58	0.54×10^4	172700	6.68×10^3	10.35

Statistical Error

The statistical error of the $\bar{p}/p$ ratio was dominated by the error of the number of the antiprotons events and derived from its 84.13% C.L. upper and lower limits. According to the Table 5.4, the statistical erros are derived as in the Table 5.7,

Table 5.7: Statistical errors of the $\bar{p}/p$ ratio .

ER	Energy (MeV)	$\bar{p}/p$ ratio	Upper Error	Lower Error
ER1	175 – 350	3.58×10^{-6}	6.20×10^{-6}	2.58×10^{-6}
ER2	350 – 500	7.00×10^{-6}	7.35×10^{-6}	4.26×10^{-6}
ER3	500 – 600	1.03×10^{-5}	1.94×10^{-5}	7.45×10^{-6}

Systematic Error

Most of the systematic error components are the same as in the systematic error of the antiproton flux. The uncertainties to be considered here are:

1. Exposure factor $S\Omega\, t$

   The geometrical factor $S\Omega$ was nearly constant over the measurement energy interval and the 'live time' t was constant in the individual flights. Hence, the exposure factor $S\Omega\, t$ which appears in both the proton and antiproton fluxes would almost cancel out, negligibly contributing to the error of the $\bar{p}/p$ ratio .

2. Atmospheric secondary protons

   We used the ratio of secondary proton flux to primary flux for minimum solar modulation, though the amount of the modulation was estimated a little more than the minimum. Using the ratio for the solar maximum, the $\bar{p}/p$ ratio would increase by 40% in ER1, and 10% in ER2 and 5% in ER3. We

estimated the error in the ratio at:

$$\frac{\Delta(1+R_p air)^{solar}}{(1+R_p air)} = \begin{cases} +6\% & (175MeV \le E < 350MeV) \\ +1.5\% & (350MeV \le E < 500MeV) \\ +0.8\% & (500MeV \le E < 600MeV) \end{cases}$$

There could also be about 5% of uncertainty of the cross section. Combining with the error due to the solar modulation, the error in the ratio is:

$$\frac{\Delta(1+R_p air)}{(1+R_p air)} = \begin{cases} +8\%/-5\% & (175MeV \le E < 350MeV) \\ +5\%/-5\% & (350MeV \le E < 500MeV) \\ +5\%/-5\% & (500MeV \le E < 600MeV) \end{cases}$$

3. Atmospheric losses of protons

   The losses of protons due to inelastic collisions in the atmosphere were estimated using Monte Carlo simulations. There could be uncertainties in the cross section used in the simulations;

$$\frac{\Delta\eta_p}{\eta_p} \simeq \frac{1-\eta_p}{\eta_p}\frac{\Delta\sigma_p}{\sigma_p} \simeq \pm 3\%$$

   where σ_p is the cross section.

The systematic uncertainties are summarized in Table 5.5.

Table 5.8: Summary of systematic errors of the $\bar{p}/p$ ratio .

Sources	175-350 MeV (%)	350-500 MeV (%)	500-600 MeV (%)
Geometrical acceptance	0	0	0
Effective exposure time	0	0	0
Efficiencies	±36	±32	±32
Atmospheric secondary protons ...	+8/ − 5	±5	±5
Atmospheric secondary antiprotons	+36/−18	+39/−19	+42/−21
Atmospheric lossses of protons	±3	±3	±3
Atmospheric lossses of antiprotons	±11	±9	±8
Cumulation method	±20	±7	±3
Total	+56/−47	+52/−39	+54/−40

Result

The ratio of antiproton flux to proton flux was derived as:

$$\bar{p}/p = \begin{cases} (3.6\,^{+6.2}_{-2.6}\,^{+2.0}_{-1.7}) \times 10^{-6} & (ER1: 175 - 350 MeV) \\ (7.0\,^{+7.3}_{-4.3}\,^{+3.6}_{-2.7}) \times 10^{-6} & (ER2: 350 - 500 MeV) \\ (1.0\,^{+1.9}_{-0.7}\,^{+0.5}_{-0.4}) \times 10^{-5} & (ER3: 500 - 600 MeV) \end{cases}$$

where the first errors are statistical and the second systematic. The result is shown in Figure 5.20 compared with the predicted spectra and the results of the other experiments, including the data from the very recent report of the IMAX experiment [65].

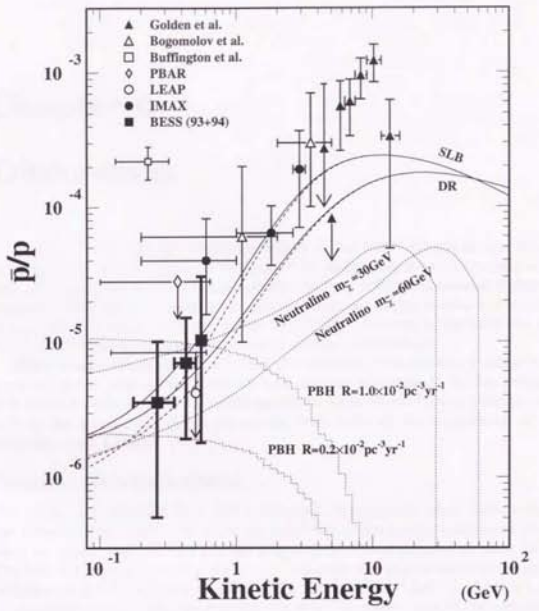

Figure 5.20: Measured $\bar{p}/p$ ratio in comparison with the other experimental data and calculations. Filled squares, the present result; open square, Buffinton *et al.*[25]; filled triangles, Golden *et al.*[23]; open triangles, Bogomolov *et al.*[26, 27]; open diamond, the PBAR experiment [28]; open circles, the LEAP experiment [29, 30]; filled circles, the recent result of IMAX *et al.*[65]; The dashed curves labeled "SLB" and "DR" are recently calculated by Mitsui [6] based on standard leaky box model and diffusive reacceleration model, respectively. The dotted lines labeled "PBH" are prediction of Maki *et al.*[15] for the $\bar{p}$'s produced by primordial black holes with the assumed evapolation rates $R = 0.2 \times 10^{-2} pc^{-3} yr^{-1}$. The dotted lines labeled "Neutralino" are the prediction of Jungman and Kamionkowski for the $\bar{p}$ productions by annihilations of dark matter neutralinos [17].

Chapter 6

Discussions

The new results for the antiproton flux from the BESS experiment are shown in Figure 5.19, and the $\bar{p}/p$ ratio in Figure 5.20, along with the other experimental data and recent predictions. They provide the first definite observational data of antiproton flux, based on eight mass-identified clear antiproton events, and are consistent with the upper limits set by the PBAR [28] (observed no antiprotons) and the LEAP [30] (observed one antiproton candidate) experiments.

These results are consistent with the predicted fluxes of secondary antiprotons produced in the propagation of cosmic rays, showing no excess at the low energies. This might provide a restriction on the models of productions of primary antiprotons such as the evaporation of the primordial black holes or the annihilation of the neutralino dark matters.

Primordial Black Holes (PBHs)

The antiproton spectrum from the evaporation of primordial black holes rises at low energies below 1GeV. Hence the measured flux of low energy antiprotons would place an upper limit on the average evapolation rate of primordial black holes. The 90% C.L. upper limit of a poisson process with two signals and 0.47 expected backgrounds is 4.9, yielding a flux of $1.6 \times 10^{-2} m^{-2} sr^{-1} sec^{-1} GeV-1$. Adding 1.28σ of systematic error to this, we obtained the 90% C.L. upper limit of the antiproton flux in the energy range 175–350GeV: $1.7 \times 10^{-2} m^{-2} sr^{-1} sec^{-1} GeV-1$. According to the calculation of Maki *et al.*[15], this result places an upper limit on the present average evapolation rate of PBHs within a few kpc away from the Solar system;

$$R < 1.3 \times 10^{-2} pc^{-3} yr^{-1} \tag{6.1}$$

which is eight orders of magnitudes stringent than (i) the upper limit from the observations of the rate of 50-TeV γ-ray bursts ($R < 8.5 \times 10^{5} pc^{-3} yr^{-1}$) [61], (ii) the practical sensitivity for 100-MeV γ-ray bursts ($R \sim 10^{5} pc^{-3} yr^{-1}$) [62], and improved the upper limit based only on the BESS-93 data [31]. The limit placed by the observed spectrum of the diffuse γ-ray background does not restrict the local density of PBHs, and will be discussed as a constraint to their average density in the universe, since the diffuse γ-ray background would contain contributions from all evaporating PBHs within the horizon.

Following the way of Maki *et al.*[15], the limit (6.1) is converted to an upper limit on the ratio of the density of presently evapolating PBHs to that of halo dark matter;

$$\varepsilon_* \equiv \frac{M_*^2}{\rho_h}\frac{dn}{dM_i}(M_i = M_*) < 2.2 \times 10^{-8} ,$$

where M_i is the initial mass of PBHs, M_* that of a PBH just expiring today, n the number density of PBHs in the vicinity of the Solar system, and ρ_h the density of halo dark matter near the Solar system. According to the scenario that PBHs were formed from density inhomogeneities in the early universe, this provides an upper limit on the amplitude of initial density fluctuations of the universe [63] on a very small scale $M_* \simeq 5.3 \times 10^{14}$g;

$$\beta(M_*) \simeq 1 \times 10^{-18}\varepsilon_*\left(\frac{\Omega_h}{0.1}\right) \tag{6.2}$$

$$< 2.2 \times 10^{-26}\left(\frac{\Omega_h}{0.1}\right) , \tag{6.3}$$

where $\beta(M_*)$ is the fraction of the mass of the universe going into PBHs of the mass M_*, and in the equation(eq:PBHbeta) a flat Friedmann universe was assumed. One can obtain the density of PBHs, assuming a scale-invariance in the density fluctuations;

$$\Omega_{PBH} \simeq 2.0 \times 10^{-1}\varepsilon_*\left(\frac{\Omega_h}{0.1}\right)$$
$$< 4.4 \times 10^{-9} \quad \text{for} \quad \Omega_h = 0.1 ,$$

where Ω_{PBH} is the density of PBHs in units of the critical density. This limit is comparable to that placed by the diffuse γ-ray background ($\Omega_{PBH} \lesssim 10^{-8}$), for which a uniform distribution of PBHs throughout the universe is assumed [64].

Supersymmetric Dark Matter

Jungman and Kamionkowski [17] recently discussed the new gluonic contribution to the annihilation processes, in which a simple B-ino dark matter may produce a significant cosmic ray antiproton signal, as shown in Figures 5.19 and 5.20, in the case that the annihilation proceeds mainly to the two-gluon final state. It is not possible to confirm nor to reject positively the predicted spectrum of antiproton flux produced by annihilations of 30-GeV B-ino dark matters by our results.

The BESS experiment proved that the antiprotons with energies below 500MeV can be detected with a instrument with as large geometrical acceptance as the BESS instrument. A longer duration of flight would provide a flux measurement with a smaller statistical errors. In addition, it is also important to measure the flux at higher energies where the larger number of antiprotons would provide a better statistics than in the measurements ever performed. We performed another

experiment with a higher resolution of the TOF system in 1995, the data of which is under analysis, and the antiproton identificaton would be possible up to 1GeV or more. In addition, new devices for particle identification will be installed in the next flight under planning, extending the energy range of antiproton measurement up to a few tens of GeV, providing a *continuous* measurement of the flux over a wide energy range about 0.2 to 10GeV with a high precision. A long duration flight of up to 15 days is also being planned, which will provide an order of magnitude higher statistics of antiproton flux than in the present data, and would offer a confirmation whether there is a structure in the low energy antiproton flux or not.

Chapter 7

Conclusions

The BESS experiment detected eight antiprotons with the lowest energies ever observed. Which was the first observation of mass-resolved cosmic-ray antiprotons and provides the first finite value of cosmic antiproton flux at the low energies. The large tracking volume with the strong magnetic field provided a clear rejection of possible background due to interactions in the instrument. Two antiprotons in the energy range 175 to 350 MeV, four in 350 to 500 MeV and two in 500 to 600MeV (all in the energies at the top of the atmosphere) provided the antiproton flux after the corrections for the possible contaminations from antiprotons produced in the atomosphere and for the instrumental and selectional efficiencies:

$$F_{\bar{p}} = \begin{cases} (5.1\ ^{+8.9}_{-3.7}\ ^{+2.9}_{-2.4}) \times 10^{-3} & (175 \text{ to } 350 MeV) \\ (9.2\ ^{+9.7}_{-5.6}\ ^{+4.8}_{-3.6}) \times 10^{-3} & (350 \text{ to } 500 MeV) \\ (1.0\ ^{+2.0}_{-0.8}\ ^{+0.5}_{-0.4}) \times 10^{-2} & (500 \text{ to } 600 MeV) \end{cases}$$

where the error values are the statistical and the systematic errors respectively. The ratio of antiproton flux to proton flux was also derived as:

$$\bar{p}/p = \begin{cases} (3.6\ ^{+6.2}_{-2.6}\ ^{+2.0}_{-1.7}) \times 10^{-6} & (175 \text{ to } 350 MeV) \\ (7.0\ ^{+7.3}_{-4.3}\ ^{+3.6}_{-2.7}) \times 10^{-6} & (350 \text{ to } 500 MeV) \\ (1.0\ ^{+1.9}_{-0.7}\ ^{+0.5}_{-0.4}) \times 10^{-5} & (500 \text{ to } 600 MeV) \end{cases}$$

These results are consistent with the previous reports on the upper limit to the $\bar{p}/p$ ratio of the PBAR[28] and the LEAP[30] experiments, and provide the most strict conditions in $\bar{p}/p$ ratio ratio in these energy range.

The results are also consistent with the predictions of antiproton flux based on the antiproton production by the collisions of cosmic rays with interstellar media. Several novel mechanisms that can produce low-energy $\bar{p}$'s were also discussed. The

density of primordial black holes (PBHs) evapolating right in the present epoc is limited as:

$$R < 1.3 \times 10^{-2} pc^{-3} yr^{-1} \quad (90\% \text{ C.L.})$$

and this leads to an upper limit on the density parameter of PBHs:

$$\Omega_{PBH} < 4.2 \times 10^{-9} \quad for \quad \Omega_h = 0.1$$

where Ω is the density in units of the critical density of the universe, Ω_{PBH} for the density of PBHs and Ω_h for the density of the halo dark matter.

The model of supersymmetrical dark matter is not possible to be limited nor confirmed from our results.

The BESS-93 and BESS-94 experiments proved that a large volume detector with many tracking points is powerful to observe a very small portion of cosmic rays, identifying various backgrounds reliably, as well as gathering a large number of events. The current result of BESS experiments showed that the antiproton flux will be measured with a certain precision at energies below 300MeV when a experiment with a several times longer duration is performed. At the same time, a more precise measurement above 500MeV is also important to clarify the processes to produce cosmic antiprotons, thus, it is also desired to make a new observation of antiprotons at higher energy ranges with large volume detectors that have the capability to identify particles over the energy range of interest.

Acknowledgments

I wish to extend my sincere gratitude to Professor S. Orito, who has been leading the BESS experiment, for his guidance throughout my research. I also wish to gratefully acknowledge A. Yamamoto who has managed the experiment. The analysis were done owing a lot to Prof. S. Orito and K. Yoshimura. I would like to thank them for their suggestions and helpful discussions at the various stages of the analysis.

I would like to thank all the BESS colleagues for their effort to make a success of the experiment, especially M. Nozaki, M. Imori and T. Yoshida for their overall contributions; K. Anraku, T. Saeki, H. Matsunaga, M. Motoki, N. Takimi, H. Matsumoto, T. Sanuki, and M. Otoba for their excellent works on the experiment. D. Righter is also thanked for his professional technical support. I wish to acknowledge the contributions to the analysis from K. Anraku, T. Saeki, H. Matsunaga, M. Motoki, T. Sanuki and Y. Nishihara. I am also indebted to Y. Makida, K. Tanaka, M. Kimura, and the other staffs who have worked on the superconducting magnet; to J. Suzuki, Y. Higashi, Y. Ajima, S. Koizumi, and all the other KEK staffs who contributed to the construction of the BESS instruments; and to K. Shimamura, T. Haga, T. Tsunoda, and all the other people who was once involved in the experiment. It is a pleasure to express my appreciation to J. Ormes, R. Streightmatter, J. Mitcell, N. Yajima, T. Yamagami, R. Golden, and B. Kimbell who were the collaborators of the experiment.

I greatly appreciate helpful comments received from Prof. J. Nishimura, discussions with T. Mitsui and K. Maki about the theoretical predictions. I also wish to thank A. Moiseev and S. Stochaj for useful discussions, and E. S. Seo who provided me the data of IMP-8. I also wish to acknowledge that the figures on the neutron monitor data were retrieved from Space Physics Data System of University of Chicago, supported by National Science Foundation Grant ATM-9420790.

At last, but not least, I am grateful to Dr. V. Jones and all other people at NASA who supported BESS, and to the balloon campaign team from the National Scientific Balloon Facility for their professional and excellent work in carrying out the BESS flights. Strong support of National Laboratory for High Energy Physics (KEK) under the leadership of Prof. H. Sugawara and Prof. S. Iwata is greatly acknowledged. Sincere thanks are given to International Center for Elementary Particle Physics (ICEPP) of University of Tokyo for kindly allowing me to use their workstations. The BESS experiment has been supported by Monbusho International Scientific Research Grant and Scientific Research Grant, Kurata Research Grant, and Sumitomo Research Grant.

References

[1] Gaisser, T. K., and Maurer, R. H., Phys. Rev. Lett. **30**, 1264 (1973).

[2] Gaisser, T. K., and Mauger, B. G., Ap. J. **252**, L57 (1982).

[3] Simon, M. and Heinbach, U., in *"Cosmic Rays, Supernovae and the Interstellar Medium"*, edited by Shapiro, M. M., *et al.*, p.137. (Kluwer Academic Publishers, Dordrecht/Boston/London, 1991)

[4] Gaisser, T. K., and Schaefer, R. K., Ap. J. **394**, 174 (1992).

[5] Heinbach, U. and Simon, M., Ap. J. **441**, 209 (1995)

[6] Mitsui, T., Doctoral thesis, Univ. of Tokyo, in preparation.

[7] Hawking, S., Mon. Not. R. astr. Soc. **152**, 75 (1971).

[8] Carr, B. J., Hawking, S. W., Mon. Not. R. astr. Soc. **168**, 399 (1974).

[9] Carr, B. J., in *"Observational and Theoretical Aspects of Relativistic Astrophysics and Cosmology"*, edited by Sanz, J. L. and Goicoechea, L. J., p.1. (World Scientific Publishing Co. Pte. Ltd., Singapore, 1985)

[10] Hawking, S. W., Nature **248**, 30 (1974).

[11] Hawking, S. W., Commun. math. Phys. **43**, 199 (1975).

[12] Kiraly, P., Wdowczyk, J., and Wolfendale, A. W., Nature **293**, 120 (1981).

[13] Turner, M.S., Nature **297**, 379 (1982).

[14] MacGibbon, J. H. and Carr, B. J. Ap. J. **371**, 447 (1991).

[15] Maki, K., Mitsui, T., and Orito, S., preprint ICEPP-9403, 1994

[16] Silk, J., and Srednicki, M., Phys. Rev. Lett. **53**, 624 (1984).

[17] Jungman, G., Kamionkowski, M., Phys. Rev. D **D49**, 2316 (1994).

[18] Aizu, H., *et al.*, Phys. Rev. **121**, 1206 (1961).

[19] Apparao, M. V. K., Nature **215**, 727 (1967).

[20] Apparao, K. M. V., *et al.*, Proc. 19th Intl. Cosmic Ray Conf. (La Jolla), **2**, 326 (1985).

[21] Bogomolov, E. A., *et al.*, Proc. 16th Intl. Cosmic Ray Conf. (Kyoto), **1**, 330 (1979).

[22] Golden, R. L., *et al.*, Phys. Rev. Lett. **43**, 1196 (1979).

[23] Golden, R. L., *et al.*, Astrophysical Letters, **24**, 75 (1984).
Stephens, S. A. and Golden, R. L. Space Sci. Rev. **46**, 31 (1987).

[24] Stephens, S. A. and Golden, R. L. Astron. Astrophys. **202**, 1 (1988).

[25] Buffington, A., Schindler, S. M., and Pennypacker, C. R., Ap. J.**248**, (1981) 1179.

[26] Bogomolov, E. A., *et al.*, Proc. 20th Intl. Cosmic Ray Conf. (Moscow), **2**, 72 (1987).

[27] Bogomolov, E. A., *et al.*, Proc. 21th Intl. Cosmic Ray Conf. (Adelaide), **3**, 288 (1990).

[28] Ahlen, S. P., *et al.*, Phys. Rev. Lett. **61**, 145 (1988).
Barwick, S. W., *et al.*, Proc. 21st Intl. Cosmic Ray Conf. (Adelaide), **3**, 273 (1990).
Salamon, M. H., *et al.*, Ap. J. **349**, 78 (1990).

[29] Moats, A., *et al.*, Proc. 21st Intl. Cosmic Ray Conf. (Adelaide), **3**, 284 (1990).

[30] Streitmatter, S. J., *et al.*, Proc. 21st Intl. Cosmic Ray Conf. (Adelaide), **3**, 277 (1990).
Stochaj, S. J., Ph.D. thesis, Univ. of Maryland, (1990).

[31] Yoshimura, K., *et al.*, Phys. Rev. Lett. **75**, 3792 (1995).
Also, Yoshimura, K., Doctoral thesis, Univ. of Tokyo (1995).
Orito, S., Nucl. Phys. B (Proc. Suppl.) **43**, 237 (1995).

[32] Orito, S., Proc. of ASTROMAG Workshop, KEK Report 87-19, 111 (1987).

[33] Yoshida, T., *et al.*, Proc. of the Second Workshop on Elementary-Particle Picture of the Universe, KEK, 142 (1988).

[34] Yamamoto, A., editor, Proc. of the 3rd BESS Workshop, KEK Proceedings 92-2 (1992).

[35] Yamamoto, A., *et al.*, Adv. Space Res. **14**, 75 (1994).

[36] Nozaki, M., *et al.*, Proc. 24th Intl. Cosmic Ray Conf. (Rome), **3**, 579 (1995).

[37] Yoshida, T., *et al.*, in preparation.

[38] Yamamoto, A., *et al.*, IEEE Trans. on Magnetics **24**, 1421 (1988).

[39] Makida, Y., *et al.*, Adv. in Cryogenic Engineering, **37**, 401 (1992).

[40] Drumm, H., *et al.*, Nucl. Instr. and Meth., **176**, 333 (1980).

[41] Allison, J., *et al.*, Nucl. Instr. and Meth., **A236**, 284 (1985).

[42] Anraku, K., *et al.*, IEEE Trans. on Nuclear Science NS-**40**, 717 (1993).

[43] Anraku, K., *et al.*, IEEE Trans. on Nuclear Science NS-**39**, 987 (1992).

[44] Imori, M., *et al.*, IEEE Trans. on Nuclear Science NS-**39**, 1389 (1992).

[45] Saeki, T., *et al.*, Nucl. Instr. and Meth., A **355**, 506 (1995).

[46] Imori, M., *et al.*, IEEE Trans. on Nuclear Science NS-**40**, 913 (1993).

[47] Yoshida, T., Proc. of the 5th BESS Workshop, KEK Proceedings 94-11, 31 (1994).

[48] Goossens, M., *ZEBRA – Overview of the ZEBRA system*, CERN Program Library Q100/Q101. CERN, 1993

[49] Application Software Group, *HEPDB – Database Management Package*, CERN Program Library Q180. CERN, 1993

[50] Bruyant, F., *et al.*, *GEANT – Detector Description and Simulation Tool*, CERN Program Library W5013. CERN, 1993

[51] Karimäki, V., Report of University of Helsinki, HU-SEFT-1991-10.

[52] Papini, P., Grimani, C., and Stephens, S. A., Proc. 22nd Intl. Cosmic Ray Conf. (Calgary) **3**, 761 (1993).

[53] Stephens, S. A., Proc. 22nd Intl. Cosmic Ray Conf. (Calgary) **2**, 144 (1993).

[54] Pfeifer, Ch., Heinbach, U. and Simon, M., Proc. 22nd Intl. Cosmic Ray Conf. (Calgary) **2**, 148 (1993).

[55] Inoue, A. *et al.*, The bulletin of the Institute for Space and Astronautical Science, the special issue on the scientific ballooning pp.79 (1981).

[56] Webber, W. R., Astron. Astrophys. **179**, 277 (1987).

[57] Seo, E. S., *et al.*, Ap. J. **378**, 763 (1991).

[58] Glesonn, L. J., and Axford, W. I., Ap. J. **154**, 1011 (1968).

[59] McGuire, R. E., *et al.*, Ap. J. **301**, 938 (1986).

[60] Particle Data Group, Phys. Rev. D**50**, 1281 (1994).

[61] Alexandreas, D. E., *et al.*, Phys. Rev. Lett. **71**, 2524 (1993).

[62] Semikov, D. V., Ap. J. **436**, 254 (1994).

[63] Carr, B. J. and Lidsey, J. E., Phys. Rev. D**48**, 543 (1993).

[64] Page, D. N. and Hawking, S. W., Ap. J. **206**, 1 (1976).

[65] Mitchell, J. W., *et al.*, submitted to Phys. Rev. Lett. Also, Proc. 24th Intl. Cosmic Ray Conf. (Rome), **3**, 72 (1995).